POLITECNICO DI TORINO

SCUOLA DI DOTTORATO
Dottorato in Ingegneria Elettronica e delle Comunicazioni
XXVII Ciclo

Tesi di Dottorato

Microring-Resonator-Based Switch Architectures for Optical Networks

Jinan Xia

Tutore
Prof. Andrea Bianco

Coordinatore del corso di dottorato
Prof. Ivo Montrosset

December 2014

Abstract

Flexible optical networking has emerged as a way to offer efficient use of available optical spectral resources as introduced in the ITU-G.694.1. In the flexible optical networking, the network dynamically adjusts its resources including the optical bandwidths and the modulation formats according to the requirement of each connection. For the flexible networks, critical components are flexible optical switches which have variable bandwidth characteristics at a fine granularity. The key to provide such variable bandwidth characteristics lies in wavelength selective switches (WSSs).

Integrated silicon photonics provides a promising platform for chip-based, high-speed optical signal processing due to its compatibility with complementary metal-oxide semiconductor (CMOS) fabrication processes. They are attracting significant research and development interest globally and making a huge impact on green information and communication technologies, and high-performance computing systems.

Microring resonators (MRRs) show the versatility to implement a variety of network functions, compact footprint, and complementary metal-oxide semiconductor compatibility, and demonstrate the viability applied in photonic integrated technologies for both chip level and board-to-board interconnects. Furthermore, MRRs have excellent wavelength selection properties and can be used to design tunable filters, modulators, wavelength converters, and switches that are critical components for optical interconnects.

The research work of this dissertation is focused on investigating how to develop MRR-based switches and switch architectures for possible applications not only in optical interconnection networks but also in flexible-grid on-chip networks for optical communication systems. The basic properties and performances of the MRR switches and the MRR switch architectures related to their applications in the networks are examined. In particular, how to design and how to configure high performance, bandwidth variable, low insertion loss, and weak crosstalk MRR-based switches and switch architectures are investigated for applications in optical interconnection networks and in flexible-grid on-chip networks for optical communication systems.

This dissertation first investigates the physical characteristics of the switching

devices consisting of single MRRs and multiple cascaded MRRs. The spectral pass-band shapes and widths as well as the propagation losses of single MRR and cascaded MRR switch devices are discussed. The physical behaviours of the MRRs are determined by their physical and geometrical parameters, including the MRR diameters, the number of cascaded MRRs, the refractive indices of the waveguides of the MRRs, the dispersions of the refractive indices, the light coupling coefficients between the MRRs, and the propagation losses in the MRRs. These parameters have different influences on the physical behaviours of the MRR switch devices. Some of them strongly affect the spectral properties, some of them have weak influences. How the parameters affect the performances of the MRR switch devices is studied for MRR-based device design.

Results show that main factors affecting the passband widths of MRR switch devices are the diameters of the MRRs, the light coupling coefficients between the MRRs, the light coupling coefficients between the MRRs and the bus waveguides of the MRR devices, and the ring numbers. The bandwidths increase with the increase in the coupling coefficients between the bus waveguides and the MRRs and between the MRRs. Using smaller MRRs can achieve larger passband widths in the switches. Cascading multiple MRRs can achieve flat-top passbands in the switches by optimal design. The flat-top passbands of the switch devices can improve the uniformity of the output power distribution of the switches and reduce inter-channel interferences in optical networks. The results show that it is possible to achieve flat-top passband widths ranging from 6.25 GHz to 3 THz by cascading three microring resonators, while having their insertion losses compatible with the use in flexible-grid optical communication networks.

Main factors affecting the insertion losses of MRR switch devices are the light coupling coefficients between the bus waveguides of the MRR switches and the MRRs, and the light coupling coefficients between the MRRs, and the propagation losses in the MRRs and the bus waveguides. When the light coupling coefficients between the bus waveguides and the MRRs and between the MRRs increase, the insertion losses of the MRR switches decrease. There are optimal diameters to achieve satisfactory insertion losses for the MRR switches. At the optimal diameters, the insertion losses of the switches become the minimal.

Filters, switches, and other photonic devices are required to have flat-top spectral passbands with steep edges in order to achieve uniform intensity distribution and to reduce inter-channel interference in optical communication networks and on-chip interconnects. Although flat-top passbands with steep edges are achieved in MRR devices by accurately controlling the ring diameters, coupling coefficients between rings and waveguides, as well as the number of microrings, flexible grid networks have more rigorous requirements on the passband widths. For flexible grids, the minimal frequency slot width is 12.5 GHz, and the minimal frequency spacing is 6.25 GHz. To support the channel slot widths of 12.5, 25, and 50 GHz in flexible grids,

ultra-narrow passband filters/switches are needed. It is challenging to achieve such a narrow passband width of 12.5 GHz using ordinary photonic devices. But narrow passbands of the devices lead to more serious signal crosstalks between adjacent channels. One of the dissertation works is focused on sharpening the passbands of the MRR switches. To do so, cascaded MRR architectures are configured to achieve the narrow passband with low crosstalk. However, it is obvious to induce higher light power loss. In this case, optimal architecture design is performed so that satisfactory crosstalk, loss, flat-top passband shape are achieved.

The spectral shapes of the passbands of the cascaded MRR switches and the multi-stage cascaded MRR switches are investigated in detail. The results show that steep-edge flat-top spectral responses at the drop ports of the multistage MRR-based switches are achieved. Increasing stage number can obtain steeper-edge response spectra of the multistage MRR-based switches, however it also increases the transmission losses of the switches. The simulation shows that the multistage cascaded MRR-based switches provide better passband properties than the MRR-based switches without stages. Clear, regular, smooth, steep roll-off edge flat-top passpands are achieved in the multistage cascaded MRR-based switches. Irregular and fluctuating passpands are shown in the high-order MRR-based switches without stages. In order to achieve steep-edge flat-top passpands of MRR switches or filters, it is better to use the multistage cascaded MRR structures with optimal design instead of the simple cascaded MRR structures without stages. But there is a trade-off between the insertion loss and the passband width to achieve an optimal performance in a switch design.

WSSs are critical enabling devices of flexible grid networks and the research work focuses on building WSS optical switch architectures for the networks based on MRR wavelength selective switches. Different spectral passband widths can be obtained by properly designing optimal MRR architectures. The feasibility of the architectures to be applied in the network is discussed by estimating their insertion losses and crosstalks, in particular, by estimating their insertion losses and crosstalks in the worst cases. The work aims to achieve feasible and optimal architectures that can be applied in optical networks not only as stand-alone devices but also as components for on-chip networks. Two types of MRR-based switch architectures are designed by using 320, 160, and 80 third-order MRR switches with -3 dB passband widths of 12.5, 25, and 50 GHz, respectively, and by using $4 \times 80 \times 12.5$ GHz, $4 \times 40 \times 25$ GHz, and $4 \times 20 \times 50$ GHz two-stage MRR switches. Both architectures are able to achieve variable output bandwidths varying from 0 to 4 THz. Results show that the former is superior to the latter based on the comparison of the maximal insertion losses and the crosstalks in the worst cases. Nevertheless, suitable selection of optical spectra can avoid high insertion losses and serious crosstalks between the adjacent channels in the latter architecture.

Bandwidth-variable microring-resonator-based wavelength selective switches with

multiple input and multiple output ports are proposed. A detailed analysis is presented on the switches consisting of the third-order microring resonators. As a proof of concept, the structural design of a four output port switch is investigated in detail. The results show acceptable insertion losses and signal crosstalk suppression ratios for the application in on-chip optical networks and optical communication networks. Deep research works show that the MRR-based WSSs are superior to WSSs based on the liquid-crystal-on-silicon spatial light modulators (LCoS-SLMs) since MRR-WSSs have low power consumption, and they need relatively simple device fabrication technology. In particular, the proposed MRR-based architectures are superior to the WSSs based on cyclic array waveguide gratings in structural design versatility, light switching control agility, and passband width adjustment, implying that the proposed bandwidth-variable microring-resonator-based wavelength selective switches have the potential to in part or completely replace the LCoS-SLMs and arrayed waveguide grating (AWG) switches for the application in the optical networks, in particular, for high performance computing systems and data center networks.

Scalable, low latency, and high-throughput interconnection is essential for future high performance interconnect networks. Interconnect networks based on electronic multistage topologies have large latencies, due to the multi-hop nature of these networks and high power consumption in the buffers and the switch fabrics. It is increasingly difficult to meet large bandwidth and low latency communications using conventional electrical switches. A chip-scale optical switch architecture is proposed for scalable interconnect network, and the performance of the switch architecture is studied by simulating the end-to-end latency and transmission packet loss rate under high traffic loads. The work aims to demonstrate if it is feasible to use MRRs to build WSSs for flexible grid on-chip networks and optical interconnects and optical networks. By using OMNet++ software, the simulated results show very low latencies and low packet losses at large throughputs.

In summary, the research of the dissertation contributes to develop high performance, variable bandwidth, low insertion loss, and low crosstalk MRR-based optical switches and switch architectures to adapt to dynamic source allocation of flexible-grid optical networks.

Acknowledgements

Contents

VIII

List of Figures

x

List of Tables

List of Abbreviations

AOWC	All-optical wavelength converter
AWG	Arrayed waveguide grating
CAWG	Cyclic arrayed waveguide grating
CMOS	Complementary metal-oxide semiconductor
DWDM	Dense wavelength division multiplexing
DPSK	Differential phase-shift keying
FSR	Free spectral range
MRR	Microring resonator
ITU	International Telecommunication Union
LCoS-SLM	Liquid-crystal-on-silicon spatial light modulator
MEMS	Microelectromechanical system
MIMO	Multiple input and multiple output
MZI	Mach-Zehnder interferometer
OFDM	Orthogonal frequency division multiplexing
ROADM	Reconfigurable optical add/drop multiplexer
SEM	Scanning electron microscope
SOI	Silicon on insulator
SOA	Semiconductor optical amplifiers
TE	Transverse electric
TM	Transverse magnetic
WSS	Wavelength selective switch

Chapter 1

Introduction

1.1 Background

1.1.1 Flexible-Grid Optical Network

Continuous increase of traffic has urged effective use of available spectral resources in optical networks. Rigid fixed-grid wavelength division multiplexing optical networks can no longer keep up with the emerging bandwidth-hungry and highly dynamic services in an efficient manner. As the available spectrum becomes occupied, the research community has focused on seeking more advanced optical transmission and networking solutions that utilize the available bandwidth more effectively. To this end, the flexible/elastic optical networking paradigm has emerged as a way to offer efficient use of the limited optical resources [1] as introduced in the ITU-G.694.1 [2]. In the flexible/elastic optical networking, flexible frequency grids are recommended to be used.

The flexible grids for dense wavelength division multiplexing (DWDM) optical networks are different from the fixed frequency grids in defining nominal central frequencies, channel spacings, and the concept of frequency slot. The main difference is that the basic unit of switching is identified, which is the frequency slot in flexible grid case now instead of a wavelength in fixed grid case. A frequency slot is defined by its nominal central frequency in the whole spectrum range and its slot width. In flexible grid case, the set of nominal central frequencies can be built using the following expression $f = 193.1 + n \times 0.00625$ THz, where 193.1 THz is ITU-T "anchor frequency" for transmission over the C-band, and n is a positive or negative integer including 0. The central frequency can be moved in the C-band at 6.25-GHz step. The slot width determines the "amount" of optical spectrum regardless of its actual position in the spectrum. A slot width is constrained to be $m \times 12.5$ GHz, where m is an integer greater than or equal to 1. In the fixed-grid case, each connection is allowed to occupy only one spectrum slot, whereas multiple spectrum slots can be

allocated to one connection in the flexible-grid case. Figure 1.1 shows the examples of optical channel assignments under fixed and flexible grids. In the fixed grid as shown in Fig. 1.1(a), there are three channels at the central frequencies with the channel spacings of 50 GHz. In the flexible grid as shown in Fig. 1.1(b), the channel spacings are 6.25 GHz. There are two slots with the slot widths of 25 or 37.5 GHz.
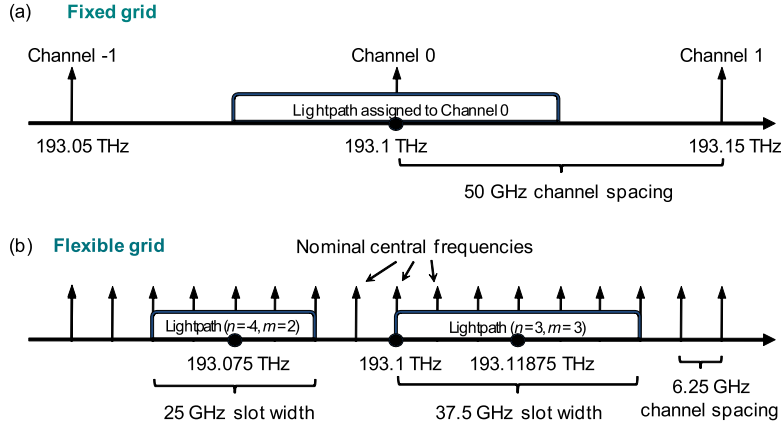
Figure 1.1. Optical channel assignment in optical networks under (a) fixed and (b) flexible grid.

Using flexible frequency grids in the optical networks can save a lot of spectra, resulting in significant increase in spectral efficiency. Figure 1.2 shows the comparison of occupied spectra for three channels when the network uses fixed grids and flexible grids. As can be seen, the three channels occupy three spectrum units (Assuming a unit of 50 GHz, total spectrum width is 150 GHz.) in fixed grids as shown in Fig. 1.2(a). In flexible grids, the three channels occupy only one and half spectrum units (75 GHz) or less (37.5 GHz), resulting in the saved spectral width of 75 or 112.5 GHz that can be used by other channels.

In the flexible grid optical networking, the network dynamically adjusts its resource of the optical bandwidths according to the requirement of each connection. For the flexible networking, the critical enabling components are flexible optical switches. Flexible optical switches should have variable bandwidth characteristics (i.e., tunable optical bandwidths and center frequencies of channels) at a fine granularity. The key to provide such variable bandwidth characteristics lies in wavelength selective switches (WSSs), which sit at the heart of the optical switch [3]. The first proposal for a variable passband/flexigrid WSS was reported in [4]. It is possible to construct advanced WSSs using liquid crystal-on-silicon spatial light modulators (LCoS-SLMs) [5] or microelectromechanical system (MEMS) devices [6]. However,
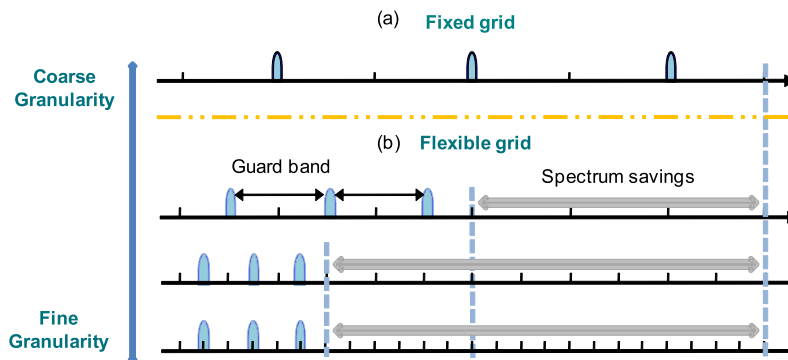
Figure 1.2. Comparison of occupied spectra in optical networks under (a) fixed and (b) flexible grid.

they need large space to realize wavelength selection function and they can not be used in chip-level optical networks and optical interconnections. Arrayed-waveguide-grating-based WSSs [7] are available in the market, but their fabrication is relatively complicated compared with the fabrication of MRRs reported.

1.1.2 On-Chip Optical Networks

Recent progress in silicon compatible photonics, in particular, the success in hybrid silicon laser sources [8], is driving high density integration of photonic and electronic components manufactured by complementary metal-oxide semiconductor(CMOS)-based technology on the same platform. Integrated silicon photonics provide a promising platform for chip-based, high-speed optical signal processing due to its compatibility with CMOS fabrication processes. Photonic integrated technologies are attracting significant research and development interest globally and making an huge impact on green information and communication technologies and high-performance computing systems since they offer high-bandwidth, low latency, and high power efficiency transmission in photonic-integrated circuits.

Microring resonators (MRRs) have been experimentally demonstrated as modulators [9, 10], filters, switches, multiplexers, demultiplexer, routers, wavelength converters, and lasers [11–15]. All of the components are the basic components of optical communication networks and optical interconnections. Due to small and compact structures of MRRs, these devices are able to be integrated on a chip to configure optical interconnections and optical networks.

Recent experimental works have demonstrated the viability of photonic integrated technologies for both chip level and board-to-board interconnects. Microring

resonators show the versatility to implement a variety of network functions, compact footprint, and complementary metal-oxide semiconductor compatibility. Microring resonators have potential to become key components for low-cost photonic integration.

Chip-level photonic interconnects [13, 16, 17], are today based on single wavelength mode operation, but can be extended to the WDM domain to support a comb of wavelengths. More precisely, when the comb of wavelengths matches the periodical transfer function of the MRR it is possible to switch a large number ($\sim$40) of channels simultaneously [18], providing high bit rates.

Based on the potential capabilities of MRRs for chip-level applications, recent proposals have extended their usage in board-to-board optical interconnects [19–21]. These architectures are composed of tunable transmitters that transfer data packets towards waveband burst-mode receivers through a switching fabric. These wavelength agile architectures offer promising capabilities that can be exploited in future optical networks. However, control issues and the difficulty of the filters providing variable bandwidths in the architectures may limit MRR role in switching fabrics if the flexible grid paradigm is applied. The main research challenge is to demonstrate if MRRs can offer reliable and cost-effective architectures.

MRRs show the advantages in several aspects. They are very small and compact. They can be used to build various architectures with different functions. Thus they are suitable for integration. If the MRRs are controlled by carrier injection for optical switching, high switching speed can be achieved. Moreover, their power consumptions are very low. In addition, ultra-narrow passband like 12.5 GHz in frequency (approximate 0.1 nm in wavelength) can be achievable in MRR switches to support flexible grids, while it is hard to achieve ultra-narrow passband with ordinary photonic devices.

However, there are challenging issues in MRR-based devices. The insertion loss of a MRR switch device is high, compared with an ordinal large volume optical switch in optical networks. The resonant wavelength of a MRR switch is sensitive to its fabrication errors in diameters or perimeters. The rough surface of the waveguide of a MRR leads to retro-reflection, resulting in signal interference and power loss. The refractive indices of MRR waveguides and the coupling coefficients between MRRs change with the frequencies or wavelengths of light propagating in the microring resonators. The light propagation behaviours in the microring resonators are sensitive to the light polarization.

1.2 Motivation and Objectives

Microring resonators have potential to be applied as many devices not only in off-chip optical communication networks and optical interconnections but also in on-chip

networks. However, there are a lot of challenging problems that are imperative to be solved. Our works are focused on designing MRR-based switches and switch architectures for possible applications in the flexible-grid networks, and on investigating how to solve scientific problems occurring in the switch device and architecture applications for flexible-grid networks.

We first investigate the physical characteristics of switching devices consisting of single MRRs and multiple cascaded MRRs. The spectral passband shapes and widths as well as the insertion losses of single MRR and cascade MRR switches are discussed. The physical behaviours of the MRRs are determined by their physical parameters and geometrical parameters, including the MRR diameters, the number of cascaded MRRs, the waveguide sizes, the refractive indices and dispersions of waveguides, the coupling coefficients between the MRRs, and the propagation losses in the MRRs. Since these parameters have different influences on the physical behaviours of the MRRs, we study how the parameters influence the performances of the MRRs so as to provide theoretical references and guides for MRR-based switch device design.

Second, the filters, switches, and other photonic devices are required to have flat-top spectral passbands with steep edges in order to achieve uniform intensity distributions into the devices in optical communication networks and on-chip interconnects and to reduce inter-channel interferences in the optical communication networks and on-chip interconnects. Although flat top passbands with steep edges are achieved in microring resonator (MRR) devices [22–25] by accurately controlling the ring diameters, coupling coefficients between rings and waveguides, as well as the number of microrings, flexible grid netwroks have more rigorous requirements on the bandwidths. For flexible grids, the minimal frequency slot width is 12.5 GHz, and the minimal frequency spacing is 6.25 GHz. To support the channel slots of 12.5, 25, and 50 GHz in flexible grids, corresponding to wavelength spacings of 0.1, 0.2 and 0.4 nm respectively in the wavelength spectrum around 1.55 μm, ultra-narrow passband filters/switches are needed. It is challenging to achieve such a narrow passband width of 12.5 GHz using ordinary photonic devices. Moreover, narrow passband usually leads to serious crosstalks in adjacent channels. The narrower the passband widths of the filters or switches are, the more serious crosstalks occurs in adjacent channels. How can we achieve the narrow pass bandwidths with acceptable insertion losses and low crosstalks between adjacent channels? We focus on sharpening the passbands of the MRR switches. To do so, we attempt to design cascaded MRR architectures to achieve the narrow passbands with low crosstalks. Furthermore, we attempt to design multi-stage cascaded MRR architectures to achieve flat-top steep-edge wide passbands for various applications in optical networks. However, it is obvious to induce higher light power losses when using multi-stage cascaded MRR architectures. In this case, we try to seek optimal architectures so that both passbands and losses can be satisfactory.

As introduced above, WSSs are critical enabling devices of flexible grid networks. We focus on building WSS optical switch architectures for optical networks and optical interconnections using MRRs. In fact, different spectral passband widths can be obtained by properly designing MRR switch architectures. After designing MRR switch architectures, we evaluate the feasibility of the architectures to be applied in the networks by estimating their insertion losses and crosstalks, in particular, estimating the insertion losses and crosstalks in the worst cases. Furthermore, we attempt to achieve feasible and optimal architectures that can be applied in optical networks not only as stand-alone devices but also as components for on-chip networks.

Scalable, low latency, and high-throughput interconnection is essential for future high performance interconnect networks. Interconnect networks based on electronic multistage topologies (e.g. Fat-Tree, CLOS, Torus, Flattened Butterfly [26, 27]) result in large latencies, due to the multi-hop nature of these networks and high power consumption in the buffers and the switch fabric. It is increasingly difficult to meet large bandwidth and low latency communications using conventional electrical switches. We discuss chip-scale optical switch architectures for scalable interconnect networks and conduct performance studies of the switch architectures by simulating the latencies and packet loss rates under high traffic loads, to demonstrate if it is feasible to build MRR WSSs for flexible grid on-chip networks and to develop advanced optical interconnect networks.

1.3 Outline

The dissertation is organized as follows. In Chapter 2, we review the literature on microring resonator tuning technologies. Basic MRR switch devices for switch architectures and optical interconnections about their structures, the operating principles, and their key parameters are introduced. We summarize the most relevant works in the literatures regarding tuning technologies for mircoring resonators: electro-optic, thermo-optic tuning technologies and the tuning technology based on nonlinear optics. Relevant microring-based devices are also reviewed. We analyze and discuss the differences in performance for the different tuning technologies. The switching speeds, tuning ranges, and application feasibilities of existing switching technologies are compared from the viewpoint of practical applications. We provide an overview of the state of the art of microring resonator switches in order to identify their suitability for current optical networking trends.

In Chapter 3, the physical characteristics of microring resonator switching devices are thoroughly analyzed using a model based on the field coupling matrix theory. The structures and the spectral response behaviors of the cascaded microring resonator devices are presented and illustrated. The spectral passband widths and

insertion losses of MRR-based switching devices as the functions of several physical characteristics of the MRRs, such as the coupling coefficients between the MRRs, the ring diameters, and the propagation losses in the MRRs are analyzed and discussed. Simple switch architectures based on MRRs are demonstrated as a possible application of the studied elements in flexible-grid networks. The architectures of simple MRR optical switches with limited functionalities are discussed, showing the potential use of MRRs for switching applications in flexible-grid optical networks. The spectral response and insertion loss properties of these switching elements are simulated using the developed model. Then we investigate the optimal design of high-order MRR-based switch devices.

Spectral shaping of the passbands of microring resonator switches is studied in Chapter 4. Multistage high-order microring resonator-based optical switch structures are proposed to achieve steep-edge flat-top spectral passband. Using the transfer matrix analysis model, the spectral response behaviors of the switch structures are simulated. The performances of the proposed multistage high-order microring resonator-based optical switch structures and the high-order microring resonator-based optical switch structures without stages are studied and compared. The studies attempt to show that multistage high-order microring resonator-based switches can achieve steep edge flat-top spectral passbands with rectangular shapes to meet the spectral passband requirements of flexible grid optical networks.

Two types of MRR-based switch architectures are proposed in Chapter 5 to realize variable output bandwidths varying from 0 to 4 THz. One consists of 320, 160, and 80 third-order MRR switches with -3 dB passband widths of 12.5, 25, and 50 GHz, respectively. Another one is two-stage switch structure. In the first stage there are 4 third-order MRR switches with the passband widths of 1 THz. In second stage, there are 80, 40, 20 third-order MRR switches with the passband widths of 12.5, 25, and 50 GHz, respectively. Their insertion losses and inter-channel crosstalks of the MRR-based switch architectures in the worst cases are numerically analysed and compared in order to show the feasibility for the architectures to be applied in flexible optical networks. In addition, the techniques and methods to reduce the crosstalk are studied and proposed.

MRR-based bandwidth-variable wavelength selective switch architectures with multiple input and output ports are proposed for flexible optical networks in Chapter 6. The light transmission behaviors of a $1 \times N$ MRR-based WSS are analyzed in detail based on numerical simulation using transfer matrix theory. Two types of $N \times N$ MRR-based WSS architectures consisting of MRR-based WSSs and MRR-based WSSs, and MRR-based WSSs and optical couplers are proposed. The performances of the proposed architectures are studied.

In Chapter 7, a simple but typical chip-scale scalable optical interconnections based on MRRs are proposed, which consist mainly of microring resonator devices:

microring lasers, microring switches, microring de-multiplexers, and integrated photodectors. Their throughput capacities, end-to-end time latencies, and transmission packet loss rates are evaluated using OMNet++. The study attempts to show that it is feasible to build on-chip optical networks and advanced optical interconnects for high performance computation and communication systems using MRR-based devices.

Finally, the conclusions and future works are presented.

Chapter 2

Microring-Resonator-Based Switches

Photonic integration technologies are attracting significant research and development interest globally and making an huge impact on green information and communication technologies and high-performance computing systems since they provide high-bandwidth, low latency, and high power efficiency transmission in photonic-integrated circuits. Integrated silicon photonics provides a promising platform for high density integration of photonic and electronic components manufactured by CMOS-based technology on the same platform. Microring resonators made of waveguides are extremely important components that can be integrated on a chip to perform switching operations directly in the optical domain. The waveguides can be made of different materials. We focus our MRR devices on silicon-based devices for their compatiblity with CMOS fabrication process and other reasons as introduced in Section 1.1.2.

The refractive index of a silicon waveguide can be tuned by thermo-optic effect or electro-optic effect. Thermo-optic effect is that when the silicon waveguide is heated, its refractive index is changed with the temperature inside the waveguide. Electro-optic effect is that the refractive index of a silicon waveguide is determined by its carrier concentration inside the waveguide. Changing the carrier concentration inside the waveguide by carrier injection can change the refractive index of the waveguide. Tuning the refractive index of a MRR waveguide can modulate the light signal output intensity of a MRR. It can also make light go through the MRR or stop light propagation through the MRR. It is a specially important for optical switching in MRR devices.

In this chapter, we review the literatures on resonant wavelength tuning technologies of microring resonators. We compare the switching speeds, tuning ranges, and application feasibilities of existing switching technologies from the viewpoint

of practical applications. We provide an overview of the state of the art of microring resonator switches in order to identify their suitability for current optical networking trends. The remainder of the chapter is organized as follows. In Section 2.1, we introduce basic MRR switch devices for switch architectures and optical interconnections about their structures, the operating principles, and their key parameters. In Section 2.2 we summarize the most relevant works in the literatures regarding tuning technologies for mircoring resonators: electro-optic, thermo-optic tuning technologies and the tuning technology based on nonlinear optics. Relevant microring-based devices are also reviewed. In Section 2.3, we analyze and discuss the differences in performance for the different tuning technologies. We draw the conclusions of this chapter in Section 2.4.

2.1 Basic Microring-Resonator-Based Switch Devices

In this section we introduce the structures of basic MRR-based switch devices, the principle of microring resonators, and the key parameters of microring resonators. A MRR-based device makes up of a microring resonator and two waveguides which can be perpendicular or parallel to each other as shown in Fig. 2.1. The microring resonator is made of a microring waveguide consisting of a core layer and cladding layers with different refractive indices. Figure 2.1(a) shows a schematic MRR switching structure making up of a single ring and two perpendicular waveguides while Figure 2.1(b) shows a schematic MRR switching structure making up of a single ring and two parallel waveguides. The MRR devices with two perpendicular waveguides are often used as basic building blocks for switches with a large number of ports [28–30], while the MRR devices with two parallel waveguides are often used to build the switches that contain cascaded rings [31].

In the two cases shown in Fig. 2.1, optical signals entering the *input* port can be either coupled into the MRR from the first waveguide, propagate in the MRR, then be coupled into the second waveguide from the MRR, and get out from the *drop* port, when their wavelengths meet the resonant condition of the MRR. If their wavelengths do not meet the resonant condition of the MRR, they will propagate in the first waveguide and get out directly from the *through* port. In brief, an optical signal at the wavelength λ_i is coupled to the microring and directed towards the drop port if the wavelength λ_i satisfies the resonant condition, while all other wavelengths are directed towards the through port. The resonance condition is defined by $2\pi R n_{eff} = m\lambda_i$, where n_{eff} is the effective index of refraction of the bending waveguide, R is the radius of the ring, and m is an integer indicating the order of resonance.

10

(a) MRR with perpendicular waveguides

(b) MRR with parallel waveguides
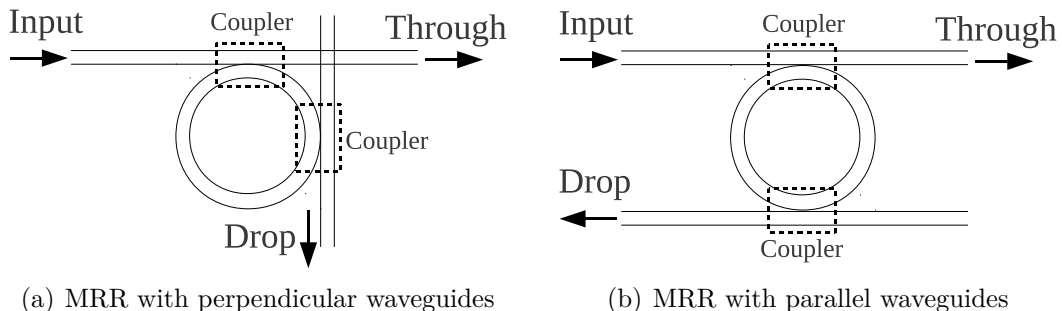
Figure 2.1. Two basic microring resonator switch structures

A key characteristic of microring resonators is that by changing the refractive index of the material in the ring waveguide, different wavelengths can be switched between the through port and the drop port. A change of the effective index Δn_{eff} causes a shift of the resonant wavelength $\Delta \lambda = \lambda_0 \cdot \Delta n_{eff}/n_{eff}$, where λ_0 is the initial resonant wavelength of the microring. Figure 2.2 shows an example of this behavior and the schematic spectrum at the drop port of the microring resonator. The light signals at three resonant wavelengths at the input port are initially (i.e. untuned state) deflected towards the drop port (λ_1, λ_3, and λ_5) while the light signals at the wavelengths of λ_2, λ_4, and λ_6) are directed towards the through port. When a change of the refractive index is applied by tuning the refractive index of microring waveguide (i.e. tuned state), the drop transfer function is right-shifted (see dashed line) so that all the light signals are directed towards the through port and thus switching the light signals at the wavelengths of λ_1, λ_3, and λ_5. Different tuning techniques and their state of the art are extensively explained in Section 2.2. Figure 2.2 also shows the free spectral range (FSR), defined as the spectrum distance between two resonant wavelengths. Derived from the resonant condition of a MRR, the free spectral range expression is $FSR \approx \lambda^2/(2\pi n_{eff}R)$. Other important design parameters are: the passband width (usually at -3 dB), the ON/OFF signal intensity ratio, and the insertion loss defined as the power loss when the light signal passing through the microring.

Another type of basic MRR switch structures is shown in Fig. 2.3. In the structures, two or more MRRs are cascaded to build a device together with two linear waveguides. The two linear waveguides are perpendicular or parallel to each other, arranged in the similar way to Fig. 2.1. In this case, the signals at the wavelengths within a band can be deflected toward the drop port. Figure 2.3(a) or Figure 2.3(b) represents two three-MRR-cascaded switches. Moreover, higher extinction ratios of drop signals or steeper flat-top wider passbands can be achieved in the cascaded MRR devices. In such case, each microring resonator of a device is named one order. The devices in Fig. 2.3 are called the third-order MRR switches

11
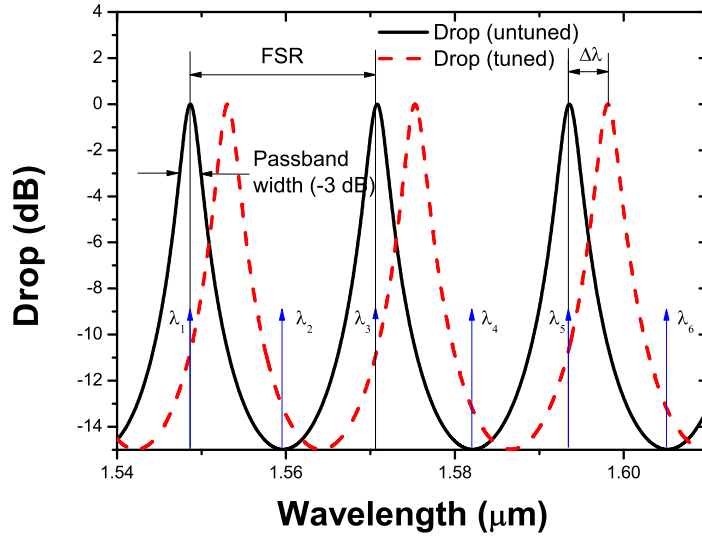
Figure 2.2. Schematic drop transfer function of a microring resonator. Relevant parameters for designing optical switches: single-channel passband width (usually at -3 dB), free spectral range (FSR), and tuning spectral range.

since there are three MRRs cascaded.

(a) MRRs with perpendicular waveguides

(b) MRRs with parallel waveguides
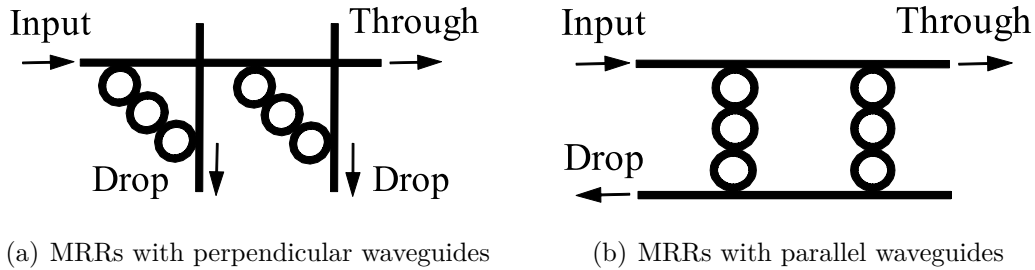
Figure 2.3. Two basic microring resonator switch structures

2.2 State of the Art of Wavelength Tuning Technologies for Microring Resonators

In this section we summarize the most relevant works in the literatures regarding wavelength tuning technologies for microring resonators. As introduced above, the

12

resonant wavelength of a MRR can be shifted or tuned by changing the refractive index of the MRR waveguide. Three technologies have been mainly reported to change the refractive index of the material in the ring waveguide for switching applications. The first one is based on electro-optic effect as mentioned above. In fact, in this effect the refractive index of the material for a microring waveguide is changed by changing the concentration of injected charge carriers [32]. The second one uses thermal-optic effect [28, 33], in which the refractive index of a material is modified by heating the microring resonator. The refractive index of the material varies with the change in the temperature inside the material. The third one uses free carrier dispersion induced by single-photon [34] or two-photon absorption through a pump laser [35]. There are other tuning techniques such as the tuning technique to exploit chem-optical effect. In the effect, when the chemical compositions of a material are changed, its refractive index change. This effect is widely used for micro-resonator based sensors [36]. We neglect its analysis for switching applications.

Microring resonators have been reported to be made of silicon (Si), silicon nitride (SiN), silicon oxinitride (SiON), tantalum pentoxide (Ta_2O_5), doped silicon dioxide (SiO_2), GaAs-AlGaAs and polymethyl methacrylate (PMMA). Silicon is one of widely used materials in large scale integration and there are a lot of mature processes to fabricate silicon-based devices in efficient cost. Integrated silicon photonics is the natural choice for chip-based, high-speed optical signal processing due to its compatibility with CMOS technology and transparency to standard telecommunication wavelengths. This survey chapter focuses on silicon microring resonator-based switch devices that have been successfully fabricated and experimentally demonstrated. In the following sections we introduce different devices classified according to tuning technologies. Furthermore, for different tuning technology, we introduce the device details with different number of rings.

2.2.1 Electro-Optic Microring Resonator Switches

A microring resonator switch operation is based on light propagation controlled by the change of the refractive index of the material used. Silicon lacks inversion symmetry crystal structure and a large electro-optic coefficient, thus it does not lend itself to the mechanism able to change the refractive index by an applied electric field based on Kerr effect. However, the refractive index in heavily doped silicon can be changed by injecting electrons and holes through a p-i-n junction based on plasma dispersion effect [9].

Changing the injection currents of the electrodes leads to the change of the injected electron and hole concentrations in the silicon waveguides, resulting in the change of the refractive indices of the MRR waveguides. Approximate change of the

refractive index of silicon at the wavelength of 1.55 μm is [37]

$$\Delta n = -[8.8 \times 10^{-22} \cdot \Delta N + 8.5 \times 10^{-18} \cdot (\Delta P)^{0.8}] \tag{2.1}$$

where ΔN is electron concentration change in cm^{-3}; Δp is hole concentration change in cm^{-3}.

First-Order Electro-Optic microring Resonator Switches

Q. Xu et al. reported in 2005 [9] a microring resonator device with high-speed change of the refractive index of silicon using electro-optic effect. The reported device shows a breakthrough in the electro-optic tuning technology since it is three orders of magnitude smaller than the previous one demonstrated, and it is able to be used to modulate optical signals at 1.5 Gbps. The report has more than one thousand citations up to now. The schematic of the microring resonator structure with a p-i-n junction is shown in Fig. 2.4. Although the two-port configuration is suitable for the modulation of optical signals, the working principle of this device supposes the first step to develop optical switches, filters, and other devices. Figure 2.5 shows the transmission spectra of the optical output at the resonant wavelength before and after injecting electrons and holes through applying bias voltage on the p-i-n junction embedded in the microring resonator device. This transmission spectra confirm that the bias voltage leads to blue shift of the resonant wavelength of the microring resonator, i.e. the resonant wavelength is decreased due to decrease in the refractive index of the waveguide of the microring resonator.

Secon-Order Electro-Optic Microring Resonator Switches

A silicon photonic microring resonator electro-optic switch composed of two coupled resonators ($R = 5$ μm) was fabricated and experimentally demonstrated [38, 39]. Figure 2.6(a) shows the view scanning-electron-microscope (SEM) image of the silicon photonic microring resonator electrooptic switch. Its spectrum of resonant response is shown in Fig. 2.6(b).

The experiment is performed by simultaneously electrically biasing both microring resonators. Both of the cavities are biased with a square wave signal at a 100-ns period with a 50% duty cycle, producing 50-ns optical gating packets at both output ports. The key results from the experiment are the following. Rising and falling times (10% to 90% of the signal) of 1.46 and 1.3 ns for through port, 1.71 and 0.87 ns for drop port, respectively, are obtained. 14-dB of optical extinction ratio (ER) for signals egressing from both output ports of the switch is observed. Packet transmission of the 40-Gb/s DPSK signal at the wavelength of 1559.5 nm is successfully realized with power penalties of 0.6 and 2.4 dB for through port and drop port
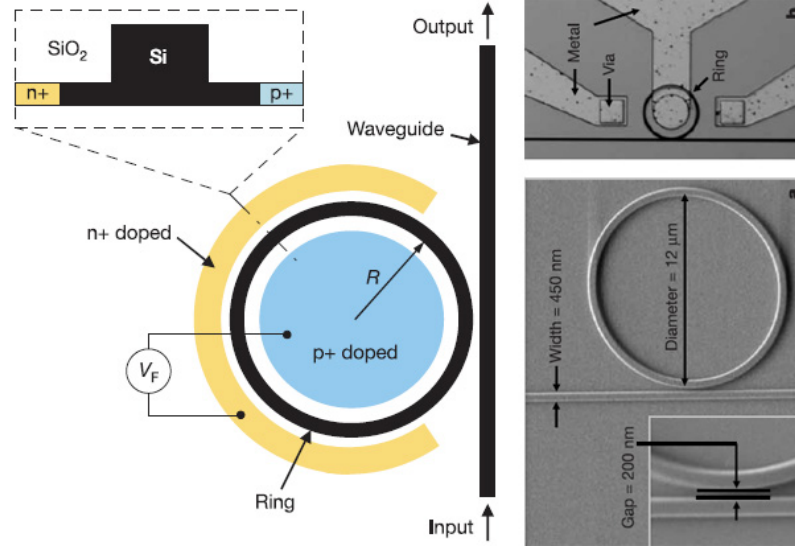
Figure 2.4.   Schematic layout of the ring resonator-based modulator (Left). The inset shows the cross-section of the ring with the radius R = 6 μm. V_F is the voltage applied on the modulator. Scanning-electron-microscope (SEM) and microscope images of the fabricated device (Right): (a) Top-view SEM image of the ring coupled to the waveguide with a close-up view of the coupling region. (b) Top-view microscope image of the ring resonator after the metal contacts are formed [9].

signals, respectively. The switch shows a 9-nm free spectral range (FSR) and -3-dB passband width of 1.1 nm at its drop-port. In a word, fast electro-optical switching speeds in the order of 1 ns were reported [38, 39], indicating that the MRRs are suitable for performing fast-speed optical switching.

High-Order Electro-Optic Micro-Ring Resonator Switches

In order to achieve large flat-top pass bandwidths and high optical-extinction-ratios, multiple-microring coupled structures have been proposed for optical switching [40]. Multiple-microring coupled structures are named as high-order mircoring resonator devices in which the dropped wavelengths propagate through several microring resonators. Light propagates from one microring to another one by direct light coupling between the two rings.

X. Luo et al. reported in [40] that an electro-optically tunable switch consisting of 10 cascaded coupled-racetrack microring resonators integrated with lateral p-i-n diodes in silicon on insulator was fabricated as shown in Fig. 2.7 using CMOS-compatible fabrication process. In the 10 cascaded microring resonator structure each ring has a footprint dimension of 20 μm by 40 μm. Up to 30 Gb/s signal switching capability is supported. Other important results reported in [40] are the

15
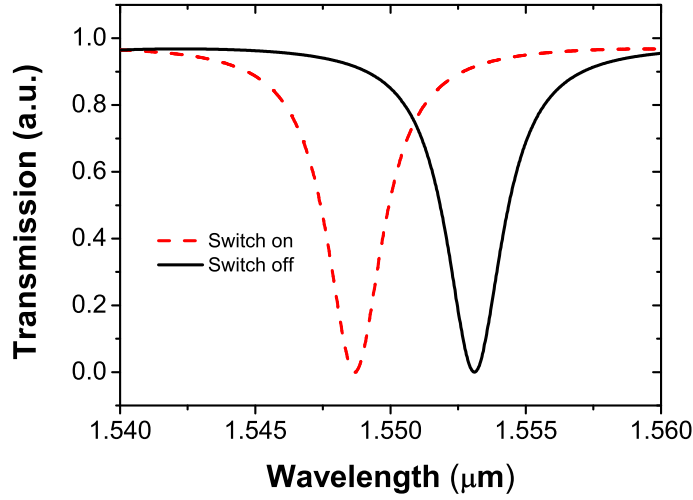
Figure 2.5.   Light transmission spectra of a microring resonator before (solid line) and after (dashed line) a bias voltage is applied. The bias leads to decrease in the resonant wavelength that is attributed to reduction in refractive index of the waveguide of the microring resonator.
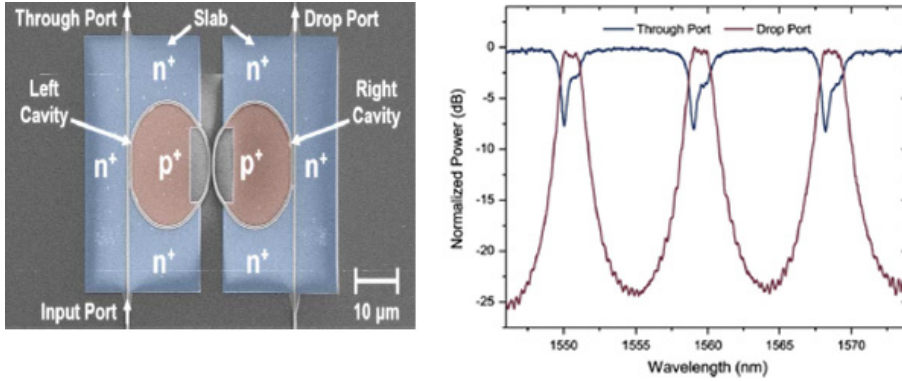
Figure 2.6.   (a) Top-view scanning-electron-microscope (SEM) image of the silicon photonic microring resonator electro-optic switch. (b) Spectra of the silicon photonic microring resonator electro-optic switch for both output ports in the passive state [38, 39].

dynamic response of the electro-optic switch from the throughput and drop ports by switching 20-Gb/s signals. Measured results show a periodic transmission bands with 6 nm free-spectral range, 80∼140 GHz bandwidth and ∼ 50 dB drop-port extinction ratio. The on/off ratios are respectively ∼ 10 dB and 45 dB in throughput and drop ports, with ∼ 1 ns switching time. The throughput losses range from 3.1 to 4.9 dB, while the drop losses range from 4.3 to 5.9 dB.
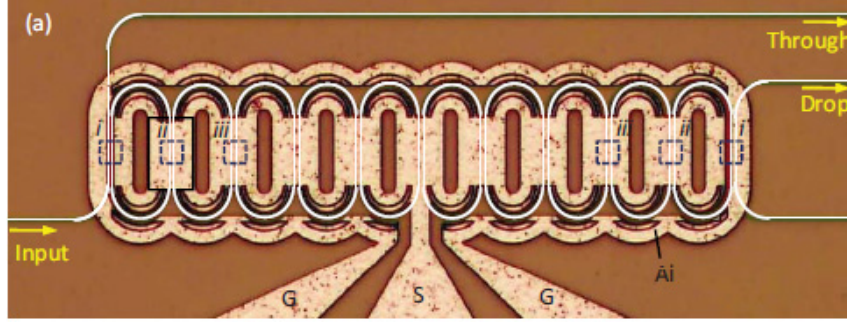
Figure 2.7. Optical microscope image of the fabricated tenth-order coupled-microring-based switch integrated with lateral p-i-n diodes [40].

2.2.2 Thermo-Optic Microring Resonator Switches

The refractive index of silicon can be changed by changing its temperature. For the thermo-optic tuning, the MRR switches must have electric heaters located on their MRRs in order to change the temperature of the MRR waveguides. The refractive index change of silicon yields a resonant wavelength shift of a microring resonator, thus switching a given optical signal in different outputs. The refractive index is changed according to $\Delta n = K \cdot \Delta T$, ΔT being the temperature variation of the waveguide and K the thermo-optic coefficient of silicon [41]. In the MRRs made of silicon material, approximate thermal change of the refractive index at the wavelength of 1.55 μm is [37]

$$\Delta n = 1.86 \times 10^{-4} \Delta T \qquad (2.2)$$

where ΔT is the temperature change in ^oC. That is, 1 ^oC temperature difference between the waveguides in the MRR switches leads to the difference of the refractive indices of 1.86×10^{-4}.

First-Order Thermo-Optic Microring Resonator Switches

F. Gan et al. reported in [42] a large resonant wavelength shift of $\Delta \lambda \sim 20$ nm of a 7-μm-radius silicon microring resonator. Figure 2.8 shows the fabricated microring resonator (dashed line) which is located below a Ti multi-wire structure heater with a diameter of 20 μm. Figure 2.9 shows the shifted drop-port transfer functions and the free spectral range of 16 nm of the MRR when different powers are applied to the heater. The experimental measurements report a switching rise time of 7 μs and a switching fall time of 14 μs.

Single microring resonators are used as optical switches to configure more complex structures such as the 4 × 4 router [28] as shown in Fig. 2.10(a). Each microring

17
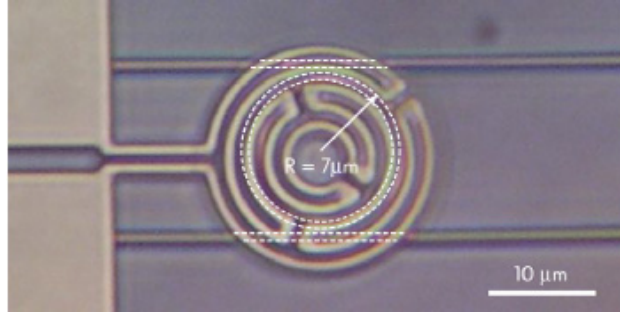
Figure 2.8. Optical micrograph of fabricated heater above tunable silicon microring resonator [42].
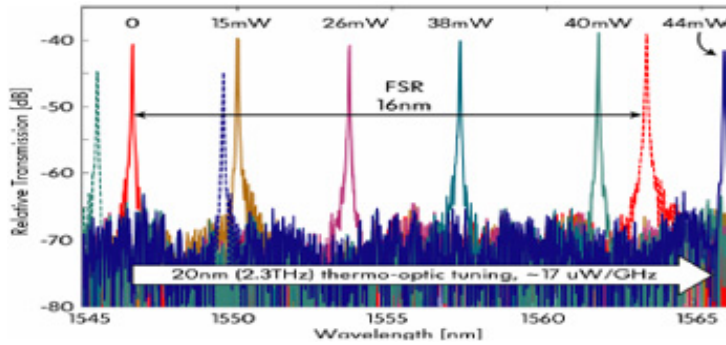
Figure 2.9. Drop-port transmission spectra for different tuning powers, showing a large tuning range of 20 nm which exceeds the 16 nm FSR of the resonator [42].

resonator of 10-μm radius is used as a switch controlled by a heater above itself exploiting thermo-optical effect. The detail of a MRR is shown in Fig. 2.10(b). The resonant wavelength of the ring resonator at 1550 nm is tuned within a range of 10 nm. When electric power is applied to the heater, the resonant wavelength of the resonators is shifted at a rate of 0.25 nm/mW. Sherwood-Droz et al. [28] also showed some combination of non-interacting paths through the router, and at most one microring resonator is used for one path. All optical paths show a maximum extinction ratio of 20.79 dB at drop or throughput port for a routed signal, and a pass bandwidth of around 38.5 GHz corresponding to a bandwidth of 0.31 nm at the wavelength of 1550 nm. The free spectral range is 8.8 nm. The average insertion loss between all the possible paths through the 4 × 4 router is 0.51 dB.

Based on single microring resonator switch controlled by the thermo-optic effect, a spatially non-blocking five-port optical router is experimentally demonstrated [29]. Figure 2.11 shows the optical router fabricated on a silicon-on-insulator (SOI) platform using standard CMOS processing. Each microring resonator has a radius of 10 μm and the total footprint of the device is about 440 × 660 μ m^2. The results show that all the microring resonators achieve -3-dB bandwidths of larger than 0.31
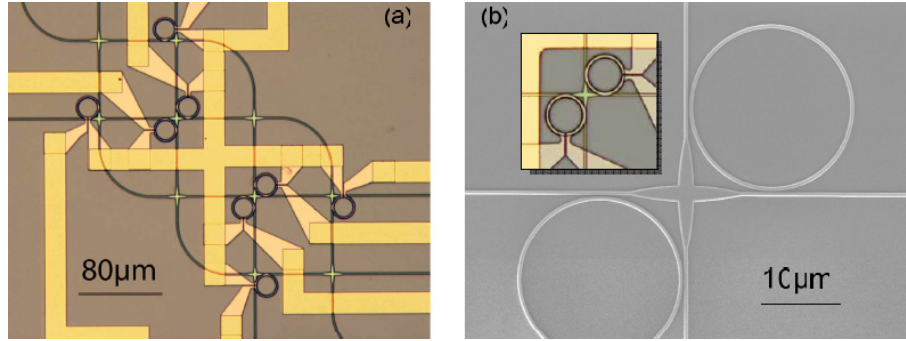
Figure 2.10.   (a) Microscope image of a 4 × 4 router shows gold contacts to nichrome heaters above the microrings. (b) An SEM image shows the details of the fabricated waveguide crossing and coupled rings (Insert shows close-up of heaters) [28].

nm (38 GHz), and extinction ratios higher than 21 dB for through ports and 16 dB for drop ports. The free spectral range of a microring is approximatively 10 nm. Total insertion loss of a single microring is ∼8 dB, which includes propagation loss, crossing loss, and coupling losses between silicon waveguide and input/output lensed fibers. The average wavelength shift is 4.8 nm for the microring resonator from OFF state to ON state. 12.5 Gbps high-speed signal transmission experiments showed high quality routing functionality of the optical router.
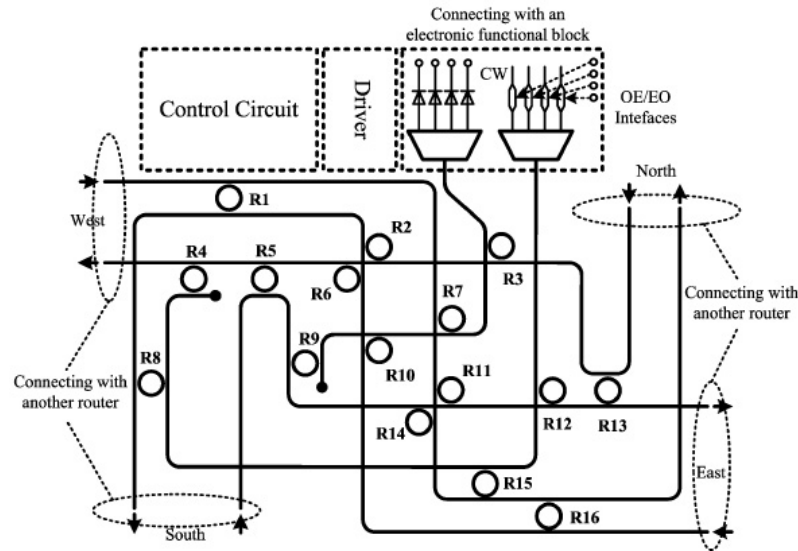
Figure 2.11.   Schematic layout of the five-port non-blocking on-chip optical router [29].

Here we show two different switch devices made of single racetrack shape microring resonators. Figure 2.12 shows the first example of switch based on two single

racetrack-shape microrings used to build a 2 × 2 router architecture that can support signal throughput capabilities up to 320 Gb/s [30]. The microring resonator switches are controlled by thermo-optic effect. In the racetrack resonators, the radii at the bending sections are 5.5 μm and the lengths of the straight sections are 4 μm. The free spectral ranges of the switches are 36 nm, the drop resonance at 1520 nm has a -3-dB bandwidth close to 12 nm, while the corresponding extinction ratio for the drop-port resonant peaks is close to 18 dB. Insertion losses for the through and drop ports are 10 and 12 dB, respectively.
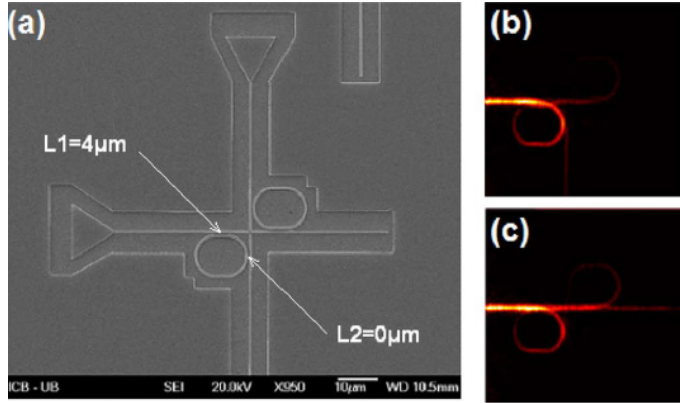
Figure 2.12.   (a)SEM image of two racetrack-shape microring resonators as optical switches using thermo-optic effect [30].(b),(c) Real time image when light is guided into the Drop and Through port, respectively.

Figure 2.13 shows the second example of racetrack-shape microring-based switch used to build a reconfigurable multiplexing device fabricated on a SOI platform [43]. The microrings have bending radii of 4 μm and straight coupling lengths of 2 μm. Each microring is controlled independently through the thermo-optic effect of silicon, and one wavelength is dropped or added from one ring. The measured results show a FSR of 19 nm, a passband width of 0.2 nm, an insertion loss of 1 dB and an ON/OFF extinction ratio of 23 dB. The results show that a wavelength shift of ∼5 nm in the transmission spectra at the drop port of one microring is achieved when heating is applied. When the heater is driven by a 20-kHz square-wave voltage signal, the temporal response at the drop port of one ring resonator shows a time constant of 9 and 6 μs for the rise edge and the fall edge respectively.

Second-Order Thermo-Optic Microring Resonator Switches

Thermal-optic tuning microring-based switches can be integrated in more complex wavelength division multiplexing structures. Two examples that use the second-order microrings (i.e. two rings per switch) are presented. The first example uses thermo-optically tuned microring resonators to switch four channels in integrated
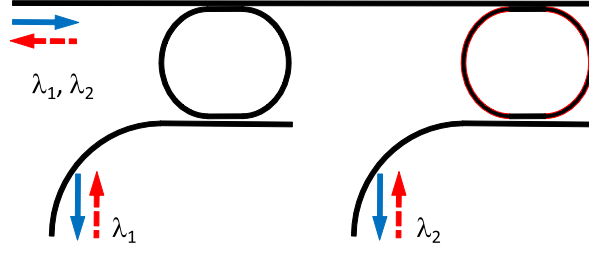
Figure 2.13. Two single microring resonators are used to build the (de)multiplexers. One wavelength is dropped or added after independently switching one ring on using thermo-optic effect [43].

SOI waveguide boards [44]. As shown in Fig. 2.14, four groups of the second-order microring-based switches perform a demultiplexing functionality filtering the output optical signals at different wavelengths. The filtered optical signals are sent to all-optical wavelength converters (AOWCs). Titanium heaters are employed for heating up the MRR structures and changing the effective refractive indices of the microring resonators for wavelength fine-tuning. The diameters of the microring resonators are 18 μm. The transmission spectra at the through and drop ports of the packed devices are measured. The measured results show that each switch has a free spectral range of 5 nm, a passband width equal to 0.04 nm, an extinction ratio of 35 dB, and a total insertion loss (including the losses of both the second-order microring resonator switches and all-optical wavelength converters) of 4.5 dB. The structure is tested with a signal transmission capacity of 160 Gbit/s (40 Gb/s per channel) at the wavelength of 1550 nm.
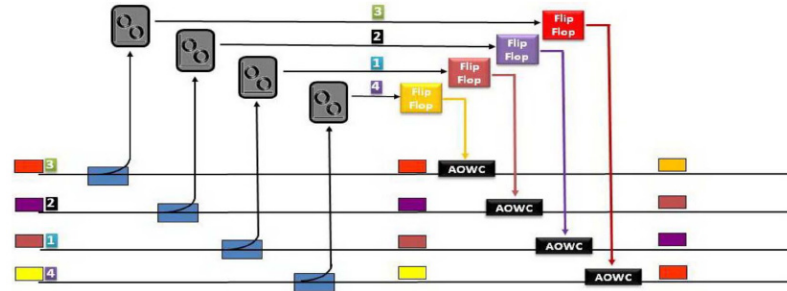
Figure 2.14. Schematic structure of the four-channel second-order thermo-optic microring resonator switch architecture [44].

The second example uses the second-order microring resonators to control the wavelength pass bands and spacings of 20 channels for on-chip wavelength-division-multiplexing systems with thermo-optic tuning technology as shown in Fig. 2.15 [45].

21

All the micoring resonators are fabricated on a SOI wafer and have a radius of 6.735 μm. Light signals from input ports A and B are dropped into the drop ports A_i, and B_i ($i = 1, 2, ..., 20$) respectively, i.e., light propagates along path $A - A_i$, or $B - B_i$. Both propagation directions have identical output responses. The microring resonator reconfigurable filterbank demonstrates precise tuning of eleven (out of the twenty) channels, with a channel spacing of 124 GHz (~ 1 nm) and crosstalk between channels of about -45 dB. The free spectral range is 16 nm. The insertion loss (from input towards drop port) for all channels ranges from 1.5 to 2.5 dB. Both examples of the second-order thermal-tuned microring resonators demonstrate that the second-order MRRs are suitable for on-chip wavelength-division-multiplexing applications.
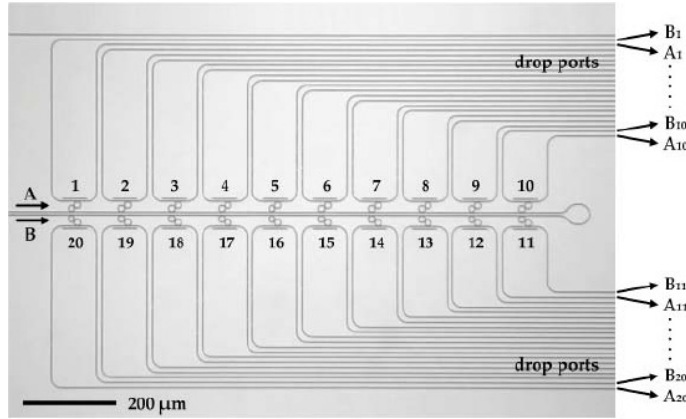
Figure 2.15. Optical micrographs of fabricated filterbanks with twenty channel counter-propagating [45].

Third-Order Thermo-Optic Microring Resonator Switches

Sharper transfer functions and larger extinction ratio can be obtained when the number of rings coupled together in a microring structure increases (i.e. the order of the microring resonator increases). Thermally tuning the third-order microring resonators made of silicon waveguides are used for tunable filtering in WDM applications [46]. Figure 2.16 shows the third-order microring resonator switches fabricated. Their experimental results demonstrate flat-top spectral passbands with $\sim$0.65 dB of intraband ripple, an out-of-band rejection ratio over 40 dB, a -3 dB bandwidth of 0.38 nm, and a free spectral range of 10 nm. The microring resonators have radii of 10 μm and the MRR switch shows an insertion loss lower than 0.9 dB. The measured response spectra show a tuning efficiency of 48.4 mW/nm. Applying 10-kHz thermal tuning signals, the dynamic measurement demonstrates a 12.63-μs

rise time when the signal intensity increases from 10 to 90%, and a 6.31-μs fall time when the signal intensity decreases from 90 to 10%, respectively.
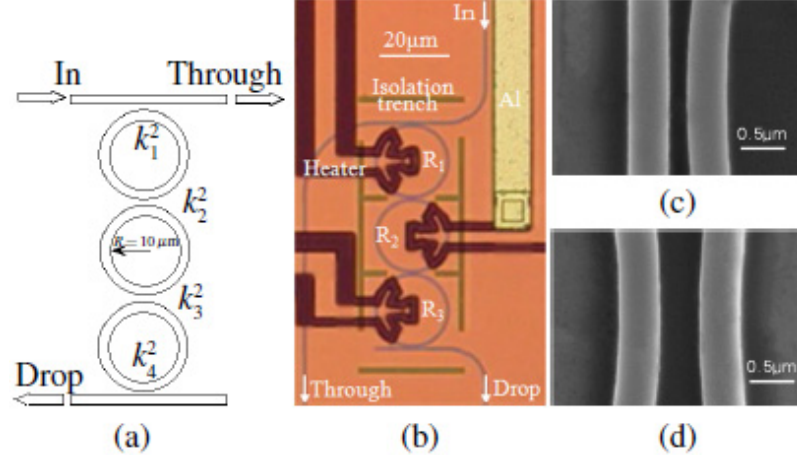
Figure 2.16.   (a) Schematic structure of the third-order MMR filter. (b) Micrograph of the thermally tunable filter. Scanning electronic micrograph of the (c) bus ring and (d) ring-ring coupling regions [46].

C. Stamadis et al. [47] used three thermo-optic tuning silicon mirocring resonators with diameters of 6 μm to perform switching. The obtained results show a -3-dB bandwidth of 1.4 nm, a free spectral range of 28 nm, an extinction ratio of 22 dB and insertion losses lower than 3 dB. The device is tested with the signals of 160 Gb/s.

Fourth-Order Thermo-Optic Microring Resonator Switches

The fourth-order thermo-optic microring-based switches may provide very high extinction ratios and low crosstalks. Y. Goebuchi et al. reported in [31] a fourth-order microring-based structure for multi-wavelength selective switching. The switching is realized through independent thermo-optic tuning of series-coupled microring resonators, and the series-coupled microring resonators can switch arbitrary wavelength channels without blocking other wavelength channels during the tuning intervals. Reported results show a high extinction ratio of 39.0 - 46.6 dB and a crosstalk of 19.3 - 24.5 dB.

Figure 2.17 shows the structure of the wavelength selective switch [31]. The round trip length of the racetrack resonator for the quadruple series-coupled microring resonator is approximately 610 μm, and the curvature radius of the bending part of the racetrack resonator is 55 μm. Racetrack shaped heaters are formed on the top of individual racetrack resonators.

By cascading two fourth-order microring-based switches [48], the measured results show that each switch has the spectral passband width of 0.21 nm and a free spectral range of 2.2 nm. The bandwidth of overall spectral response are doubled (0.42 nm) when switching on the two switches. The results show that, by means of the ON/OFF switching capability of the two switches, the overall bandwidth can be digitally controlled. Therefore, the two-switch architecture can be used as a switch device with variable bandwidth that is required in optical networks.
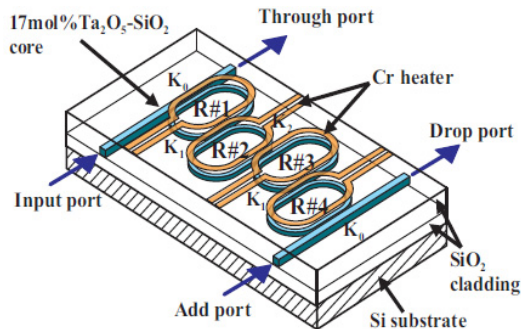
Figure 2.17. Perspective view of a wavelength channel selective switch using quadruple series-coupled MRRs [31].

2.2.3 All-Optical Microring Resonator Switches

Here we will review the most relevant all-optical microring-based switches reported in the literatures. In this type of switches, tuning the resonant wavelengths of the microring switches is realized by changing the refractive indices of the MRR waveguide materials when high intensity laser beams pump the MRRs. High intensity laser beam induces optical Kerr effect inside the MRR waveguides to change the refractive indexes of the materials. In some cases, a laser beam can induce plasma dispersion inside microring resonators resulting from single photon or two photon absorption [49], [34], thus leading to the change of the refractive indexes of MRR materials. Pumping laser beam may be input into the microring resonators by light coupling with optical couplers as shown in Fig. 2.18 [35], or may be directly focused on the surfaces of microring resonators from the tops of the microrings as shown in Fig. 2.19 [49]. In addition, it is also possible to exploit the change of refractive indexes of silicon materials inside the microring resonators through thermal-optic effect by focusing laser beams on the microring resonators to heat the materials [50]. So far, only single ring devices (i.e. the first-order microring resonators) have been reported for the optical tuning MRR switches for two possible reasons. The first one is that high coupling loss between MRR waveguides leads to low pumping power in the microring that can not effectively change the refractive index of the MRR

waveguide, when the pumping laser beam is coupled into the MRRs by using optical coupling scheme. The second is that several lasers are used to couple laser beams into the MRRs or several laser beams are needed to irradiate multiple MRRs for high-order MRR switch devices, resulting in large and complex space structures that do not benefit to the integration of the MRR devices.
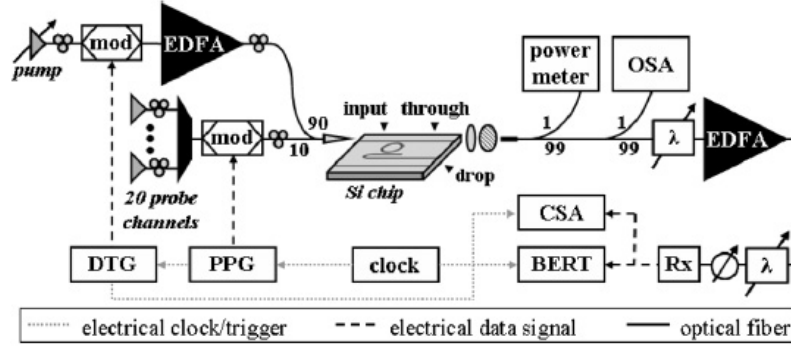
Figure 2.18. Diagram of the device structure and experimental setup used for active measurements. (CSA: communications signal analyzer; DTG: data timing generator; λ: tunable grating filter; mod: LiNbO modulator; OSA: optical spectrum analyzer; Rx: receiver) [35].
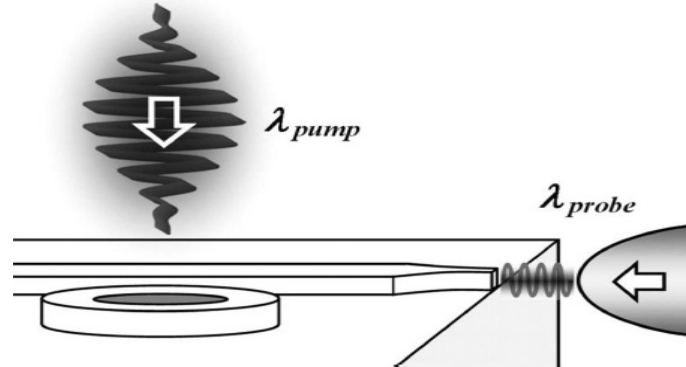
Figure 2.19. Scheme of laser pumping microring resonator from its top. Probe light is coupled into the bus waveguide of the microring resonator through optical coupler [49].

Simultaneous all-optical switching of tens of continuous-wave wavelength channels is reported in a microring resonator-based silicon broadband 1×2 comb switch [35]. The state of the switch is toggled by modifying refractive index of the ring via two-photon absorption induced by a pump laser source operating at 1.55-μm wavelengths. The 1×2 all-optical comb switch shown in Fig. 2.20 uses a 100-μm radius silicon ring resonator. It has a footprint of $\sim$0.04 mm^2. The experimental setup in Fig. 2.18 shows that the combined pump and probe signals pass

through the switch and are analyzed using a power meter and an optical spectrum analyzer. The transmission spectra of both drop and through ports, together with a third port (a reference waveguide with the same length and cross section as the through port waveguide), are shown in Fig. 2.21. The results show simultaneously switching 20 continuous wave wavelength channels with the spacing of ∼0.8 nm using the same pumping laser. The free spectral range that characterizes the reported microring resonator is 0.8 nm in concordance with the larger radius of this device. The results show an extinction ratio of 14.5 ∼ 18.7 dB, a passband width of 0.085 nm (10.6 GHz) for all the channels, a switching rise/fall time around 1 ns, and the insertion loss of 2.3 dB at the drop port. The switch overcomes the small bandwidth of the traditional ring resonator since it simultaneously switches on or off all the channels, and it may work in wavelength division multiplexing applications.
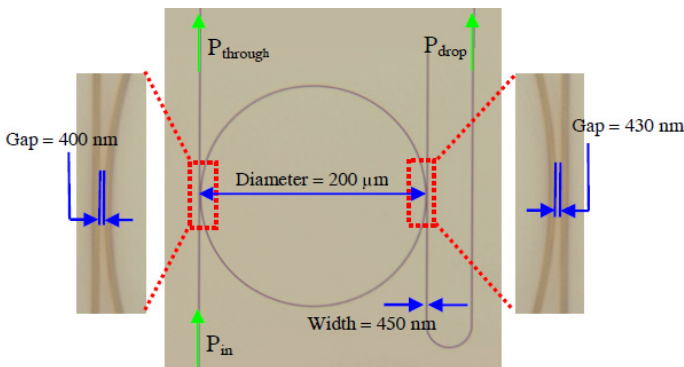
Figure 2.20. Top-view microscopic picture of the fabricated 1×2 all-optical comb switch [51].
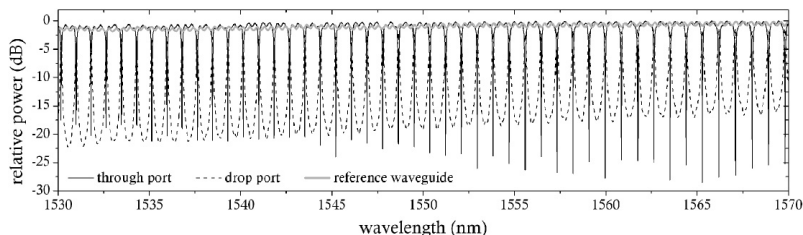
Figure 2.21. Relative transmission spectrum over the C-band of the through port (black, solid), drop port (black, dashed), and output of the reference waveguide (gray, solid) [35].

A femtosecond pulse laser with a central wavelength of 415 nm is reported to be used to pump the microring resonator [51] with the same geometric size as the microring in [35] by focusing the pump pulses on its top surface. The result shows that it can enable switching of a large number (∼40) of wavelength channels spaced

by ∼0.85 nm. Overall optical bandwidth spans 33 nm. The switching time is less than 1 ns. The resonant wavelengths of the ring are shifted by 0.2 nm after pumping, i.e. the wavelength tuning range of the microring resonator is 0.2 nm. The insertion loss of the ring is less than 3 dB over the entire spectral range from 1532 nm to 1565 nm.

A first-order microring-based 2 × 2 all-optical control switch is reported in [50] as shown in Fig. 2.22. The switch has nanosecond-scale switching time (< 2 ns), ON/OFF extinction ratios up to 11.5 dB, and insertion losses of ∼1 dB at a data rate of 10 Gb/s for static and dynamic operation. The FSRs of the resonators are 1.6 nm and the resonator modes have -3-dB bandwidths of 0.1 nm (12.5 GHz) on average. The experimental setup is shown in Fig. 2.23. Two main pump lasers at the wavelengths of 1536.6 and 1563.1 nm and an external laser at the wavelength of 532 nm are used to tune the resonant wavelengths of two microring resonators, resulting in 2 × 2 switching function. The experiment is performed using 6 wavelength channels from 1542.9 nm to 1559.8 nm. This device can be an important building block in more complex routing structures to provide network designers with the imperative 2 × 2 switching function. The 2 × 2 switch facilitates the design of more complex routing structures, allowing the implementation of multi-function integrated optical networks.

Input	Pump state	Output
In0	OFF	Out0
In0	ON	Out1
In1	OFF	Out1
In1	ON	Out0
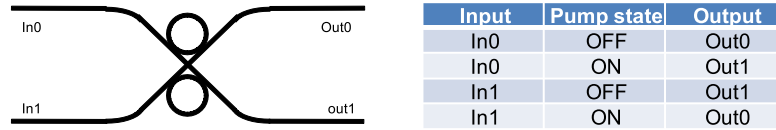
Figure 2.22.   Schematic of the 2 × 2 switch layout and table for the switching states.
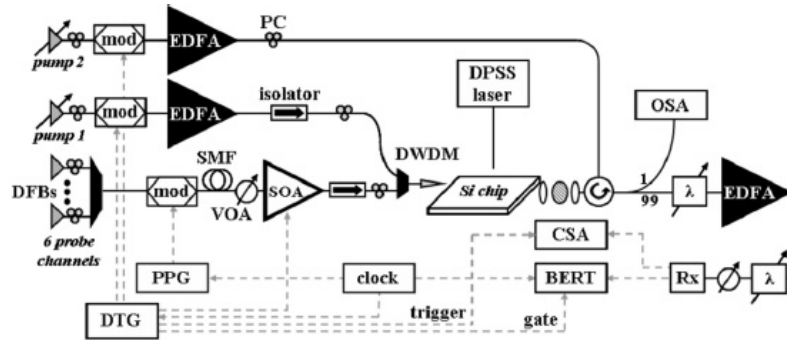
Figure 2.23.   Diagram of the experimental setup. Solid lines represent optical fiber, while dashed lines represent electrical cable [50].

The all-optical pumping scheme demonstrates the possibility of the device to

27

achieve fast switching (2 ns) with high extinction ratios. It is worth noting that all-optical microring resonator switching can be also realized by optically controlling intra-cavity loss via Raman scattering [52]. However, in actual implementations, electronic carrier injection instead of optical pump scheme is feasible to tune the refractive index of a MRR for optical switching applications. Not only would the optical pumping scheme be impractical in structures, but also electronic carrier injection is expected to improve the speed, insertion loss, and power requirements of the switches, while also providing a more stable switching scheme [50].

2.3 Comparison of Microring-Resonator-Based Switch Device Performances

The performances of microring-resonator-based switch devices are strongly dependent on their wavelength tuning methods, architectures, physical and geometrical parameters. Their passband widths and insertion losses are dependent on the numbers and the diameters of the microring resonators consisting of the switching devices as well as the coupling behaviours between the waveguides of the microring resonators.

Small microring devices can achieve large wavelength tuning ranges and large free spectral ranges. It is reported that when microring resonator diameters are decreased from 3 to 2 μm [53, 54], their free spectral ranges increase from 52 to 80 nm, while their bandwidths increase from 1.2 to 3.3 nm, indicating that the spectral bandwidths of microring resonators increase if the diameters of microring resonators decrease.

As mentioned previously, large flat-top spectral passband widths can be achieved if high-order coupled microring structures are used as optical switches in the optical interconnect systems [39, 45, 55]. The passband of a microring-resonator switch may become wider and flatter using high-order microring-resonator switch structure instead of single-microring-resonator structure [39]. It is reported that a flat-top pass band of 310 GHz is achieved using the fifth-order microring-resonator switch structure [55].

The difference between the switch devices using different wavelength tuning technologies is discussed as follows.

2.3.1 Electro-Optic Microring Resonator Switches

The refractive index of silicon can not be tuned directly using Kerr effect as mentioned in Section 2.2. However, the refractive index of heavily doped silicon can be changed by injecting electrons and holes through a p-i-n junction based on plasma

dispersion effect. Moreover, the effective refractive index of the waveguide for a microring resonator can be changed by using electro-optic material instead of silicon oxide for the cladding layer of the waveguide of the microring resonator, i.e., the core layer of the waveguide is made of silicon while the cladding layers are made of the electro-optic material. Using this waveguide, the resonant wavelength of a microring resonator can also be tuned by applying electric field on the microring resonator.

Microring switch devices can achieve faster switching speed using the electro-optic tuning technology based on plasma dispersion effect. Their switching times are on the order of ∼1 ns [39,40]. Using high-order microring-resonator structures, flat-top spectral passbands of the microring resonator switches are able to be achieved. A third-order microring add-drop filter consisting of silicon microring resonators with the diameters of 5 μm is reported to have a flat passband width of ∼1 nm (125 GHz) at the wavelength of 1550 nm and a free spectral range of 32 nm [56]. The ∼1-nm wide passband can accommodate two, five, ten, and twenty channels in optical networks at the spacings of 50, 25, 12.5, 6.25 GHz [57] respectively, where 6.25 GHz is defined as the frequency granularity of flexible optical networks. A compact silicon-on-insulator add-drop filter composing of microring resonators with a 3-μm diameter for wavelength-division-multiplexing on-chip interconnect applications [54] is reported to have a passband width of 210 GHz (1.7 nm) and a FSR of 52 nm (6.34 THz), with only 2.9-dB insertion loss and a drop-port extinction ratio as high as 25 dB. The device could accommodate up to 30 high-bit-rate data channels at the spacing of 6.25 GHz within one FSR. However, the channel passband is not flat. It is reported that when the diameter of the microring resonator is reduced to 2 μm, the passband width increased to 410 GHz (3.3 nm) and the FSR increased to 80 nm, which spans almost both the C and L bands [53]. The device would accommodate up to 60 high-bit-rate data channels at the spacing of 6.25 GHz within one FSR.

Advantage: Microring resonator switches with the electro-optic effect have higher switching speed. High throughput microring resonator switches can be fabricated with CMOS-compatible process technology in low cost, and monolithic integration can be realized. The switches have potential to be used in high speed optical communication networks and optical interconnection in networks on-chip.

Drawback: The resonant wavelengths of microring resonators may be shifted due to their high sensitivity to ambient temperature fluctuation caused by the large thermo-optic coefficient of silicon (1.86×10^{-4} K^{-1}). Fortunately, a lot of approaches have been proposed and successfully implemented to mitigate the influence of the temperature sensitivity. Several schemes involving active compensation have been demonstrated, in which heaters provide feedback that dynamically stabilizes the ring resonance [58–60]. There have also been several schemes that involve passive compensation. One scheme is to use polymers with negative thermo-optic coefficient as the cladding materials of MRR waveguides to counteract the positive thermo-optic

coefficient of silicon [61–64]. Recently, a scheme was reported to use a Mach-Zehnder interferometer (MZI) design to stabilize the resonant wavelengths of microring resonators in silicon electro-optic modulators, through the spectrum blueshift with temperature to counteract the spectrum redshift of a conventional microring resonator [65,66]. The degradation from thermal effects can also be mitigated using a pre-emphasized driving signal [67].

2.3.2   Thermo-Optic Microring Resonator Switches

Thermo-optic microring resonator switch devices have large wavelength tuning range while they have slow switching speed. The devices can achieve the wavelength tuning range larger than 20 nm [42]. Typically, their switching times are on the order of 10 μs due to slow thermal diffusion speed. Using the third-order microring-resonator switch structure, a flat-top passband response with a -3-dB bandwidth of 1.4 nm (175 GHz) at the wavelength of 1550 nm and a FSR of 28 nm are reported [47]. This flat-top band can accommodate 28 high-bit-rate data channels at the spacing of 6.25 GHz within one FSR.

Large transmission capacities have been achieved in thermally tuned silicon microring resonator-based router. A 2×2 router architecture was reported to support up to 320-Gb/s throughput [30], using a dual-ring 2×2 thermo-optic switch residing on a SOI photonic motherboard.

Advantage: Thermo-optic microring resonator switch devices have large wavelength tuning ranges. More than 20 nm (2.5 THz) wavelength tuning range has been achieved [42]. They are easy to be fabricated and to be implemented in low cost.

Drawback: The switching speeds of these devices are rather slow. Typically, the switching times are on the order of 10 μs. However, they can be used in the optical communication networks in which fast switching times are not required.

2.3.3   All-Optical Microring Resonator Switches

All-optical microring resonator switching can be realized based on shifting the resonant wavelengths of microring resonators using optically induced plasma dispersion effect, Kerr effect, and optically induced heating effect in silicon material. It can also be realized by controlling intracavity light propagation loss via inverse Raman scattering.

However, silicon does not possess strong nonlinearity and large electric-optic coefficient while Kerr effect is dependent strongly on nonlinear electric-optic coefficient. Hence, high power or extremely high power lasers are needed for all-optical microring resonator switches. In this case, laser will damage the microring resonator structure. Thus, it is not an effective method to use Kerr effect for switching purpose in silicon-based microring resonator devices.

Optically induced heating effect is actually similar to thermo-optic effect. The waveguide material absorbs the energy of a pump laser and the energy changes into heat. The heat changes the temperature of the waveguide, resulting in changing the refractive index of the waveguide material.

Inverse Raman scattering in silicon leads to strong loss at the anti-Stokes wavelength. It could be a scheme to realize all optical control of microring resonator switches using this effect. Currently, the most effective method reported for all-optical microring resonator switching purpose is to use optically induced plasma dispersion effect which results from single photon or two photon absorption.

All-optical microring resonator switch devices can generate high switching speed (less than 1 ns), and tens of channels can be simultaneously switched on or off. A 1×2 all-optical comb switch using a 200 μm diameter silicon ring resonator with a switching time of less than 1 ns is reported [51]. The switch enables simultaneous switching of 40 wavelength channels spaced by $\sim$0.85 nm. The overall optical bandwidth of the device spans 33 nm.

However, the optical pumping scheme is not superior to electro-optic tuning scheme in structures, speed, insertion loss, power requirements, and device stabilities. The devices have very small wavelength tuning ranges and narrow passband widths. Expensive ultrafast pulsed lasers are used to pump microring resonators. The pumping lasers need large space, which may not be suitable for compact optic-electronic integration. The comparison of the three tuning technologies is listed in Tab. 2.1.

Table 2.1.   Comparison of microring resonator-based switch performances

Tuning technology	Switching time	Tuning range	Complexity
Electro-optic	1 ns	2.8 nm [59]	Simple
Thermo-optic	10 μs	>20 nm [42]	Simple
Optical tuning	1 ns	0.2 nm [51]	Complicated

2.4   Conclusions

The chapter was focused on examining wavelength tuning technologies for microring resonator-based switch devices in silicon photonic interconnection networks and optical communication networks. Based on the descriptions above, we draw conclusion as follows:

The resonant wavelengths of silicon-based microring resonators for switching applications in photonic interconnection networks can be tuned through electro-optic

effect, thermo-optic effect, optically induced plasma dispersion effect in silicon material. The performances of microring resonator switch devices are strongly dependent on their wavelength tuning methods, architectures, physical and geometrical parameters. Their passband widths are dependent on the numbers, the diameters of the microring resonators, the physical properties of MRR materials, and the coupling characteristics of the MRRs in the switch devices. In small diameter microring devices, large free spectral ranges, large passband width, and large wavelength tuning ranges can be achieved. In high-order microring switch devices, wide and flat-top spectral passbands can be achieved.

Electro-optic tuning can achieve faster switching speeds ($\sim$1 ns) and suitable wavelength tuning ranges ($\Delta\lambda \sim 2.8$ nm) for MRR switch devices. However, the optical central wavelengths of the passbands of the MRR switch devices may be drifted caused by temperature fluctuation during the carrier injection in the p-i-n junction. This limits the capacity of the signal transmission in optical interconnection systems. Fortunately, the optical wavelength fluctuation can be mitigated using temperature compensation, wavelength track and feedback, MZI interferometer spectrum stabilization, driving signal pre-emphasis, and other relevant techniques.

Thermo-optic tuning provides large wavelength tuning ranges ($\Delta\lambda > 20$ nm) with low switching speeds (10 μs) for MRR switch devices. It is relatively easy to tune the resonant wavelengths of the microring resonators. So far, experimental results demonstrate the maximal supported signal throughput of 320 Gbit/s using thermo-optic tuning micoring resonator devices.

Optically induced plasma dispersion effect inside silicon through single photon and two photon absorption can change the refractive index of a silicon waveguide of a MRR switch device. Experimental results show high switching speeds (less than 1 ns) and tens of channels can be simultaneously switched. However, the optical pumping scheme would be impractical in structures for opto-electronic integration due to large pumping laser dimensions. High pumping laser power is also needed since it is not easy to couple high power directly into the devices due to high light coupling loss. In comparison, electronic carrier injection can increase the switch speeds, decrease the insertion losses, and decrease power consumptions of the switches, while also providing a more stable switching scheme, indicating that the optical pumping scheme is not superior to electro-optic tuning scheme for MRR switch devices in structures, speeds, insertion losses, power requirements, and device stabilities.

Chapter 3

Design of Microring Resonator Devices for Switching Applications in Flexible-Grid Networks

In this chapter, the physical characteristics of microring resonator switching devices are thoroughly analyzed using a model based on the field coupling matrix theory. The spectral response and insertion loss properties of these switching elements are simulated using the developed model. Then we investigate the optimal design of high-order MRR-based devices. First, the structure and the spectral response behaviors of the MRR-based devices are illustrated in Section 3.2. The spectral passband widths and insertion losses of MRR-based switching devices as the functions of several physical characteristics of the MRRs, such as the coupling coefficients between the MRRs, the ring diameters, and the propagation losses in the MRRs, are analyzed and discussed in Section 3.3. In Section 3.4 simple switch architectures based on MRRs are demonstrated as a possible application of the studied elements in flexible-grid networks. Results show that by cascading three microring resonators it is possible to achieve the flat-top passband widths ranging from 6.25 GHz to 3 THz, while having the insertion losses compatible with the use in flexible-grid optical communication networks. The architectures of simple MRR optical switches with limited functionalities are discussed, showing the potential use of MRRs for switching applications in flexible-grid optical networks.

3.1 Introduction

The constant increase of traffic has urged effective use of the available spectral resources in optical core networks. The development of mature and reliable optical orthogonal frequency division multiplexing (OFDM) transmission systems helped

to solve the problem. However, the adoption of optical OFDM systems made inadequate the traditional fixed-grid division of the optical spectrum used in WDM networks. Thus, flexible-grid networks have been introduced as mentioned in Chapter 1

In flexible-grid networks, the fundamental device is a flexible WSS which has to cope with the need to switch channels with variable bandwidths. Early WSSs were demonstrated using integrated optics [68, 69]. Commercial WSSs use free-space optics exploiting MEMS [5] or liquid crystal switching elements [70]. Hybrid integrated and free-space optics WSSs [71] were demonstrated in laboratory. These devices cannot be used in short reach networks such as networks on chip or in board to board or data center interconnects due to their large volumes. The flexible-grid WSS based on AWG described in [72] requires a complex fabrication process and hardly achieves a very narrow steep-edge flat-top passband.

MRRs are instead highly wavelength selective and can be easily integrated on chip. MRRs were studied as filters, switches, modulators, routers, multiplexers for optical communication networks and optical interconnections [73–75]. Wide flat-top passbands can be achieved by cascading several MRRs and by properly selecting structural design parameters [76, 77]. A 1.4 nm wide passband, corresponding to frequency bandwidth of 175 GHz, using three cascaded MRRs, were reported [15]. Compact 5-th order ring resonator optical filters based on submicron silicon photonic wires with a flat-top pass band of 310 GHz were demonstrated [78]. A maximal bandwidth of 6 nm (750 GHz) was reported [79] . However, devices for flexible-grid networks have stricter requirements.

Tuning actions are required to select a proper passband or change a passband, depending on the switching needs. Thermal [80, 81], electrical [40] or optical tuning technologies can be exploited to dynamically select a proper set of wavelengths for different switching speeds. Optimizing the design of MRRs becomes fundamental to develop MRR switching devices characterized by very narrow or very wide flat-top passband widths.

In this chapter, we investigate the optimal design of high-order MRR-based devices, which are obtained by cascading several microring resonators. First, the structure and the spectral response behaviors of the MRR-based devices are illustrated in Section 3.2. The spectral passband widths and insertion losses of MRR-based switching devices as the functions of several physical characteristics of the MRRs, such as the coupling coefficients between MRRs, the ring diameters, and the propagation losses in the MRRs, are analyzed and discussed in Section 3.3. In Section 3.4 simple switch architectures based on MRRs are demonstrated as a possible application of the studied elements in flexible-grid networks. Finally, conclusions are drawn in Section 3.5.

3.2 High-order Microring Resonator-Based Switch Devices and Transfer Matrix Theory

High-order MRR-based devices are composed of two linear waveguides and several cascaded MRRs, as shown in Fig. 3.1. The device cascading N microrings is named Nth-order MRR-based device. In these devices, it is assumed that all MRRs operate at the same resonant wavelength. The signal from the input port propagates in the first waveguide. The portions of the spectrum at the resonant wavelengths are coupled into the first MRR and they propagate through the $N-1$ remaining MRRs. Finally, the propagating spectrum is coupled to the output waveguide and exits at the drop port. Instead, the portions of the spectrum not correspondent to the resonant wavelengths exit from the through port. In Fig. 3.1, a_n, a'_n and b_n, b'_n, with $n \in [0, 1, 2, ..., N, N+1]$, denote the complex mode normalized amplitudes and their squared magnitudes correspond to the modal powers. k_n represents instead the dimensionless field coupling coefficient, while k_n^2 is the power coupling coefficient. k_0^2 and k_N^2 represent the power coupling coefficients between bus waveguides and MRRs at the signal input port and the drop port.
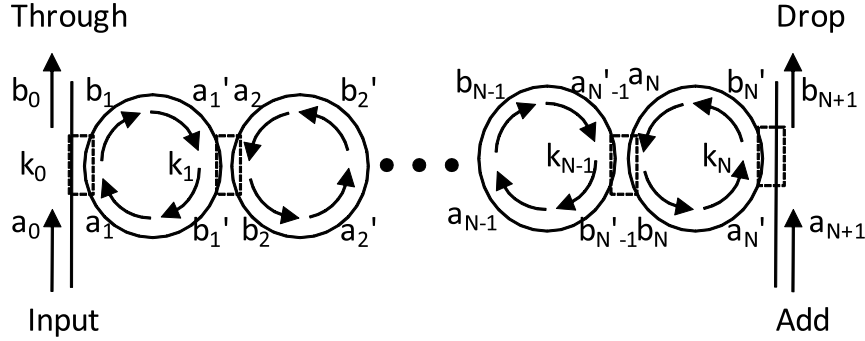
Figure 3.1. Structure of a high-order MRR-based switching device.

To study the response spectrum of MRR-based devices, it is necessary to compute the resulting signal (i.e., b_{N+1}) at the drop port. The computation can be performed based on the field coupling matrix theory [82]. The light propagation in the MRR-based device can be described using the transfer matrix equation as follows:

$$\begin{bmatrix} a_{N+1} \\ b_{N+1} \end{bmatrix} = \prod_{n=0}^{N-1} (P_{N-n} \cdot Q_{N-n}) \cdot P_0 \begin{bmatrix} a_0 \\ b_0 \end{bmatrix}. \tag{3.1}$$

In Eq. 3.1, P_n describes the coupling matrix between the $(n-1)^{th}$ and the nth MRR. In particular, P_0 and P_N correspond to the coupling matrices between the

input waveguide and the first MRR, and between the output waveguide and the last MRR respectively. P_n can be computed as

$$P_n = \frac{1}{k_n} \begin{bmatrix} -t_n & 1 \\ -1 & t_n^* \end{bmatrix}, \tag{3.2}$$

where t_n and t_n^* are the transmission coefficient and its complex conjugate respectively. Furthermore, t_n^2 is the power coupling coefficient such that $|k_n|^2 + |t_n|^2 = 1$ with the simplifying assumption of no external losses in the coupling between bus waveguides and MRRs, and between MRRs.

Furthermore, Q_n, representing the propagation matrix in one MRR, is written as

$$Q_n = \begin{bmatrix} 0 & e^{-i\beta R\pi} \\ e^{i\beta R\pi} & 0 \end{bmatrix}, \tag{3.3}$$

where β is equal to $2\pi n(f)f/c + i\alpha$, $n(f)$ is the frequency dependent effective refractive index, f is the propagating mode frequency, α is the light propagation loss per unit length in the MRRs, and R is the MRR radius.

Finally, Eq. 3.1 can be expressed in the following form:

$$\begin{bmatrix} a_{N+1} \\ b_{N+1} \end{bmatrix} = \begin{bmatrix} A & B \\ C & D \end{bmatrix} \begin{bmatrix} a_0 \\ b_0 \end{bmatrix}, \tag{3.4}$$

Thus, b_0 and b_{N+1}, the signals at the through and the drop ports respectively, can be expressed as

$$b_0 = \frac{a_{N+1}}{B} - \frac{A}{B}a_0, \tag{3.5}$$

and

$$b_{N+1} = \frac{D}{B}a_{N+1} + \left(C - \frac{AD}{B}\right)a_0. \tag{3.6}$$

3.3 Physical Characterization of High-Order Microring Resonator-Based Switch Devices

The MRRs considered in this work are built using silicon waveguides with silicon oxide as cladding. We refer to the waveguides with cross sections of 450 nm wide and 250 nm thick, whereas the thicknesses of silicon oxide cladding at top and bottom are 1 and 3 μm respectively. The effective refractive indices of the waveguides are calculated, using the finite difference method, to be about 3.212 for transverse-electric (TE) polarization mode and 3.023 for transverse-magnetic (TM) polarization mode at the wavelength of 1.55 μm. We keep fixed these values because they depend on the waveguide structures which are the same in all the considered cases. We

disregard the large wavelength shift for different polarization light propagation under resonant condition and we focus on light propagation in TE polarization only for simplicity.

The spectral response at the drop port is influenced by several physical parameters: the number of coupled MRRs, the coupling coefficients between waveguides and MRRs and between MRRs, the MRR diameters, and the propagation losses in the MRRs. In the following sections, we study the effect of each parameter on the spectral response, to determine which is the most suitable high-order MRR-based device to build WSS for flexible grid optical networks. The results are obtained by simulating the behaviors of high-order MRR-based devices using the mathematical formulas reported in Section 3.2. In the figures, arrows are used on the frequency axes to show the ITU-T central frequencies of channels with spacing 100 GHz.

All N MRRs are assumed to be identical in size. If not differently stated, the MRR diameters are set to 20 μm and the light propagation losses to 5 dB/cm. Furthermore, the power coupling coefficients between bus waveguides and MRRs are set to $k_0^2 = k_N^2$, and the power coupling coefficients between MRRs meet the following condition:

$$k_1^2 = k_2^2 = ... = k_{N-1}^2 = 0.25 \cdot k_0^4. \tag{3.7}$$

3.3.1 Sensitivity to Number of Microring Resonators

The desired response spectrum should present a flat-top passband to preserve signal shape and intensity. Figure 3.2 depicts the response spectra at the drop port of Nth-order MRR-based devices, for variable N, with coupling coefficients satisfying Eq. 3.7. A single MRR-based device has a response spectrum that corresponds to a Lorentz curve. In the case of a 2nd-order MRR-based device, the top of the response spectrum is not flat, while the coupling of three MRRs results in a flat-top passband. If more than three MRRs are used, fluctuations in the top passband appear. Thus, we focus on $N = 3$ in the following analysis, i.e., on 3rd-order MRR devices.

3.3.2 Sensitivity to Power Coupling Coefficients and Propagation Losses

The spectral response of a 3rd-order MRR-based device at its drop port is analyzed by varying the coupling coefficients between MRRs, and between the bus waveguides and MRRs.

In Fig. 3.3 the spectral response is shown for different values of the coupling coefficients between the waveguide and the first MRR, while the coupling coefficients between the MRRs are set according to Eq. 3.7. The passband width increases with increasing coupling coefficients. In Fig. 3.4 it is shown that the -3 dB passband width
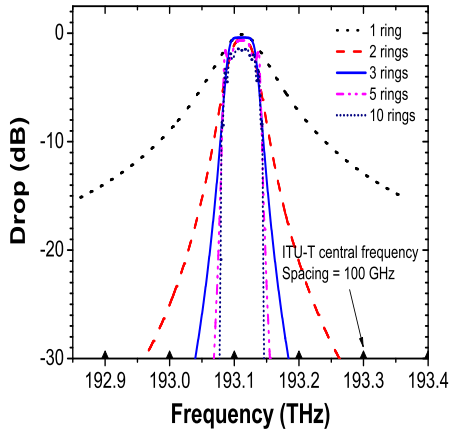
Figure 3.2. Response spectra of Nth-order MRR-based switching device for variable N, with MRR diameter $D = 20$ μm, propagation loss 3 dB/cm and power coupling coefficients $k_0^2 = 0.16$.
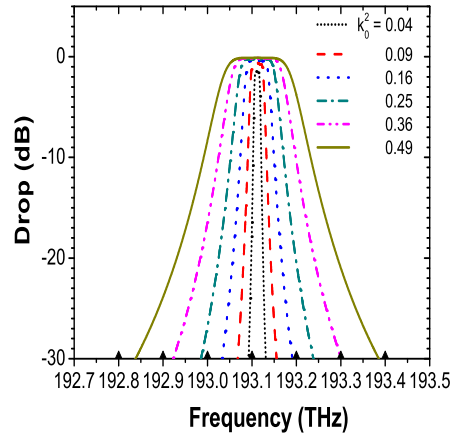
Figure 3.3. Spectral response by varying k_0^2 the coupling coefficients between bus waveguide and MRRs, with MRR diameter $D = 20$ μm and propagation loss 3 dB/cm.
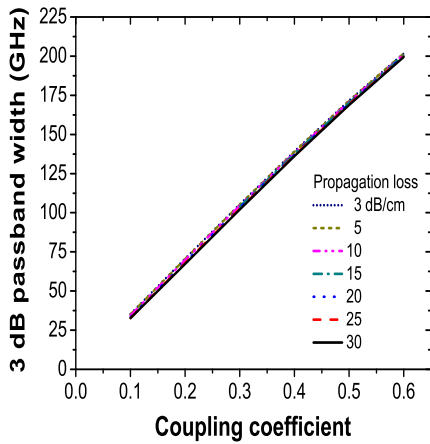
Figure 3.4. -3 dB passband width as a function of coupling coefficients, with MRR diameter $D = 20$ μm.
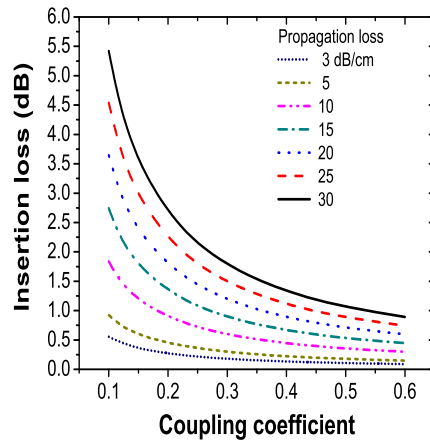
Figure 3.5. Insertion loss as a function of coupling coefficients, with MRR diameter $D = 20$ μm.

of a 3rd-order MRR-based device i) increases linearly with the coupling coefficients. ii) is independent of the propagation losses ranging from 3 to 30 dB/cm. Indeed, losses almost do not affect the device passband width.

38

Figure 3.5 reports the insertion loss, computed as the power loss between the input waveguide and the output waveguide, at the drop port of the MRR-based device as a function of the coupling coefficient with the propagation loss as a parameter. The insertion loss decreases with increasing coupling coefficients, with a steeper decrease when the power coupling coefficients are below a given threshold, between 0.2 and 0.3 depending on the propagation loss. For higher values of the power coupling coefficients the insertion loss exhibits a slower decrease. Thus, it is important to carefully adjust the value of the coupling coefficients because a small difference in coupling coefficient implies a significant change of the insertion loss. Finally, higher propagation losses imply higher values of insertion losses. Instead, for low propagation losses the insertion losses assume very low values and they are almost constant with respect to the power coupling coefficient variation.

We observed that larger flat-top passband width can be achieved if the power coupling coefficients between MRRs are increased with respect to the coupling coefficient between the waveguide and the first MRR. Thus, we modify Eq. 3.7 by adding a coefficient γ to the equation;

$$k_1^2 = k_2^2 = 0.25 \cdot \gamma \cdot k_0^4, \tag{3.8}$$

where $\gamma \geq 1$. In Fig. 3.6, it is shown that the passband of the structure increases with increasing γ. If γ is larger than 1.5, the spectral response exhibits large fluctuations at the top spectrum that makes the device unsuitable for flexible grid applications.
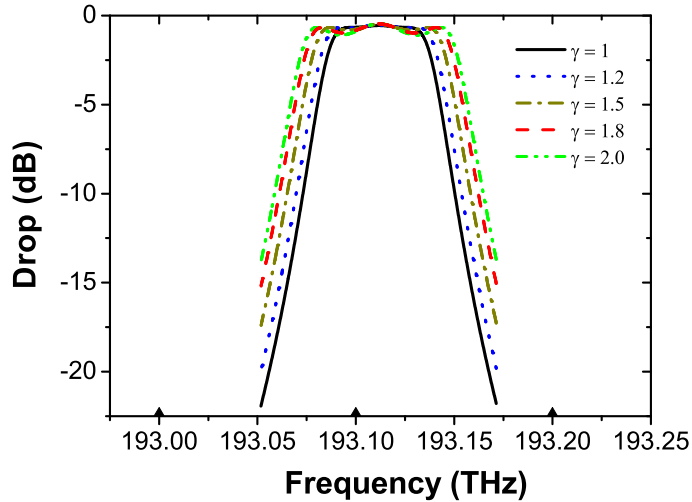
Figure 3.6. -3 dB passband width as a function of the coefficient γ, with MRR diameter $D = 20$ μm, propagation loss 5 dB/cm and power coupling coefficients $k_0^2 = 0.16$.

3.3.3 Sensitivity to the Ring Diameters of Microring Resonators

Figure 3.7 shows the coupling coefficient between the linear waveguide and the MRRs versus the MRR diameters to obtain a given passband width. In the simulation, light propagation losses in the MRRs are set to 5 dB/cm when the diameters are greater than 10 μm, whereas for the diameters of 4, 8, and 10 μm, the light propagation losses in the MRRs are set to be 40, 13.1 and 7.5 dB/cm, respectively [83]. These values are exponentially dependent on the bending radii [84, 85].

To obtain a given passband bandwidth the coupling coefficients between the linear waveguides and the MRRs must be linearly increased with the MRR diameters. The coupling coefficient increase can be achieved by decreasing the gaps between the linear waveguides and MRRs.
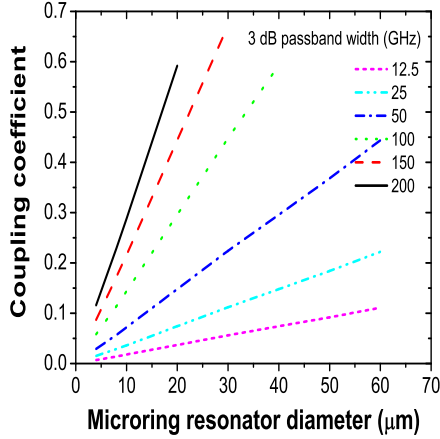
Figure 3.7. Coupling coefficient vs. the MRR diameter under a given passband width.
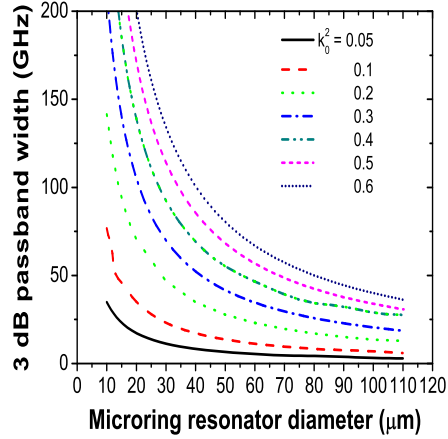
Figure 3.8. -3 dB passband width as a function of the MRR diameter under a coupling coefficient.

The passband widths are instead inversely proportional to the diameters, as shown in Fig. 3.8, which reports the passband width as the function of MRR diameters for a light propagation losses of 5 dB/cm. The passband widths roughly decrease exponentially as the MRR diameters increase. Thus, it is better to use MRRs with small diameters to obtain large flat-top passbands that can be suitable to be used in WSS based on MRRs for flexible-grid networks.

Figure 3.9 shows the insertion loss as a function of the diameters of MRRs for variable passband widths. The insertion losses decrease drastically with the increase of MRR diameters until the diameters are larger than 10 μm, while for larger diameters the insertion losses are almost constant. The reason is that the

bending losses increase drastically for MRRs with small diameters. In particular, the bending losses increase exponentially with the decrease in diameters when the MRR diameters are smaller than 10 μm. The insertion losses strongly depend on the bending losses for small MRRs while the propagation losses, including bending losses and intrinsic transmission losses through linear lengths become almost constants for larger MRRs.

For ring diameters larger than 10 μm the insertion losses are almost constant for a given passband width as the MRR diameters increase. Indeed, as previously described, coupling coefficients between MRRs must be increased for increasing diameters of MRRs to achieve fixed passband widths. The coupled light powers into the MRRs compensate the increased propagation losses when the MRR diameters are increased. As a result, the insertion losses of the MRR devices change very little.

Finally, Figure 3.10 shows the insertion loss as a function of the MRR diameters. Enlarging the MRR diameters implies not only increasing the light propagation distance in the MRRs, but also decreasing the bending loss.
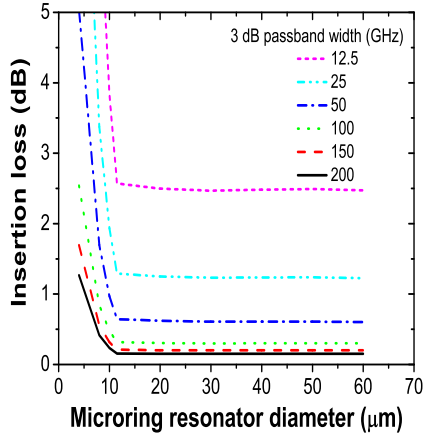
Figure 3.9. Insertion loss as a function of the MRR diameter under a -3 dB passband width.
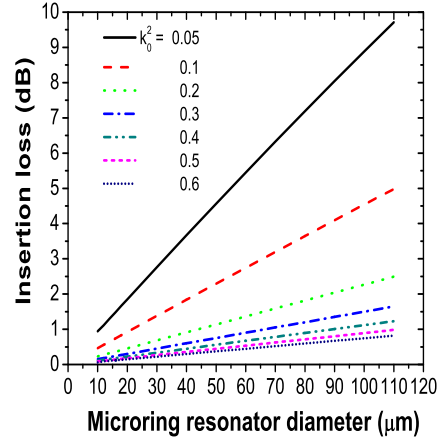
Figure 3.10. Insertion loss as a function of the MRR diameter under a coupling coefficient.

3.4 Applications of High-Order Microring Resonator Switching Devices for Wavelength Selective Switches

The analyzed MRR-based structures show the characteristics that can be of great benefit in designing WSSs for flexible-grid networks. Indeed, by varying the diameters or the power coupling coefficients it is possible to obtain flat-top bandwidths at

the output port with highly variable, spectral responses, ranging from very narrow to very large bandwidths. For instance, Figure 3.11 depicts the spectral responses with flat-top passband widths of 6.25 GHz and 3 THz bandwidths, which are respectively the minimum and the maximum passband widths that can be achieved in 3rd-order MRR-based switching devices. The narrow passband width is achieved when the MRR diameters are 20 μm, the coupling coefficient $k_0^2 = 0.02$, $k_1^2 = k_2^2 = 0.01$, and the propagation losses in the rings are 5 dB/cm. The wide passband width is instead achieved when the MRR diameters are 2 μm, coupling coefficients are $k_0^2 = 0.53$, $k_1^2 = k_2^2 = 0.2$, and propagation losses are 25 dB/cm. The insertion losses of the two elements are 4.35 dB and 0.36 dB, respectively. Thus, by properly selecting design parameters, flat-top passbands with bandwidths varying from 6.25 GHz to 3 THz using a 3rd-order MRR-based structure can be achieved. In the case that a passband wider than 3 THz is required, several MRR-based switching devices, operating at different frequencies, can be cascaded and a much wider passband can be achieved. For example, a 4 THz passband width can be achieved if we cascade two MRR-based switching devices in two continuous frequency interval having a passband width of 2 THz.

(a) -3 dB bandwidth of 6.25 GHz.

(b) -3 dB bandwidth of 3 THz.
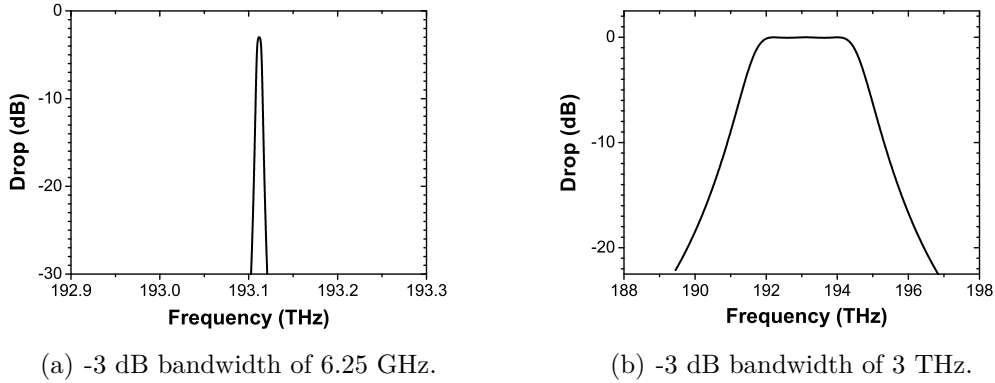
Figure 3.11.   Spectral response with -3 dB bandwidths of 6.25 GHz and 3 THz.

Obviously, it is required to cascade several of these devices to achieve more complex switching functionalities for a flexible-grid network. A possible application for flexible-grid network is depicted in Fig. 3.12 which represents a simple 4-stages optical switch able to switch 12.5, 25, 50, and 100 GHz -3 dB passband widths at the drop ports. In this case, all MRRs have the diameters of 20 μm with the propagation losses of 5 dB/cm while coupling coefficients $k_0^2 = 0.037, 0.072, 0.15, 0.285$ between bus waveguides and MRRs are used. The four groups of MRRs have different effective refractive indices equal to 3.212, 3.214, 3.216, and 3.22 respectively. Figure 3.13 shows the transmission spectra at the four drop ports and at the through port. Insertion losses are 2.5, 1.33, 0.72 to 0.47 dB, respectively.
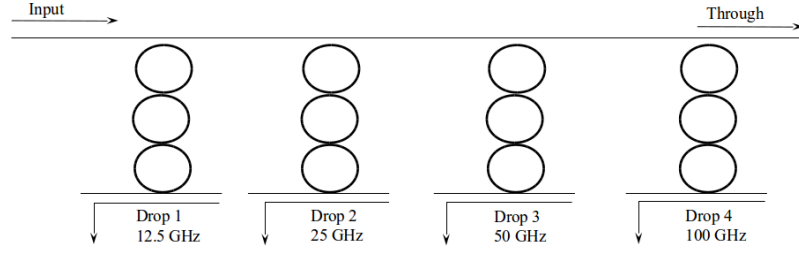
Figure 3.12.   Structure of a wavelength selective switch with four drop ports at different passband widths.

(a) Drop port

(b) Through port
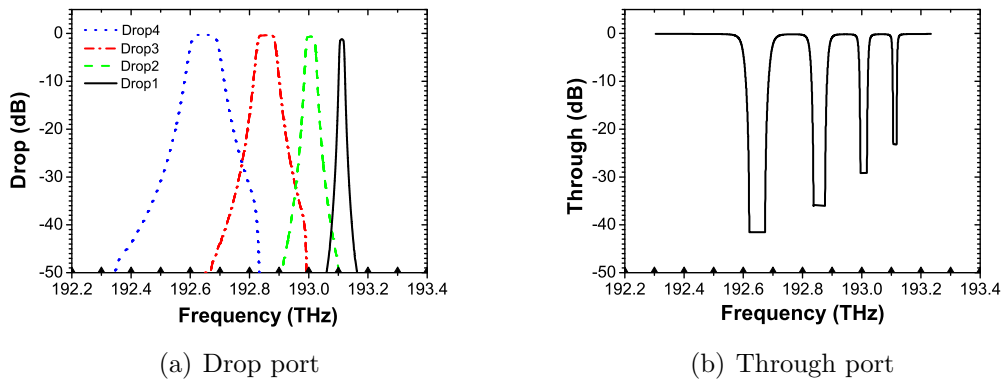
Figure 3.13.   Transmission spectral response of WSS with four drop ports.

Another switching device which can be built with a MRR-based structure is shown in Fig. 3.14. In this case MRR-based devices have the same structure and they are characterized by a -3 dB passband width of 12.5 GHz. At output ports, it is possible to select combinations of the signals at the drop ports and at the through port thanks to the use of optical switches, exploiting for example Semiconductor Optical Amplifiers (SOAs). Moreover, the third-order MRR switches can be switched on or off by tuning the refractive index of the waveguide of one of the three MRRs in a third-order MRR switch. According to the required switching functionalities, the structure of Fig. 3.14 can be modified or it can be used as a building block for the design of a flexible WSS. The MRRs require to be properly designed (i.e., selection of the MRR diameters and of power coupling coefficients) to guarantee low losses which will ensure the scalability of the WSS. Thus, further work will consist in the study of the appropriate design of MRR-based devices to build a scalable flexible WSS.

Nevertheless, MRR devices show some limitations. The resonant wavelengths of the MRRs are sensitive to the geometrical sizes of the MRRs. A very small fabrication error such as 10 nm, which reaches micro-fabrication precision limit in
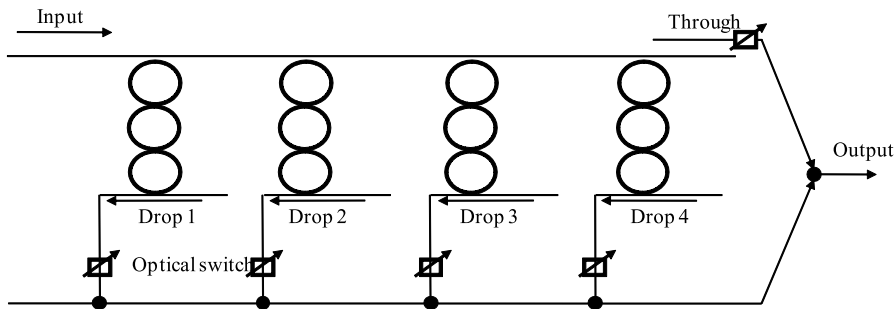
Figure 3.14.   Structure of a simple WSS with four drop ports.

modern industrial processing fields, can lead to a 0.5 nm resonant wavelength shift of a MRR. Dispersion implies resonant wavelength shift and coupling coefficient variation between MRRs, the latter leading to passband width fluctuations.

3.5   Conclusions

Wide flat-top passbands can be achieved in 3rd-order MRR-based devices consisting of three cascaded MRRs. The passband widths of the devices are mainly influenced by the MRR diameters, the coupling coefficients between the linear waveguides and MRRs, and the coupling coefficients between the MRRs.

A detailed analysis on the impact of design parameters on the spectral response and on the insertion losses of these devices has been provided. The bandwidths of the devices increase linearly with the coupling coefficients while they are inversely proportional to the ring diameters. Flat-top passband widths varying from 6.25 GHz to 3 THz can be achieved using 3 cascaded MRRs by properly selecting the MRR diameters and the coupling coefficients between the bus waveguides and the MRRs and between MRRs, while keeping their insertion losses acceptable.

We showed possible structures of optical switches with limited switching capabilities. Future works will investigate how scalable and full-capable switches can be built using MRR-based devices. Indeed, although in the early development stage, MRR-based switching devices seem a promising alternative to free space optics or liquid crystal switching systems which are today proposed to build WSSs in the flexible-grid scenario.

Chapter 4

Spectral Shaping of Passbands of Microring Resonator Switches

Spectral shaping of the passbands of microring resonator switches is studied in this chapter. Multistage high-order microring resonator-based optical switch structures are proposed to achieve steep-edge flat-top spectral passband. Using the transfer matrix analysis model, the spectral response behaviors of the switch architectures are simulated. The results show that multistage high-order microring resonator-based switches can achieve steep edge flat-top spectral passbands with rectangular shapes which can meet the spectral passband requirements of flexible grid optical networks.

4.1 Introduction

Flat-top spectral passbands with steep edges are required for filters, switches, and other photonic devices in optical communication networks and on-chip interconnects to reduce crosstalk and to achieve uniform transmission intensity distribution through the communication systems. To support the grids, channel spacings, and frequency slots of flexible grid networks, ultra-narrow passband filters/switches are needed. Microring resonators have high wavelength selective characteristics and narrow flat top passbands with steep edges may be achieved in MRR devices as introduced in Chapter 3 by accurately controlling the ring diameters, coupling coefficients between rings and waveguides, as well as the number of microrings.

A 90-cascaded-MRR structure as shown in Fig. 4.1(a) was reported and fabricated to achieve sharp peak transmission response and long group delays [86]. In the structure, the drop waveguide of the first microring resonator is the input waveguide of the second ring, the drop waveguide of the second microring resonator is the input waveguide of the third ring, and so forth. With such an arrangement, each ring

resonator in the cascades filters the input light and relays the filtered light to the next cascaded microring. As a result, the ring resonator structure has very sharp transmission peaks at the drop ports but high loss. If a single ring resonator in a relay stage is replaced with two or more rings, as shown in Fig. 4.1(b), flattened top passpand can be achieved by optimizing the coupling coefficients between the MRRs while the insertion loss can be reduced a lot. The structure in Fig. 4.1(b) is called multistage N^{th}-order MRR devices, where the "order" refers to the number of rings in one stage as introduced in Chapter 3. In Fig. 4.1(a), there is only one ring in a stage, thus the structure is named multistage first-order MRR device although there are many MRRs in the final layout. In the multi-stage structure, the signal dropped at the first stage is propagated into the input waveguide of the second stage, the signal dropped at the second stage is propagated into the input waveguide of the third stage, and so on. This permits to obtain a very steep edge flat-top wide passpand but with a low insertion loss.

(a)

(b)
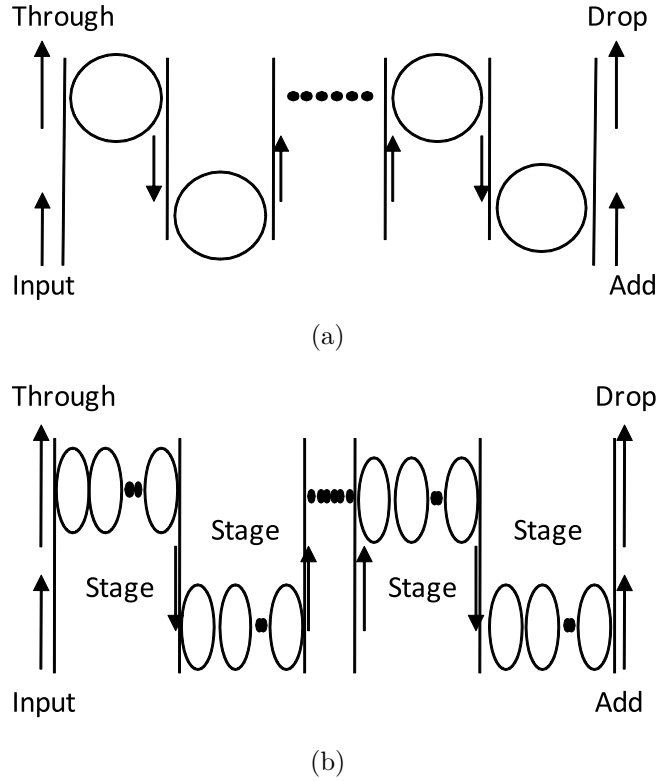
Figure 4.1. (a) Layout of a MRR structure for sharp transmission peak. (b) Multistage N^{th}-order MRR structure for steep-edge flat-top passband.

In this chapter, we use the transfer matrix model to simulate light transmission through multi-stage N^{th}-order MRR-based switches and cascaded N^{th}-order

MRR-based switches without relay stages. We first compare numerical simulation with experimental measurement to confirm the validity of the model. The spectral response behaviors of the multi-stage N^{th}-order MRR switches are discussed and compared with those of simply cascaded MRR structures without stages. The results show that the multi-stage N^{th}-order MRR structure provides superior passband characteristics to the Nth-order MRR structure without stages at the same number of MRRs.

4.2 Improved Algorithm of Transfer Matrix Equations for Cascaded Microring Resonator Devices

As pointed out in [87], the computation results in Eq. 3.1 may be inaccurate or unphysical for large number of MRRs N (typically > 20), due to numerical overflow in matrix elements for large N, which is caused by large value $\frac{1}{k_n}$ in the case of weak coupling coefficient k_n between neighbour MRRs. The problem was encountered in our simulation even when $N > 10$. To solve this problem, we apply the same method as in [87] as follows:

We reformulate Eq. 3.1 as

$$\begin{bmatrix} a_n \\ b_n \end{bmatrix} = Q_n^{-1} P_n^{-1} \begin{bmatrix} a_{n+1} \\ b_{n+1} \end{bmatrix} \tag{4.1}$$

$$\begin{bmatrix} a_0 \\ b_0 \end{bmatrix} = P_0^{-1} \prod_{n=1}^{N} (Q_n^{-1} P_n^{-1}) \begin{bmatrix} a_{N+1} \\ b_{N+1} \end{bmatrix}$$
$$= \begin{bmatrix} A' & B' \\ C' & D' \end{bmatrix} \begin{bmatrix} a_{N+1} \\ b_{N+1} \end{bmatrix} \tag{4.2}$$

where P_n^{-1} and Q_n^{-1} are the inverses of P_n and Q_n. $Q_n^{-1} = Q_n$.

$$b_0 = (C' - \frac{A'D'}{B'})a_{N+1} + \frac{D'}{B'}a_0 \tag{4.3}$$

$$b_{N+1} = -\frac{A'}{B'}a_{N+1} + \frac{a_0}{B'} \tag{4.4}$$

For single input, i.e. $a_{N+1} = 0$, we obtain the transmissions b_0 and b_{N+1} at both the through and the drop ports in Fig. 3.1 as follows:

$$b_0 = \frac{D'}{B'}a_0 \tag{4.5}$$

$$b_{N+1} = \frac{1}{B'} a_0 \tag{4.6}$$

Since all the elements P_n^{-1} are proportional to the weak coupling coefficient k_n, the calculated matrix elements in Eq. 4.2 are limited to small values and no exponential divergence or numerical overflow occurs, so that the calculations following Eq. 4.1-Eq. 4.6 become accurate and convergent.

To confirm the validity of the equations above, the simulated results are compared with experimental measurement [46], as shown in Fig.4.2. In the simulation, all the parameters of the device are the same as those in [46]. The device consists of three MRRs with the radii of 10 μm. The effective index of refraction of the waveguides for the MRRs are 3.8. The light propagation loss is 3 dB/cm. The power coupling coefficient of k_0^2, k_1^2, k_2^2, and k_3^2 are 0.164, 0.0049, 0.0049, and 0.164, respectively. The thin curves represent simulated results, while wide solid curves are the measured ones. Simulated results are in very good agreement with the experimental measurements. We also used the above equations to simulate the drop responses of the MRR-based devices and compared our results with the corresponding experimental measurements in [88,89]. Also in this case the numerical simulated results are in good agreement with the experimental measurements. Thus, we will use the transfer matrix theory to predict the light transmission behaviors of the MRR devices in the following sections.
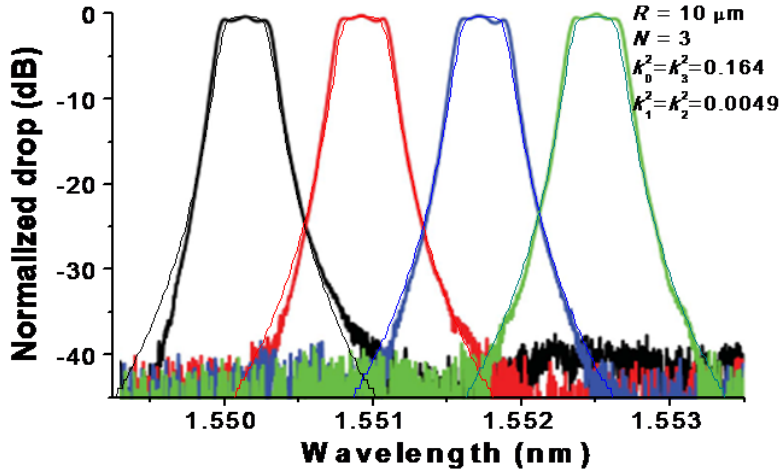
Figure 4.2.   Comparison of numerical simulation with experiment measurement: Wide solid curves represent experimental measurements; Thin curves represent simulated results.

4.3 Multi-Stage Microring-Resonator-Based Switch Elements

Using the transfer matrix equations from Eq. 4.1 to Eq. 4.6 we simulate the optical output behaviors of multistage MRR-based switches as follows. In the simulation, we assume that all MRRs have the same geometric parameters, including ring resonator diameter, waveguide width, and waveguide thickness. We set that the coupling coefficient k_0 between the input linear waveguide and the first MRR is equal to the coupling coefficient k_N between the output linear waveguide and the last MRR, and that the coupling coefficients k_1, k_2, ..., k_{N-1} between two adjacent MRRs in stages have the same values. Figure 4.3 shows the response spectra at drop ports for multistage third-order MRR-based switches, i.e., three MRRs are used in each stage. In the three figures, the geometrical radii of all the third-order MRRs are 10 μm. However, their passband widths are different. From Fig. 4.3(a) to Fig. 4.3(c), the passband width increases and their coupling coefficients between bus linear waveguides and MRRs, and the coupling coefficients between MRRs increase. The power coupling coefficients between two adjacent microrings are 0.0008, 0.003, 0.013, and the coupling coefficients between the linear waveguides and the microrings are 0.068, 0.135, 0.27, respectively. In these parameters, we can obtain -3 dB passband widths of 0.1, 0.2, and 0.4 nm, corresponding to the bandwidths of 12.5, 25, and 50 GHz in frequency for the switches, respectively. These passband widths correspond to a part of the widths of standard frequency slots in flexible grids recommended by ITU-T. The effective indices of refraction of the waveguides of the MRRs are set to 3.8 [46]. The light propagation losses through the MRRs are 5 dB/cm [83]. Since the light propagation loss through a MRR is sensitive to light polarization direction and TE polarization light has lower propagation loss in the waveguide with rectangular cross section used in this work, only TE polarization light propagation is considered in our simulation.

As can be seen from Fig. 4.3, the passband width of the switch is different for different coupling coefficient between MRRs and different coupling coefficient between input/output waveguide and MRR. Furthermore, the passband roll-off edge of the switch becomes steeper and the passband becomes narrower when the stage number increases from 1 to 6. This indicates that increasing the number of microring in each stage improves the spectral passband shape at the drop port of the switch. The roll-off edge of light output spectral response becomes steeper and steeper as the stage number increases, while the response spectrum at drop port keep flat-top shape. The -3 dB bandwidths decrease from 0.13 to 0.08 nm in Fig. 4.3(a), from 0.27 to 0.18 nm in Fig. 4.3(b), and from 0.52 to 0.36 nm in Fig. 4.3(c) when the stage numbers increase from 1 to 6. Furthermore, rectangular transmission responses are achieved when the stage number increases. However, the insertion

49

losses of the switches also increase when more stages are used. The insertion losses of the switches increase from 1.56 to 9.49 dB in Fig. 4.3(a), from 0.78 to 4.79 dB in Fig. 4.3(b), and from 0.39 to 2.45 dB in Fig. 4.3(c) when the stage numbers increase from 1 to 6. Comparing the output powers corresponding to the flat-top parts of the curves, the devices show higher output powers when they have larger passband widths. This indicates that the devices show lower insertion losses when they have larger passband widths.
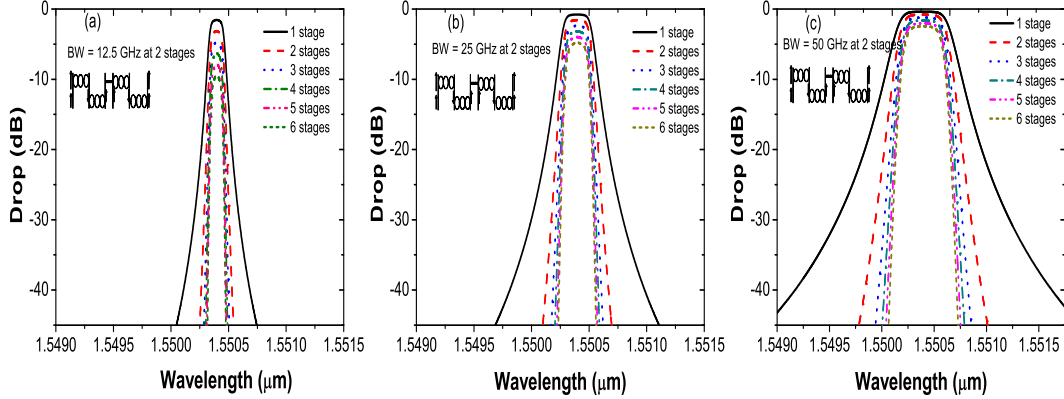
Figure 4.3. Response spectra at drop port of multistage third-order MRR-based switches.

Now we compare the response spectra of multistage N^{th}-order MRR switches with the response of Nth-order MRR switches which have the same MRR numbers but without stages. Fig. 4.4(a) reports the response spectra of multistage third-order MRR switches. In the switches, there are three MRRs in a stage. The geometrical radii of the third-order MRRs are 10 μm, the power coupling coefficients between the microrings are 0.0049 and the coupling coefficients between the linear waveguides and the microrings are 0.16. The effective index of refraction of the waveguides of the MRRs is 3.8. The light propagation losses through the MRRs are 5 dB/cm. Fig. 4.4(b) reports the response spectra of Nth-order MRR switches without stages. All the geometrical radii of the MRRs, index of refraction, light propagation losses through the MRRs, the coupling coefficients between the microrings, and the coupling coefficients between the linear waveguides and the microrings are the same as those in Fig. 4.4(a). As can be seen in Fig. 4.4, the response spectra of multistage resonator switches are different from those of Nth-order MRR switches without stages although they have the same numbers of MRRs. In Fig. 4.4(a), all the curves show clear, regular, and smooth shapes for the multistage N^{th}-order MRR switches when the stage number increases from 2 to 6. However, in Fig. 4.4(b), all the curves show irregular and fluctuating shapes for the Nth-order MRR switches without stages when the microring number increases from 6 to 18. Comparing those

50

curves in Fig. 4.4(a) with Fig. 4.4(b), we can see that the roll-off edge of response spectrum becomes steeper and steeper as the stage number increases for multi-stage third-order MRR switches while the response spectrum keeps flat-top shape. However, for a MRR switch without stages, the shape of the response spectrum at drop port changes a lot when the MRR number increases. Fluctuation is seen in the top passband of the response spectrum. We also compare the response spectra of multi-stage N^{th}-order MRR switches, which have 2, 4 - 10 MRRs in a stage, with the response spectra of simple N^{th}-order MRR switches without stages when both switches have the same MRR numbers. The response spectra of the multi-stage N^{th}-order MRR switches show the same behaviors. This indicates that the multi-stage N^{th}-order MRR-based devices in Fig. 4.1(b) have better performance in passband property than N^{th}-order MRR-based devices without stages in Fig. 3.1.
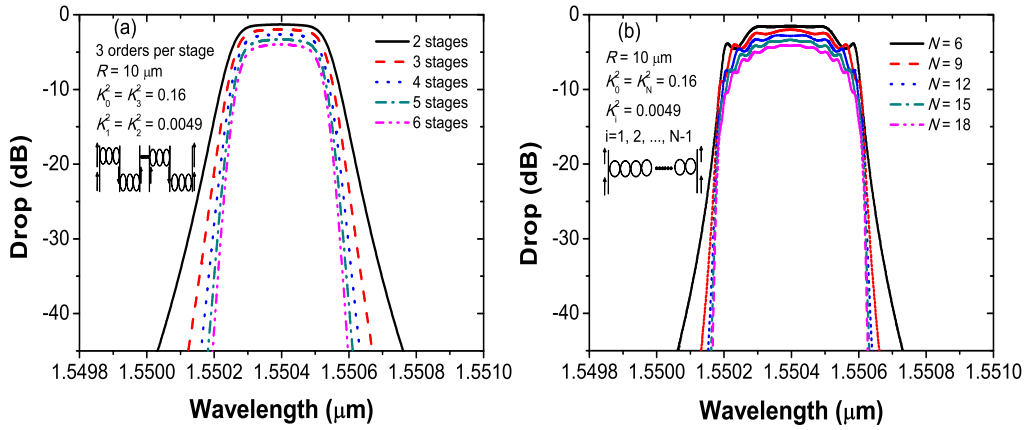
Figure 4.4. (a) Response spectra at the drop port of multi-stage third-order MRR-based switches. (b) Response spectra at the drop port of Nth-order MRR-based switches without stages.

We note that the insertion loss of the multistage N^{th}-order switch increases with the number of stage since the signal intensity from its drop port decrease when the number of stage increase as shown in Fig. 4.4. This implies that there is a trade-off between insertion loss and passband width to achieve an optimal stage and microring numbers for switch design which deserves further investigation.

4.4 Conclusions

The transmission behaviors of multistage N^{th}-order MRR-based switches were simulated by using an improved algorithm for the transfer matrix theory. The results showed that steep-edge flat-top spectral responses at the drop ports of multistage

51

MRR-based switches were achieved. Increasing stage number can obtain steeper-edge response spectra of the multistage MRR-based switches, however it also increases the transmission losses of the switches. The simulation showed that the multistage N^{th}-order MRR-based switches provided better passband properties than the cascaded MRR-based switches without stages. Clear, regular, smooth, steep roll-off edge flat-top passpands were achieved in the multistage N^{th}-order MRR-based switches. Irregular and fluctuating passpands were shown in the Nth-order MRR-based switches without stages. Thus, in order to achieve steep-edge flat-top passpands of MRR switches or filters, it is better to use the multistage N^{th}-order structure with optimal design instead of the simple N^{th}-order structure without stages. Note that there is a trade-off between the insertion losses and the passband widths to achieve an optimal performance in a switch design. We also note that the tunability of the switch passbands is important for the MRR switch design. They can be achieved by changing the refractive indices of the waveguides using thermal-optic tuning, electric-optic tuning technology, and others. They will be investigated elsewhere.

Chapter 5

Bandwidth-Variable Microring-Resonator-Based Wavelength Selective Switches

Two types of microring-resonator-based wavelength selective switch architectures are proposed in this chapter to realize variable output bandwidths varying from 0 to 4 THz. One consists of 320, 160, and 80 third-order MRR switches with -3 dB passband widths of 12.5, 25, and 50 GHz, respectively. Another one consists of two-stage switch structures. The first stage is a 1×4 MRR-based wavelength selective switch with the passband width of 1 THz per output port. The second stage makes up of four passband-variable MRR switch blocks with the widths ranging from 0 to 1 THz. Each block makes up of 80, 40, 20 third-order MRR switches with the passband widths of 12.5, 25, and 50 GHz, respectively. Their insertion losses and crosstalks in the worst cases are numerically analysed and compared, showing acceptable insertion losses and tolerable crosstalks for practical MRR switching applications in flexible optical networks.

5.1   Introduction

Due to continuous increase of traffic load in telecommunication networks, rigid fixed-grid wavelength division multiplexing optical networks can no longer keep up with the emerging bandwidth-hungry and highly dynamic services in an efficient manner. The research community has focused on seeking more advanced optical transmission and networking solutions that utilize the available bandwidth more effectively. The flexible optical networking paradigm has emerged as a way to offer efficient use of the limited resources [1]. In the flexible optical networking, the network dynamically adjust its resources, not only the optical bandwidths but also the modulation formats

according to the requirements of each connection. For the flexible networks, very important components are flexible optical switches.

Flexible optical switches should have variable bandwidth characteristics (i.e., tunable optical bandwidth and center frequency per channel) at a fine granularity. The key to provide such variable bandwidth characteristics lies in wavelength selective switches, which sit at the heart of the optical switch [3]. The very first proposal for a variable passband/flexigrid WSS was reported in [4]. It is possible to construct advanced WSSs using liquid crystal- on-silicon technologies [5] or microelectromechanical system [6]. But they need large space to realize wavelength selection function and they can not be used in chip-level optical networks and optical interconnections. AWG-based WSSs [90] are available in the market, but their fabrication is relatively complicated compared with the fabrication of MRRs reported.

Mircroring resonators as wavelength selective components have attracted wide attentions for applications in optical interconnections and optical networks, due to their evident advantages in wavelength high selectivity, compact foot printing, fast switching, and low power consumption. Experiments have shown the potential for MRRs to be used as high performance modulators, filters, routers, switches, add/drop multiplexers in optical interconnections and optical networks as introduced in Chapter 1. In particular, the resonant wavelengths of the MRRs can be tuned using thermo-optic effect, electro-optic effect or other techniques as introduced in Chapter 2. This makes the passband widths of MRR devices be adjusted quite agile. Thus the variable passband widths become achievable in the MRR devices.

Based on the available spectrum in the C band, we design our MRR switch architectures with the variable bandwidths in the range from 0 to 4 THz in this chapter. Two types of microring-resonator-based switch architectures are designed to realize variable output bandwidths. One consists of 320, 160, and 80 third-order MRR switches with -3 dB passband widths of 12.5, 25, and 50 GHz, respectively. Another one is a two-stage switch architecture consisting of a 1 × 4 MRR-based wavelength selective switch with the passband width of 1 THz per output port as the first stage, and four switch blocks as the the second stage with each block composed of 80 third-order MRR switches with passband widths of 12.5 GHz, or 40 third-order MRR switches with passband widths of 25 GHz, or 20 third-order MRR switches with passband widths of 50 GHz. Their insertion losses and crosstalks in the worst cases are numerically analysed and compared.

5.2   Switch Architectures and Insertion Loss

We give the details on the design of the bandwidth-variable architectures. We also discuss the maximal insertion losses of the architectures for their practical applications in optical networks and optical connections.

5.2.1 High-Order Microring Resonator Switch Architecture

Figure 5.1 shows a switch architecture to achieve variable pass bandwidths by selecting combinations of the signals at the drop ports and at the through port. The architecture consists of a lot of third-order MRR switches with different passband widths. We report the switch architectures with variable passband widths of 1 and 4 THz as follows.
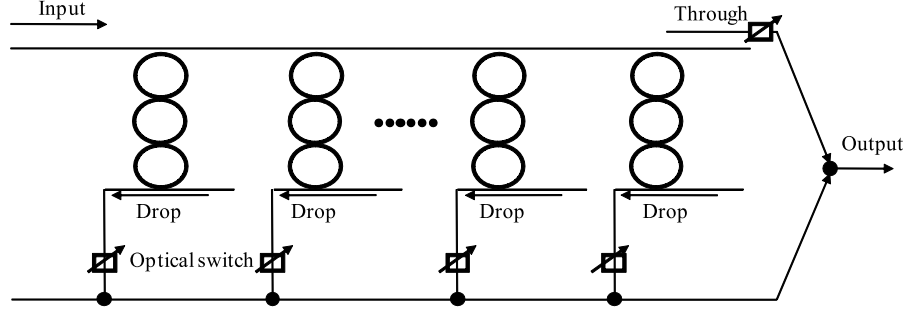
Figure 5.1. Architecture consisting of MRR switches with variable pass bandwidths.

Variable Passband Widths of 1 THz

The first architecture consists of 80 third-order MRR switches with the bandwidths of 12.5 GHz, the light coupling coefficients between the linear bus waveguide and the MRRs, and between the linear waveguides at drop ports and the MRRs of the third-order switches are $k_0^2 = k_3^2 = 0.0464$. The light coupling coefficients between two MRRs in the third-order switches are $k_1^2 = k_2^2 = 0.0116$. The second architecture consists of 40 third-order MRR switches with the bandwidth of 25 GHz, the light coupling coefficients are $k_0^2 = k_3^2 = 0.0939$, $k_1^2 = k_2^2 = 0.0022$. The third architecture consists of 20 third-order MRR switches with the bandwidth of 50 GHz, the light coupling coefficients are $k_0^2 = k_3^2 = 0.1878$, $k_1^2 = k_2^2 = 0.0469$. All the third-order MRR-based switches in the three architectures are divided into four groups. The MRRs in each group have same radii. The radii of the MRRs in the four groups of MRR switches are designed to be 12.617, 12.708, 12.8, and 12.891 μm, respectively.

In detail, for the architecture consisting of 80 third-order MRR switches, the MRR switches are divided into four groups and each group has 20 third-order MRR switches. The first group consists of 20 third-order MRR switches with the radii of 12.617 μm. The second group consists of 20 third-order MRR switches with the radii of 12.708 μm. The third group consists of 20 third-order MRR switches with the radii of 12.8 μm. The fourth group consists of 20 third-order MRR switches with the radii of 12.891 μm. For the architecture consisting of 40 third-order MRR switches,

the MRR switches are divided into 4 groups and each group has 10 third-order MRR switches. The first group consists of 10 third-order MRR switches with the radii of 12.617 μm. The second group consists of 10 third-order MRR switches with the radii of 12.708 μm. The third group consists of 10 third-order MRR switches with the radii of 12.8 μm. The fourth group consists of 10 third-order MRR switches with the radii of 12.891 μm. For the architecture consisting of 20 third-order MRR switches, the MRR switches are divided into 4 groups and each group has 5 third-order MRR switches. The first group consists of 5 third-order MRR switches with the radii of 12.617 μm. The second group consists of 5 third-order MRR switches with the radii of 12.708 μm. The third group consists of 5 third-order MRR switches with the radii of 12.8 μm. The fourth group consists of 5 third-order MRR switches with the radii of 12.891 μm. Such radius selection is based on a trade-off between design accuracy and fabrication precision.

In principle, all the third-order MRR-based switches should have different radii for different central frequencies according to the resonant equation of MRRs introduced in Chapter 2, i.e. $2\pi R n_{eff} = m\lambda_i$. In this case, the difference of MRR radii between two adjacent third-order MRR-based switches is less than 0.005 μm. Such a small radius difference is beyond the precision limitation in current semiconductor fabrication technologies. To avoid this problem, each group of MRR switches are set to have the same radii since such design makes the fabrication feasible. We assume the effective refractive indices of the linear waveguides and the waveguides of the first MRR switches in the three architectures to be 3.296 at the wavelength of 1.55 μm. The refractive index differences of the waveguides in two adjoining third-order switches are approximate 2.15×10^{-4}, 4.3×10^{-4}, and 8.6×10^{-4} for the three architectures respectively so that all the switches in the architectures can output light signals with different wavelengths but with same passband widths. The different waveguide refractive indices can be achieved using thermo-optic or electro-optic effect as we introduced in Chapter 2. The geometrical spacing between the two third-order MRR switches is 50 μm. In the architectures, the variable bandwidths ranging from 0 to 1 THz can be achieved by switching on or off a part of switches so as to achieve variable pass bandwidths.

Variable Passband Widths of 4 THz

For variable bandwidths varying from 0 to 4 THz, we select small MRRs with the radii of 3.03 μm since small MRRs have large free spectral range which can avoid signal interference between channels. We set same radii for all the MRRs, because the resonant wavelengths of small MRRs are very sensitive to the variation of the diameters of the MRRs leading to very high precision requirement in device fabrication. Using same radii for all the MRRs can avoid the high precision requirement in device fabrication. Instead, we assume that the refractive indices of MRRs are

tunable and that the refractive indices of MRRs match the variation of the resonant wavelengths of each MRR switch. The first architecture consists of 320 third-order MRR switches with the bandwidths of 12.5 GHz, the light coupling coefficients between the linear bus waveguide and the MRRs, and between the linear waveguides at drop ports and the MRRs of the third-order switches are $k_0^2 = k_3^2 = 0.0105$. The light coupling coefficients between two MRRs in the third-order switches are $k_1^2 = k_2^2 = 0.0026$. The second architecture consists of 160 third-order MRR switches with the bandwidth of 25 GHz, the light coupling coefficients are $k_0^2 = k_3^2 = 0.021$, $k_1^2 = k_2^2 = 0.0053$. The third architecture consists of 80 third-order MRR switches with the bandwidth of 50 GHz, the light coupling coefficients are $k_0^2 = k_3^2 = 0.042$, $k_1^2 = k_2^2 = 0.0105$. The geometrical spacing between two neighbor third-order MRR switches is 20 μm. The waveguides have the cross sections of 450 nm wide by 220 nm height, and their inherit effective refractive index is 3.296.

Figure 5.2 reports typical transmission spectra of the MRR switch architecture in Fig. 5.1 that can be achieved by selectively switching on/off a part of third-order MRR switches. Figure 5.2(a) shows the pass bands with the widths of 12.5, 25, 50, 100, 150 and 200 GHz which are obtained from the through port of the switch architecture. Figure 5.2(b) reports the transmission response spectra at the drop port corresponding to the pass band spectra in Fig. 5.2(a). The operation spectra are obtained when the through port outputs the signals and when all the drop signals are extracted from all other ports and propagate into the bus linear waveguide and are output from one port instead of the through port. Actually, various bandwidths can be achieved. For example, in the architecture consisting of 160 third-order MRR switches with the pass band of 25 GHz, the 25 GHz band at a central frequency can be achieved directly from the drop port of one of the switched-on third-order MRR switches. It can also be obtained from the through port by switching on 159 MRR switches of which the central frequency spacings are tuned to be equal to their band widths, and the central frequency spacing between the last one and the last second one is tuned to equal half of their bandwidths, so that these unwanted signals are discarded from their drop ports. The 50 GHz band can be obtained by combining the output from the drop ports of two of the third-order MRR switches. They can also be achieved from the through port by switching on the 158 switches and discarding the unwanted signals. Furthermore, more switches can be added and be switched on to reduce the residual noise from the dropping switches, so as to reduce the inter-channel signal crosstalk. In addition, comparing Fig. 5.2(a) with Fig. 5.2(b) we can see that lower insertion losses and more uniform signal intensity distribution can be achieved when they get out from the through port of the switch than they get out from the drop ports.

Figure 5.3 reports the maximal insertion losses of the MRR switch architectures in Fig. 5.1 as the functions of propagation losses of MRRs when their variable passband widths are 1 and 4 THz. The maximal insertion loss is defined as follows.
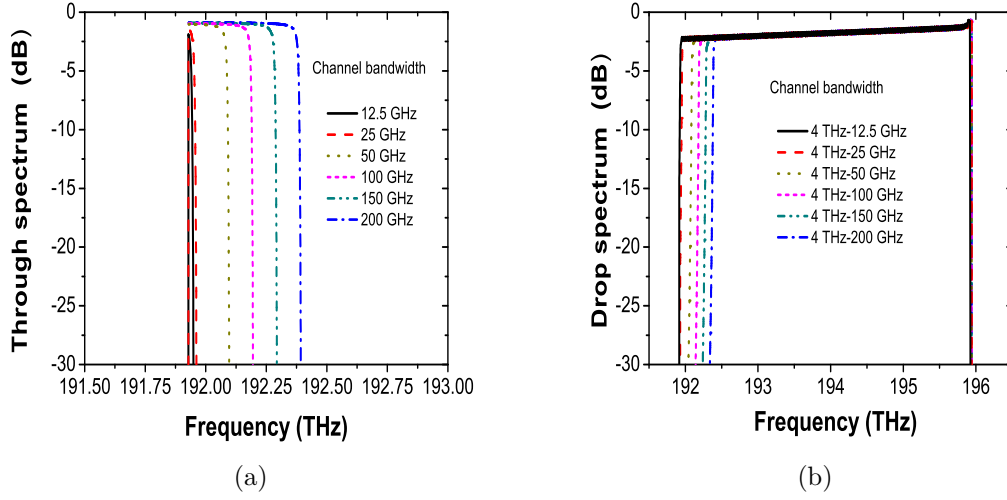
Figure 5.2. Typical transmission spectra at the through port (a) and the drop port (b) of the microring resonator switch architecture. 5 dB/cm propagation loss in rings, 3 dB/cm propagation loss in linear waveguides. 3 μm radius of rings, 20 μm spacing between neighbor rings.

When all the MRR switches in the architectures drop their light signals from their output ports, and when all the losses caused by dropping the signals from all the MRR switches and the loss in linear waveguide are taken into account, the last MRR switch at the end of the linear bus waveguide has the lowest dropped light power, corresponding to the maximal insertion loss. For other cases, for instance, when only one switch with shorter light propagation distance in linear bus waveguide drops its light signal, or when two MRR switches and more than three switches drop their light signals, the dropped light powers are higher than the lowest one. Thus, the defined maximal insertion loss corresponds to the worst case in light switch for all the architectures.

Figure 5.3(a) shows the maximal insertion losses of the switch architectures consisting of 80 drop channels with the passband width of 12.5 GHz, 40 drop channels with the passband width of 25 GHz, and 20 drop channels with the passband width of 50 GHz when the propagation losses in the linear bus waveguide are 2, 3, and 5 dB/cm and when the propagation losses in the microring resonators vary from 3 to 30 dB/cm. For a linear silicon waveguide, the realistic value of its propagation loss is reported to be around 3 dB/cm. Low loss less than 1 dB/cm in linear waveguide was also reported [83]. However, the losses in microring resonators are much higher than the values in linear waveguides. 3 - 4 dB/cm loss is regarded as low loss while 5 dB/cm or more could be the realistic values of the propagation losses in silicon MRRs. It reported ultra low propagation loss of 2 - 3 dB/cm in MRRs [83]. For

58
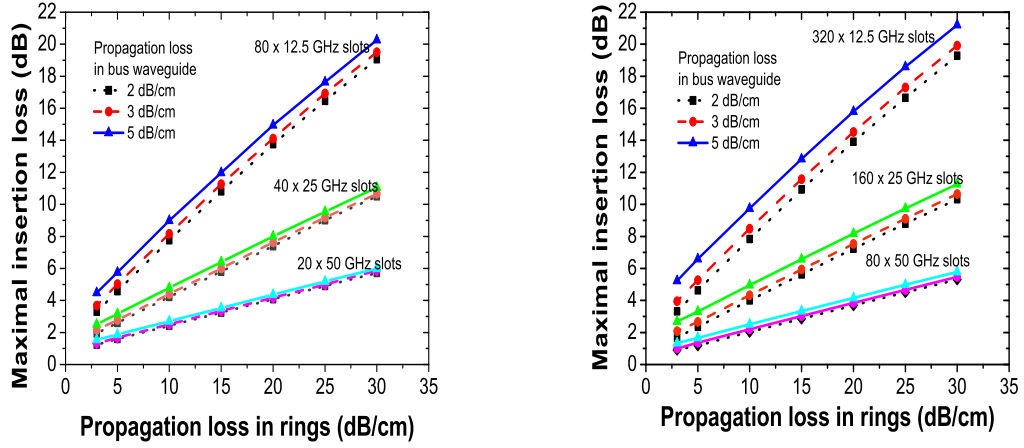
(a) 80 × 12.5 GHz, 40 × 25 GHz, and 20 × 50 GHz slots. 12.8 μm radius of rings, 50 μm spacing between neighbor rings. 1 THz total bandwidth.

(b) 320 × 12.5 GHz, 160 × 25 GHz, and 80 × 50 GHz slots. 3 μm radius of rings, 20 μm spacing between neighbor rings. 4 THz total bandwidth.

Figure 5.3.   Maximal insertion loss as a function of propagation loss in rings when the propagation losses in bus waveguide are 2, 3 and 5 dB/cm respectively.

comparison, 3 - 5 dB/cm propagation losses in the linear silicon waveguide and 3 - 30 dB/cm propagation losses in the ring silicon waveguide are used in the figures. As can been seen, the maximal insertion losses increase linearly with the propagation losses in the microring resonators while they increase with the propagation losses in bus waveguide. In particular, the switch architecture with 80 × 12.5 GHz drop channels has higher maximal insertion loss than the architecture with 40 × 25 GHz drop channels, and the switch architecture with 40 × 25 GHz drop channels has higher maximal insertion loss than the one with 20 × 50 GHz drop channels.

Figure 5.3(b) shows the maximal insertion losses of the switch architectures consisting of 320 drop channels with the passband width of 12.5 GHz, 160 drop channels with the passband width of 25 GHz, and 80 drop channels with the passband width of 50 GHz when the propagation losses in the bus waveguide are 2, 3, and 5 dB/cm and when the propagation losses in the microring resonators vary from 3 to 30 dB/cm. As can been seen, the maximal insertion losses show the same behavior as that in Fig. 5.3(a). They increase linearly with the propagation losses in microring resonators while they increase with the propagation losses in bus waveguide. The switch architecture with 320 × 12.5 GHz drop channels has higher maximal insertion loss than the architecture with 160 × 25 GHz drop channels, and the switch architecture with 160 × 25 GHz drop channels has higher maximal insertion loss than the one with 80 × 50 GHz drop channels.

59

Thus, both Figure 5.3(a) and Figure 5.3(b) show that the architecture using the MRR switches with the bandwidths of 50 GHz has the lowest maximal insertion loss while the architecture using the MRR switches with the bandwidths of 12.5 GHz has the maximal maximal insertion loss. This indicates that the architecture using the MRR switches with wider bandwidths has lower insertion loss than the one using the MRR switches with narrower bandwidths in order to achieve the drop channel combinations with same variable passband widths. The reason is that the weaker coupling coefficients between the MRRs, between bus waveguide and MRRs are used in the switch architecture consisting of the narrower passband MRR switches, resulting in lower dropped powers.

Moreover, it can be seen from Fig. 5.3(a) or Fig. 5.3(b) that, in some cases, the maximal insertion losses are less than 4 dB/cm either for the architectures consisting of 80 × 12.5 GHz, 40 × 25 GHz, 20 × 50 GHz, or for the switch architectures consisting of 320 × 12.5 GHz, 160 × 25 GHz, 80 × 50 GHz. This implies that when the architectures are properly designed and the parameters are properly selected, the insertion losses of the architectures may be decreased to acceptable values for practical optical networks.

5.2.2 Two-Stage High-Order Microring Resonator Switch Architecture

Usually, if the wavelength bands for all the signal channels cover a very wide spectral range such as C band, the wavelength bands are better to be divided into several sections for optical switching architectures so that the light signals can be separated and output in several sections. In this case, multi-stage switch architectures must be used to realize the spectral separation. The reason is that the free spectral range of the MRRs in a transmission system must be greater than the covered spectral range of C band (about 4.5 THz) in order to avoid several channels to go through a same MRR switch, i.e., to avoid crosstalk between channels. FSR is inversely proportional to the diameter of the MRRs. For 4.5 THz FSR, the diameters of the MRRs are about 3 μm. For so small MRRs, very weak couplings between the MRRs in the MRR switches must be used to guarantee a narrow passband width of 12.5 GHz. As a result, the passband shapes of the MRR switches may be deformed seriously. When the C band is divided into several sections, the MRRs with small FSRs can be used for each section. Thus large MRRs can be used. In this case, it can effectively avoid crosstalk between signal channels which are distributed in different spectral ranges. However, it is possible to incur high insertion losses and extremely nonuniform signal intensity distribution in the architectures, caused by the nonuniform signal intensity output from the switches in the first stages of the architectures.

Figure 5.4 shows a two-stage MRR switch architecture. The first stage is a 1 × 4 MRR-based wavelength selective switch with the passband width of 1 THz per output port. In the 1 × 4 MRR-based WSS, the signals are dropped from three third-order MRR switches or output directly from the linear bus waveguide. The three third-order MRR switches of the 1 × 4 WSS use different MRRs with the radii of 2.667, 2.755, and 2.844 μm independently, and their corresponding FSRs are greater than 42 nm (> 5 THz). The coupling coefficients for the the MRR switches are $k_0^2 = k_3^2 = 0.65$ and $k_1^2 = k_2^2 = 0.165$. The geometrical spacings between two switches are 50 μm. In the second stage, there are four switch blocks, corresponding to 4 variable passband MRR switches which have the same architectures as those shown in Fig. 5.1 with the passband widths ranging from 0 to 1 THz. Each block may consist of 80, 40 or 20 third-order MRR switches with same diameters. The diameters of the MRRs in the first, second, third, and fourth block are 27.928, 28.074, 28.22, and 28.366 μm, respectively. When each block in the second stage consists of 80 third-order MRR switches, the coupling coefficients for the the MRR switches are $k_0^2 = k_3^2 = 0.053$, and $k_1^2 = k_2^2 = 0.013$. In this design, the passband width of each third order MRR switch is 12.5 GHz. The intrinsic indices of refraction of the waveguides of the MRRs are 3.926 while they are assumed to be tunable for the different MRR switches. When each block consists of 40 third-order MRR switches, the coupling coefficients for the the MRR switches are $k_0^2 = k_3^2 = 0.0106$, and $k_1^2 = k_2^2 = 0.026$. In this design, the passband width of each third order MRR switch is 25 GHz. When each block consists of 20 third-order MRR switches, the coupling coefficients for the the MRR switches are $k_0^2 = k_3^2 = 0.0212$, and $k_1^2 = k_2^2 = 0.052$. In this design, the passband width of each third-order MRR switch is 50 GHz.

Figure 5.5 shows the maximal insertion losses of the two-stage switch architectures in Fig. 5.4. Comparing Fig. 5.5 with Fig. 5.3(b), the two-stage switches show higher maximal insertion losses. The reason is that the output light signal intensities dropped from the switches in the first stage are not distributed uniformly into the switches in the second stage as shown in Fig. 5.6.

Figure 5.6(a) and Figure 5.6(b) show the transmission spectrum responses of the MRR switches in the two-stage architecture ($4 \times 80 \times 12.5$ GHz) as shown in Fig. 5.4. As can be seen, the dropped signal intensities show a nonuniform distribution. The insertion losses range from 4.1 to 11.6 dB and from 4.2 to 12.78 dB for the third-order MRR switches with the central wavelengths ranging from 1.538 to 1.546 μm and from 1.546 to 1.554 μm, respectively. The differences of the maximal and minimal insertion losses are 7.5 and 8.67 dB.

Figure 5.6(c) and Figure 5.6(d) show the transmission spectrum response of the MRR switches in the architecture(320×12.5 GHz) as shown in Fig. 5.1. Compared with Fig. 5.6(a) and 5.6(b), they are much better in the uniformity of insertion losses of the switches. The differences of the maximal and minimal insertion losses are 0.46 dB and 0.45 dB that are much less than 7.5 and 8.67 dB. The results in Fig. 5.6 are
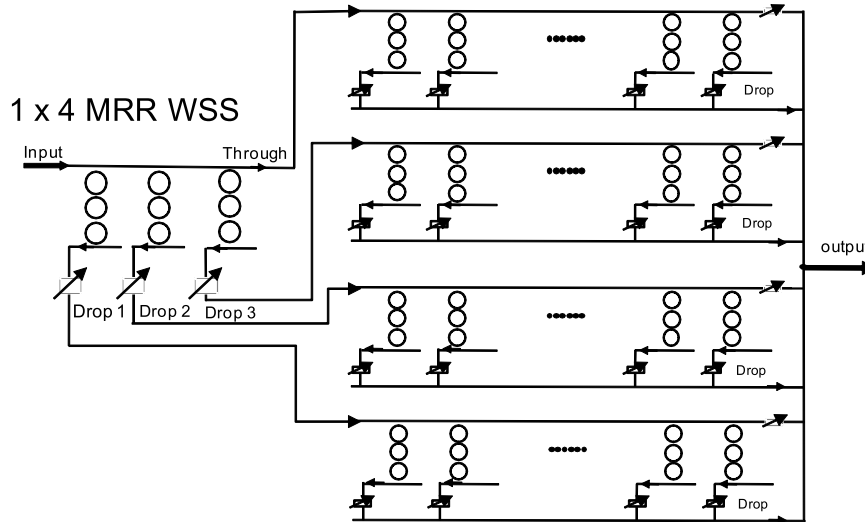
Figure 5.4.   Two-stage switch architecture consisting of one 1×4 MRR WSS and four blocks.
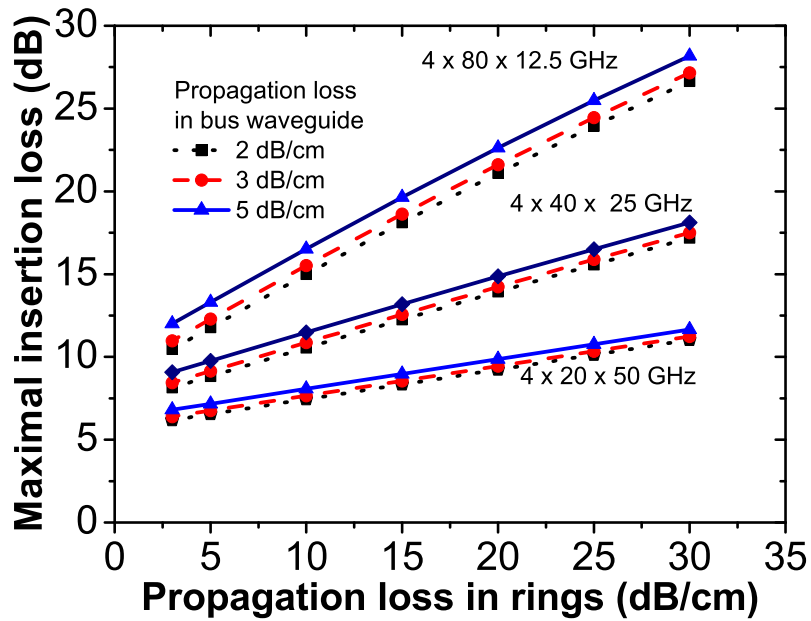
Figure 5.5.   Maximal insertion loss of the two-stage MRR switch architecture as a function of the propagation loss in rings.

(a) Wavelength from 1.538 to 1.546 μm $4 \times 80 \times 12.5$ GHz architecture.

(b) Wavelength from 1.546 to 1.554 μm $4 \times 80 \times 12.5$ GHz architecture.

(c) Wavelength from 1.538 to 1.546 μm 320×12.5 GHz architecture.

(d) Wavelength from 1.538 to 1.546 μm 320×12.5 GHz architecture.
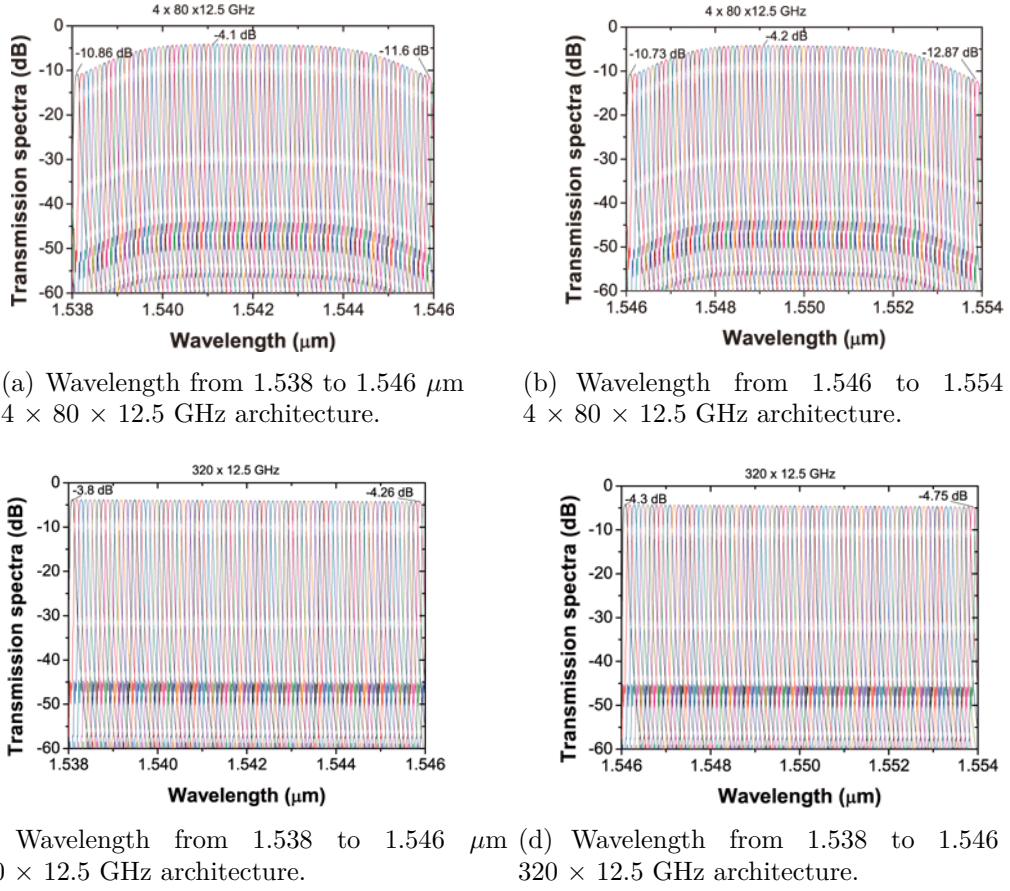
Figure 5.6.   Transmission spectrum response of the MRR switches in the two architectures.

obtained when the propagation losses in all the MRRs for the two architectures are 5 dB/cm while the propagation losses in all the linear bus waveguides are 3 dB/cm.

The nonuniform insertion losses of the MRR switches in the two-stage architecture come from the nonuniform output signal intensities of the switches in the first stage. The output spectra of the switches in the first stage are not rectangular shape as shown in Fig. 5.7. As can be seen in Fig. 5.7, each curve of the output spectra shows that the output signal intensity increases first, then it almost does not change, later it decreases when the wavelength continues to increase.

Moreover, there are light coupling losses between the waveguides at the output ports in the first stage and the input ports in the second stage that are not taken into account in Fig. 5.6(a) and Fig. 5.6(b). The coupling losses between the waveguides at the output ports in the first stage and the input ports in the second stage lead to extra power losses in the two-stage architecture when the signals propagate from
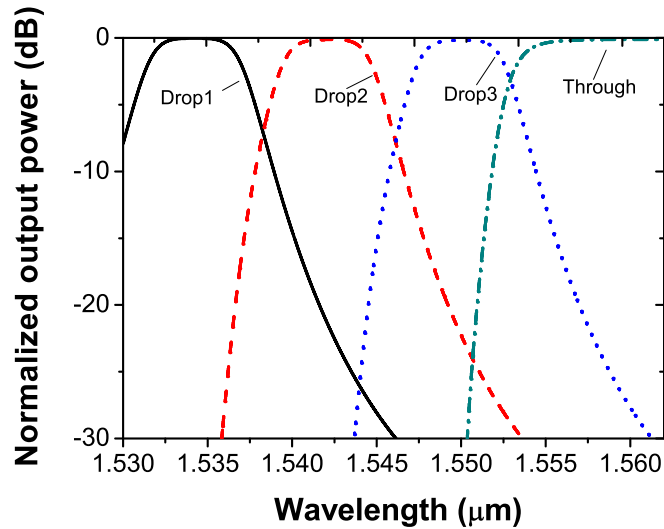
Figure 5.7.   Output spectra of the switches in the first stage of the two-stage MRR switch architecture. Drop1 (Solid line),Drop2 (Dashed line),Drop3 (Dot line), Through (dash dot line)

the switches in the first stage to the second stage, resulting in high insertion loss in the two-stage switch architecture. Therefore, it should be careful to design the two-stage architecture in the wide spectral range.

However, if only a part of light waveband is used in an optical communication system, high insertion loss can be avoided by carefully selecting the light wavelengths.

5.3   Crosstalk Analysis

Crosstalk

Inter-channel crosstalk is a critical issue for optical networks. It leads to the reduction in the signal-to-noise ratios of the signal receivers in optical networks, resulting in the increase in the bit error of the transmission systems. Here we define the inter-channel crosstalk as the ratio of the light power of the adjacent channels at the central wavelength of the wanted channel to that at the central wavelength of the wanted channel as shown in Fig. 5.8. For the definition of the crosstalk, we assume that each third-order MRR switch in the switch architectures occupies a light channel in Fig. 5.8.

Figure 5.9 shows the comparison of the maximal inter-channel crosstalks in the
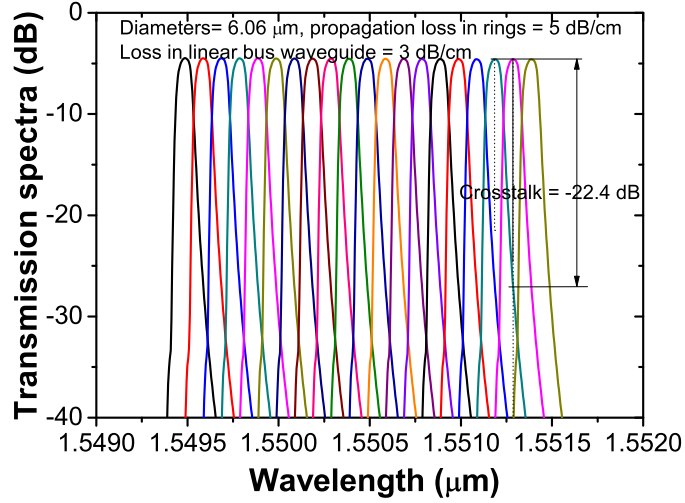
Figure 5.8. Transmission spectra of a switch architecture consisting of 320 third-order microring resonator-based switches with the pass bandwidth of 12.5 GHz and the definition of the inter-channel crosstalk in the switches.

architectures consisting of 320×12.5 GHz, 160×25 GHz, and 80×50 GHz third-order MRRs in Fig. 5.1 with the maximal inter-channel crosstalks in the two stage architectures consisting of 4×80×12.5 GHz, 4×40×25 GHz, and 4×20×50 GHz third-order MRRs in Fig. 5.4. Total spectral bandwidths in all the architectures are 4 THz. The upper curves represent the maximal crosstalks versus the propagation losses in the rings of the two-stage architectures. The lower curves represent the maximal crosstalks versus the propagation losses in the rings of the architectures without stages, i.e. the architectures which consist of 320 MRR switches with the passband widths of 12.5 GHz, or 160 MRR switches with the passband widths of 25 GHz, or 80 MRR switches with the passband widths of 50 GHz. It can be seen that the inter-channel crosstalks increase with the increase in the propagation losses in the MRRs. This is because the propagation losses through the MRR switches increase when the propagation losses in the MRRs increase, resulting in the decrease in the output signal powers of the MRR switches and the increase in the inter-channel crosstalks. It can be also seen that the inter-channel crosstalks for the two types of architectures consisting of the MRR switches with the pass bandwidths of 50 GHz are less than those with the pass bandwidths of 25 and 12.5 GHz at the same propagation losses of the MRRs. This indicates that there are lower inter-channel crosstalks for the two types of architectures when the architectures use the MRR switches with wider passband widths.

Comparing the upper and the lower curves in Fig. 5.9, the two-stage architectures show larger maximal crosstalk values than the architectures in Fig. 5.1, which are caused by nonuniform signal intensity output from the first stage. However, the

65
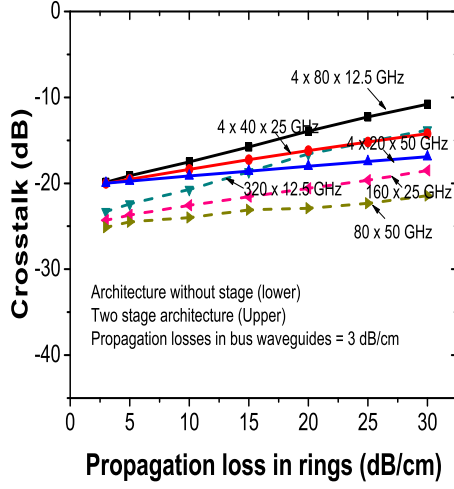
Figure 5.9. Comparison of crosstalks in the two MRR switch architectures when the propagation losses in the MRRs change.
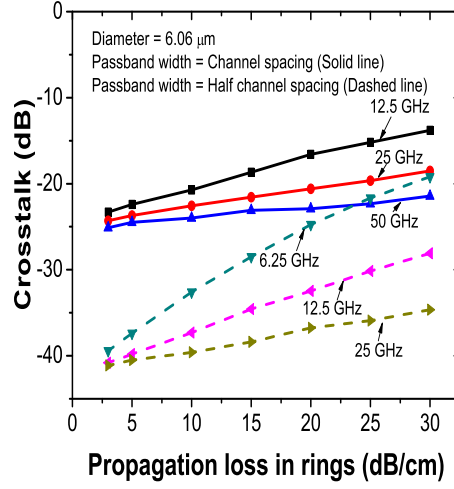
Figure 5.10. Comparison of crosstalks in one MRR switch architecture when the passband widths of the MRR switches change.

worst cases i.e. the maximal crosstalk cases can be avoided by selecting suitable light wavelengths. We note that the curves of the crosstalks are almost same when the propagation losses in linear bus waveguides vary from 2 dB/cm to 5 dB/cm. This means that the propagation losses in linear bus waveguides influences little on the crosstalks in the two architectures.

Techniques to reduce crosstalks

There are several methods to reduce the crosstalks in the two types of architectures. One simple method is to use the MRR switches with narrow passbands. As shown in Fig. 5.10, the crosstalk values can be reduced to -40 dB from -25 dB when the passbands of the MRR switches are reduced a half in the case that all the wanted light channels are output independently from drop ports. In this case, the passband width of each MRR switch is equal to half of the central frequency spacing between neighbor MRR switches. The three upper curves represent the maximal crosstalks as the functions of propagation losses in the MRRs of the switch architecture in Fig. 5.1 when the passband widths of the MRR switches are 12.5, 25, and 50 GHz and when the central frequency spacings between two neighbor MRR swtiches are equal to the passband widths of the MRR switches. The three lower curves represent the maximal crosstalks as the functions of propagation losses in the MRRs

of the the switch architecture in Fig. 5.1 when the passband widths of the MRR switches are 6.25, 12.5, and 25 GHz, but their central frequency spacings between two neighbour MRR switches are 12.5, 25, and 50 GHz respectively. However, using the MRR switches with narrow passbands in the two architectures could incur higher insertion loss because it needs to use smaller coupling coefficients between the MRRs to achieve small passband widths. Smaller coupling coefficients lead to lower output powers of the MRRs.
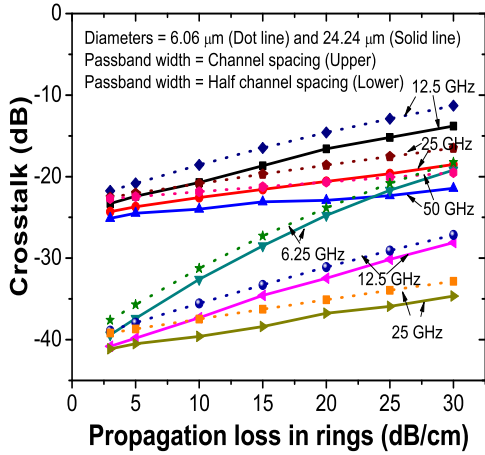
Figure 5.11. Cosstalk comparison for the MRR switchs with different diameters.
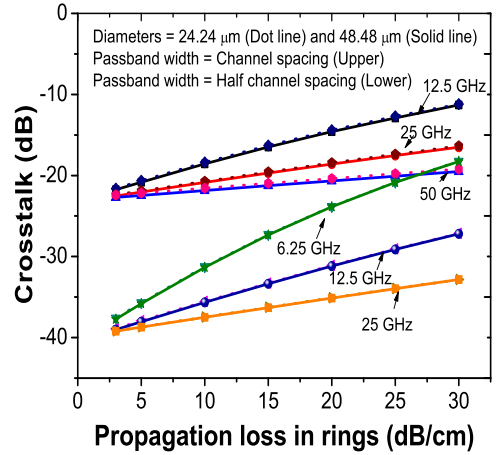
Figure 5.12. Cosstalk comparison for the MRR switchs with different diameters.

Another method is to use larger MRRs instead of the small MRRs in the discussed architectures. Figure 5.11 shows the maximal crosstalks of the switch architectures in Fig. 5.1 as the functions of the propagation losses in the MRRs of the architectures when the MRRs have different diameters. The solid curves represent the maximal crosstalks as the functions of the propagation losses in the MRRs with the diameters of 24.24 μm when the MRR switches have different passband widths. The dot curves represent the maximal crosstalks as the functions of the propagation losses in the MRRs with the diameters of 6.06 μm. For the upper solid and dot curves, the passband widths of the MRR switches are equal to the central frequency spacings between two adjacent MRR switches. For the lower solid and dot curves, the passband widths of the MRR switches are equal to a half of the central frequency spacings between two adjacent MRR switches. It is evident that the crosstalks of the larger MRR switch architectures are smaller than the the crosstalks

67

of the larger MRR switch architectures, indicating that the switch architectures consisting of larger MRRs can reduce the crosstalk. The reason is that steeper edge flat-top spectral passbands can be achieved in the larger MRR switches as discussed in Chapter 3, resulting in lower crosstalks between neighbor channels. However, the larger MRRs will have smaller FSR. The FSR limitation must be considered in the architecture design.

However, when the diameters of the MRRs are greater a critical value, increasing the MRR diameters can not reduce the crosstalks any more. Figure 5.12 shows the maximal crosstalks of the switch architectures in Fig. 5.1 as the functions of the propagation losses in the MRRs of the switch architectures, when the architectures consist of the MRR switches with the diameters of 24.24 and 48.48 μm and when the MRR switches use different passband widths. The solid curves represent the maximal crosstalks as the functions of the propagation losses in the MRRs with the diameters of 48.48 μm when the MRR switches have different passband widths. The dot curves represent the maximal crosstalks as the functions of the propagation losses in the MRRs with the diameters of 24.24 μm. For the upper solid and dot curves, the passband widths of the MRR switches are equal to the central frequency spacings between two adjacent MRR switches. For the lower solid and dot curves, the passband widths of the MRR switches are equal to a half of the central frequency spacings between two adjacent MRR switches. Their curves almost coincide. Thus, there are optimal MRR sizes to achieve the satisfactory crosstalks for the MRR switch architectures.

5.4 Architectures for Reconfigurable Optical Add/Drop Multiplexers

Based on the two switch architectures, we can develop more advanced devices such as flexible-grid reconfigurable optical add/drop multiplexers (ROADM) for optical networks and optical interconnections. The ROADM is an application module that allows software-controlled transparent optical switching of wavelength channels into and out of a fiber in an optical network. The ROADM application is particularly valuable because more dense wavelength-division multiplexing networks are deployed extensively in metropolitan networks, which have a large number of wavelengths and a bandwidth demand that is relatively large and unpredictable even with sophisticated network planning [91]. The ROADM is valuable in this type of network by adding the flexibility in software to "express" individual channels through a node or to "add" and "drop" a wavelength for information access or rerouting along another path in the network.
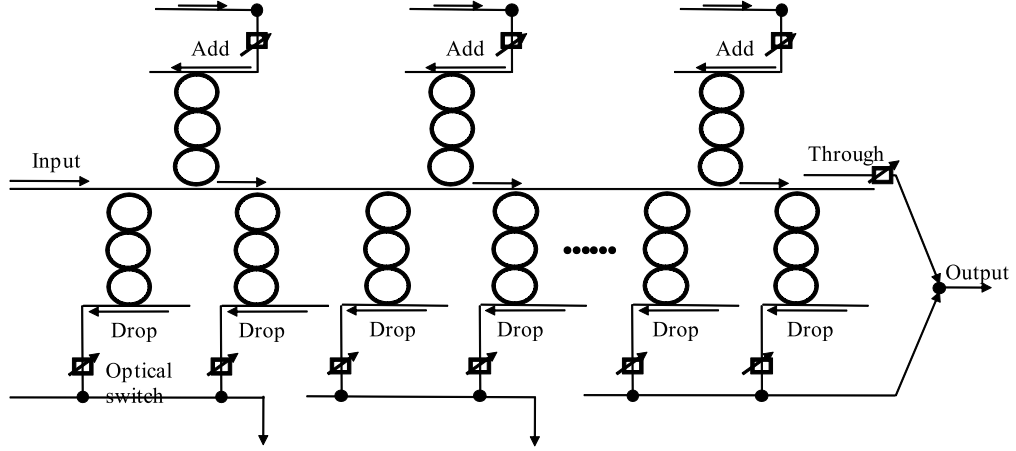
Figure 5.13.   Architectures for reconfigurable optical add/drop multiplexers

Fig. 5.13 shows a reconfigurable optical add/drop multiplexer based on the architecture in 5.1. The new wavelengths or light channels are able to be selected and added from the top MRR switches. Some wavelengths from the input port are selected and dropped from MRR switches at the bottom, depending on the requirements of networks on wavelengths. For the ROADM with high-order MRR switches in Fig. 5.13, wavebands instead of single wavelengths can be added or dropped. The selected wavelengths in ROADM can be changed by tuning the refractive indices of the MRR switches using electro-optic effect and thermo-optic effect as introduced in Chapter 2. The reconfigured operation of the OADM is realized by changing the selected add/drop wavelengths with the refractive index tuning technologies and may be controlled automatically by programming. If the ROADM is applied in Fig. 5.4, we can configure multi-stage optical add/drop multiplexers.

5.5   Conclusions

We designed the MRR switch architectures consisting of 320, 160, and 80 third-order MRR switches with -3 dB passband widths of 12.5, 25, and 50 GHz, respectively, and the two-stage MRR switch architectures consisting of $4 \times 80 \times 12.5$ GHz, $4 \times 40 \times 25$ GHz, and $4 \times 20 \times 50$ GHz. Both architectures are able to achieve variable output bandwidths varying from 0 to 4 THz. Numerical analysis shows that the former is superior to the latter based on the comparison of the maximal insertion losses and crosstalks in the worst cases. However, proper selection of optical spectra used can avoid high insertion losses and serious inter-channel crosstalks in

the latter architecture. Anyway, acceptable insertion losses such as less than 4 dB and low crosstalks such as -20 dB can be achieved in the two architectures by selecting optimal geometrical sizes of their MRRs and the physical parameters of their waveguides.

Chapter 6

Multiple-Input and Multiple-Output Microring-Resonator-Based Wavelength Selective Switches

Microring-resonators-based bandwidth-variable wavelength selective switch architectures with multiple input and output ports are proposed for flexible optical networks in this chapter. The light transmission behaviors of a $1 \times N$ MRR-based WSS are analyzed in detail based on numerical simulation using transfer matrix theory. $N \times N$ MRR-based WSS architectures consisting of only MRR-based WSSs, and consisting of both MRR-based WSSs and optical couplers, are proposed. The architectures show highly variable bandwidths, acceptable losses, high signal crosstalk suppression, and versatile structural design for optical interconnections, and they have potential to be applied for optical interconnections and optical networks, in particular, for high performance computing systems and data center networks.

6.1 Introduction

Continuous growth of traffic stimulates a series of innovations in optical networks and optical interconnections, such as using wavelength routed WDM technology, elastic bandwidth allocation, bandwidth-variable transponders and bandwidth-variable optical cross connects, distance-adaptive spectrum resource allocation, and other technologies to increase transmission capacities and spectral efficiencies of the networks [92–94]. In the innovations, new optical switches and routers with wavelength selection function are needed to meet new demands. Moreover, not only should their spectral passband widths be variable instead of fixed passband widths, but

also multiple functions and large count ports of switch architectures and routers are needed.

As introduced in previous chapters, microring resonators are ideal devices to be used to build wavelength selective switches or optical routers for photonic integrations that are able to adapt to dynamic bandwidth allocations and bandwidth variations in the optical networks or optical interconnections. In a complex optical networks and interconnection networks, specially, when the networks have very large number of optical components, many influencing factors on the performances of basic devices such as optical switches in the networks should be taken into account. In the complex optical networks and interconnection networks built with MRRs, the chromatic dispersion in refractive indices of MRR waveguides and light coupling coefficients between waveguides, the fabrication errors should be taken into account in the design, since accumulated errors and accumulated performance parameter variations could lead to evident variations in light propagation behaviors of the architectures.

In this chapter, we introduce basic principles to design complex MRR-based WSS switches in Section 6.2. We propose $1 \times N$ microring-resonators-based bandwidth-variable wavelength selective switch architectures in Section 6.3. As a proof of concept, the structural design of a one-input and four-output port switch is introduced in detail. The switching performance is evaluated, including the variable passband range of the switch, the insertion loss, and the crosstalk suppression ratio in adjacent channels. Then, we demonstrate $N \times N$ MRR-based WSS architectures. Initial analysis on their performances is shown. Finally we conclude our results in this chapter.

6.2   Basic Principles to Design Complex Microring Resonator Wavelength Selective Switches

6.2.1   Selection of Passband Widths of Microring-Resonator-Based Switches

In this chapter we discuss the design of the complex WSS architectures which consist of cascaded MRRs as shown in Fig. 3.1 as basic switch unit. The structural parameters of a basic MRR switch unit are selected based on the transfer matrix equations Eq. 3.1 - Eq. 3.6. Using the equations, a required transmission spectrum of the MRR switches can be achieved by selecting the structural parameters of MRRs. In particular, the maximal flat-top spectral response may be achieved by arranging the MRRs to be symmetrically distributed in the switches [95], i.e., the light coupling

coefficients between the linear bus waveguides at the input ports and the MRRs of the switches, and between the linear waveguides at the drop ports and the MRRs of the switches are set to the same values. The light coupling coefficients between two adjacent MRRs should be set to those values as reported in [22], so that the maximal flat-top spectrum may be achieved. For the MRR switches consisting of three cascaded MRRs, the coupling coefficients between the linear bus waveguides and the MRRs, and the light coupling coefficients between two adjacent MRRs should meet the equation as $k_1^2 = k_2^2 = 0.25k_0^2 = 0.25k_3^2$.

Passband width is one of the most important parameters of a wavelength selective switch. To select a passband width, we should take two parameters into account for the design. One is the free spectral range of the MRR, another one is the insertion loss of the MRR switch. Both of the parameters are relevant to the MRR diameters. Based on our previous results [95], it is necessary to use larger MRRs for the switch to achieve a narrow bandwidth. If small MRRs are used, it requires very weak coupling between MRRs to achieve such a narrow bandwidth. However high propagation loss occurs in small MRRs due to drastically increased bending loss in the MRRs. Hence there is an optimal combination in the free spectral range and insertion loss of a MRR in order to determine the passband width of a MRR switch.

A larger MRR will have a smaller free spectral range since the free spectral range of a MRR is inversely proportional to its diameter. In a switch with a small FSR, strong light signal interference i.e. crosstalk will occurs if the light signal frequencies cover a wide range that is greater than several FSRs. Assuming a signal at the frequency f_1 can be dropped from a MRR switch, all the signals at the frequencies $f_2 = f_1 + m \times FSR$, where m is an integer, can be also dropped from the switch. This leads to interference or crosstalk between the signals at these frequencies. Therefore, large FSR should be used to avoid the crosstalk between channels. The FSR of a switch should be greater than the frequency range of the input light signals through the MRR switch.

6.2.2 Tuning Central Frequencies of Passbands of Microring Resonator Switches

Microring resonator can be fabricated into a circle or a racetrack shape. The resonant equation of a microring resonator can be re-written in a general format as

$$n(f)L = mc/f \tag{6.1}$$

where L is the perimeter of a MRR, m is the mode number of light propagation in the miroring, and c is the light propagation speed in vacuum. Based on the equation, the passbands of MRR switches can be shifted if the refractive indices of waveguides in the MRRs are changed as introduced in Chapter 2. As shown in

Fig. 6.1, the passbands instead of single frequencies or wavelengths are shifted 125 and 250 GHz when the refractive indices of MRR waveguides are changed 0.0021 and 0.0043 respectively. Exploiting this property we can achieve the passbands with different central frequencies for MRR-based switches.
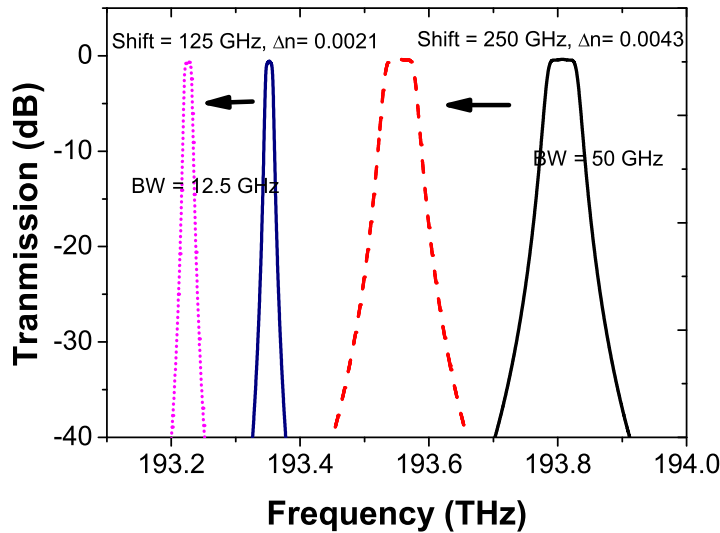
Figure 6.1. Frequency shift of the passbands of a third-order MRR switch with the MRR radii of 12.617 μm by tuning the refractive indices of MRR waveguides. When the refractive index is changed 0.0021, the passband with the width of 12.5 GHz is shifted 125 GHz; When the refractive index is changed 0.0043, the passband with the width of 50 GHz is shifted 250 GHz.

MRRs may be made of different materials. Since silicon material is compatible to large scale integrated circuits used for electronic industry, it is widely investigated to be applied in photonic integrations. The change in refractive indices of silicon waveguides can be achieved using thermo-optic effect or electro-optic effect as introduced in Chapter 2. If using thermo-optic effect, the MRR switches must have electric heaters in the devices to change the temperature of the MRR waveguides. Approximate thermal change of refractive index of silicon may be calculated using Eq. 2.2 [37].

If using electro-optic effect, the MRR switches must have electrodes formed on the inner and outer sides of the MRRs. Changing the injection currents of the electrodes will change the injection electron and hole concentrations in the silicon waveguides, resulting in the change in the refractive indices of the MRR waveguides. The changed value of the refractive index of silicon may be calculated using Eq. 2.1 [37].

6.2.3 Limitation

Chromatic Dispersion

To design wavelength selective switches based on MRRs, several factors to affect the performance of a switch must be taken into account. First, the effect of chromatic dispersion on the transmission spectral response bandwidths of MRR-based switches must be taken into account in the design. The refractive indices of the waveguides of the MRRs change with light propagation wavelengths in the MRRs. The light coupling coefficients between the MRRs, and between the linear waveguides and MRRs also change with the light propagation wavelengths [96]. Using beam propagation method (BPM) and finite element method (FEM) in the software optiBMP [97] to simulate light propagation through a silicon waveguide with the cross section of 0.55 μm wide by 0.22 μm high, the extracted effective indices of the refraction of the silicon waveguides in the MRRs versus the light wavelengths are shown as in Fig. 6.2. It can be seen that the refractive index of the waveguide decreases linearly with the wavelength. The fitting function can be written as $n_{eff} \approx 3.58109 - 0.18365\lambda$, where n_{eff} is the effective refractive index, and λ is the wavelength. Replacing the wavelength with a frequency, we obtain $n_{eff} \approx 3.58109 - 0.18365c/f$, where c is the light speed, f is the light frequency. If written in a general format, the effective effective refractive index of the MRR waveguide is $n_{eff} \approx n_c - 0.18365c(1/f - 1/f_c)$, n_c is the effective refractive index at the central frequency f_c.

Using the BPM and FEM, we extract the light power coupling coefficient between two MRRs as a function of the wavelength represented by the red dashed line in Fig. 6.2 when the gap between the waveguides of the two MRRs is 220 nm. We get the fitting function as $k^2 \approx -0.52906 + 0.3912\lambda$. Replacing the wavelength with the frequency, the function is written as $k^2 \approx -0.52906 + 0.3912c/f$. In a general format, the equation may be written as $k^2 \approx k_c^2 + 0.3912c(1/f - 1/f_c)$ where k_c^2 is the light power coupling coefficient between the MRRs at the central frequency f_c.

The dispersion in the refractive index of a silicon waveguide makes the response spectra of the MRRs move to different wavelength positions. The dispersion in light coupling coefficients leads to the variation in the passband widths and the passband shapes of the MRRs as shown in Fig. 6.3. The passband (black curve) of 12.5 GHz at the central frequency of 193.15 THz is deformed and is narrower than the pass band (red thin curve) of its ideal structure without dispersion, while the passband (blue dashed curve) of 12.5 GHz at the frequency of 193.2 THz is wider than the pass band (blue dot thin curve) of its ideal structure without dispersion. Narrow passbands show relatively strong impact caused by dispersion, compared with wide passbands. The two passbands (wine dot dash curve and violet dot dot dash curve on the right sides) of 50 GHz show relatively weak effect caused by dispersion, compared with the two passbands of 12.5 GHz.
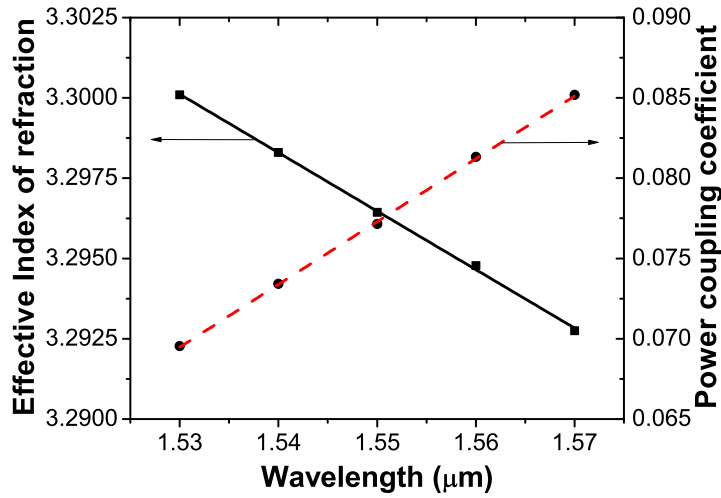
Figure 6.2.   Extracted dispersions of the microring-resonator parameters

Fabrication Errors

In semiconductor device fabrication, there are fabrication errors such as MRR diameter, waveguide width, and height errors, eccentricity of internal and outer circles in MRRs. The diameter error of a MRR leads to a perimeter variation, resulting in varying its resonant wavelength. Current semiconductor device fabrication precision is limited to 10 nm in geometrical dimensions. A 10-nm diameter error of a microring resonator with a diameter of 10 μm could lead to a resonant wavelength shift of 1.5 nm. Such a large resonant wavelength shift could cause high transmission loss or very strong inter-signal interference in some cases.

The waveguide width, height, and section shape determine the light propagation modes in MRR waveguides and the effective refractive indices of the waveguides. The errors in the waveguide width, height, and section shape affect the light propagation modes, lead to the change in the effective refractive index and chromatic dispersion.

Since the wavelengths of light propagation in the MRRs are in the order of one micron magnitude, the surfaces of the MRR waveguides are relatively rough. The rough surfaces of the wavguides cause retro-reflection of the light in the MRR waveduides, resulting in high light propagation loss, serious signal interference, and strong noise.

Thus, in the design of WSSs, the fabrication errors should be taken into account.
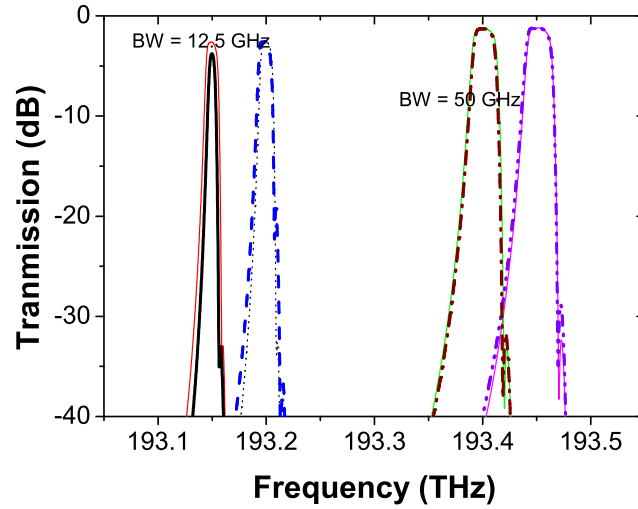
Figure 6.3. Dispersion in light coupling coefficient leads to the change in the passband shapes of the MRRs. The passband (black curve) of 12.5 GHz at the frequency of 193.15 THz is deformed and is narrower than the passband (red thin curve) of its ideal structure without dispersion, while the passband (blue dashed curve) of 12.5 GHz at the frequency of 193.2 THz is wider than the passband (blue dot thin curve) of its ideal structure without dispersion. Narrow passbands show relatively strong impact caused by dispersion, compared with wide passbands. The two passbands (wine dot dash curve and violet dot dot dash curve on the right side) of 50 GHz show weak influence of dispersion, compared with the two passbands of 12.5 GHz on the left side.

Insertion Loss and Cross Talk

The insertion loss of a switch architecture and the crosstalk between adjacent light channels are important parameters to characterize the MRR switch architecture. The insertion losses of MRR switch devices are influenced by the light coupling coefficients between the bus waveguides of the MRR switches and the MRRs, and the light coupling coefficients between the MRRs, and the propagation losses in the MRRs and the bus waveguides. As reported in Chapter 3, when the light coupling coefficients between the bus waveguides and the MRRs and between the MRRs increase, the insertion losses of the MRR switches decrease. There are the minimal insertion losses at optimal diameters for the MRR switches. If the diameters are less than the optimal diameters, the insertion losses of the switches increase drastically, due to drastically increased bending losses in the MRRs. The crosstalks of the MRR switches are influenced mainly by the spectral passband shapes and passband widths. A high insertion loss leads to a low received signal power in a detector while a strong crosstalk leads to a strong signal noise. Both high insertion loss and

strong crosstalk lead to a low signal noise ratio, resulting in a high bit error rate in an optical network. They should be carefully considered in the MRR-based WSS design.

6.3 Multiple-Input and Multiple-Output Microring-Resonator-Based Wavelength Selective Switch Architectures

6.3.1 $1 \times N$ Bandwidth-Variable Microring-Resonator-Based Wavelength Selective Switch Architecture

As an example, a 1×4 bandwidth-variable micro-resonator-based wavelength selective switch architecture is configured as shown in Fig. 6.4. In the architecture, there are one linear bus waveguide, 80 third-order MRR-based switches consisting of three cascaded MRRs. To match the minimal frequency slot width for flexible networks in ITU-T G.694.1, each switch has a pass bandwidth of 12.5 GHz. All the light signals covering a bandwidth of 1 THz are input into the wavelength selective switch from its input port. The light signals can either be dropped by the third-order MRR switches at their resonant frequencies or go through the linear bus waveguide and be output at the end of the linear bus waveguide. The 80 third-order MRR-based switches are divided into 4 groups. Each group consists of 20 third-order MRR-based switches. We assign the MRRs in each group to have same radii. The MRR radii R for the 4 groups of MRR switches are set to 12.617, 12.708, 12.8, and 12.891 μm, respectively. The silicon waveguides of 0.550 μm wide by 0.22 μm high are used for the MRRs and the liner bus waveguides.

The effective refractive indices of the waveguides are calculated to be 3.296 at the wavelength of 1.55 μm by using finite difference method in optiBMP [97]. The refractive index difference of the waveguides in the two adjoining third-order switches is tuned to be approximate 2.15×10^{-4} by using thermo-optic or electro-optic effect. The light coupling coefficients between the linear bus waveguide and the MRRs, and between the linear waveguides at drop ports and the MRRs of the third-order switches are set to $k_0^2 = k_3^2 = 0.0464$. The light coupling coefficients between two MRRs in the third-order switches are set to $k_1^2 = k_2^2 = 0.0116$. The geometrical spacing between the two third-order MRR switches is 50 μm. The footprint of the MRR architecture is about 4 mm long by 0.1 mm wide. The propagation losses through the linear bus waveguides are 2 dB/cm and the propagation losses in the MRRs are 3 dB/cm [98].

The light signals from the MRR switches in a group are dropped into a common linear waveguide. Multiple channels can be dropped from one output port, and the

maximal passband width can be 20×12.5 GHz = 250 GHz at one drop port.
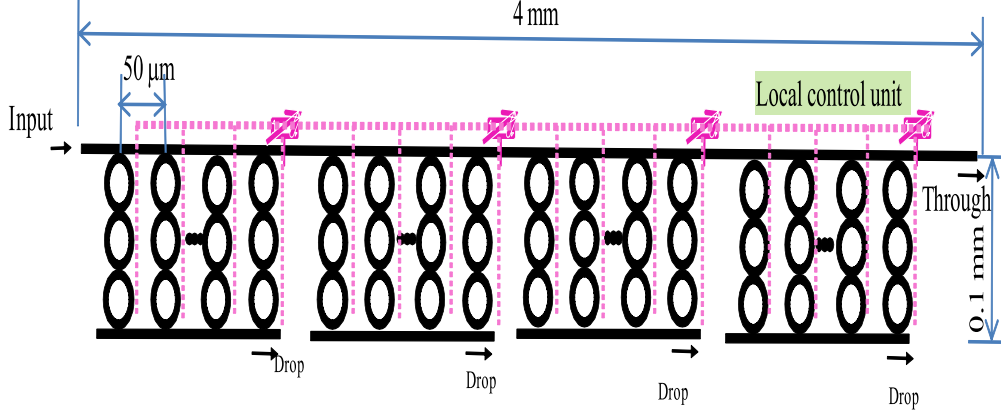
Figure 6.4. Schematic of a bandwidth-variable microring-resonator-based switch architecture consisting of 80 third-order MRR-based switches that are divided into 4 groups. Each group consists of 20 MRR switches with the pass bandwidth of 12.5 GHz. The architecture has 4 multi-channel drop ports with the passband width varying from 0 to 250 GHz that can be achieved by switching on/off a part of MRR switches in a group.

Typical transmission spectra of the switches with different bandwidths and combinations at four drop ports are shown in Fig. 6.5. The variable passband widths of the MRR-based WSSs are achieved by switching on or switching off some or all of the third-order switches. Each third-order switch can be switched on or switched off by tuning refractive index of the waveguide in one of the third-order MRRs through thermo-optic effect [99] or electro-optic effect [37].

Figure 6.5(a),(b),(c) show 4 passbands with the same widths of 12.5, 25, and 50 GHz respectively at four drop ports, but their central frequencies are different. Each drop port outputs one passband. In Fig.6.5(a) the first drop port has the minimal insertion loss 2.05 dB while the fourth drop port has the maximal insertion loss 2.66 dB. Other two drop ports have the insertion losses varying from 2.05 to 2.66 dB. The nonuniform insertion loss is caused not only by different propagation loss in the MRRs and the linear bus waveguide, but also by the light coupling losses between the MRRs and by the light coupling losses between the MRR and the linear waveguide. The light dropped from the first port has the shortest light propagation distance while the light dropped from the fourth port has the maximal light propagation distance, resulting in the minimal and maximal propagation losses. In Fig. 6.5(b) the four drop ports show the insertion losses varying from 2.13 to 2.68 dB. In Fig. 6.5(c) the insertion losses at the four ports vary from 2.15 to 2.69 dB.

Figure 6.5(d) shows 4 different passbands with the widths of 12.5, 25, 50, and

79
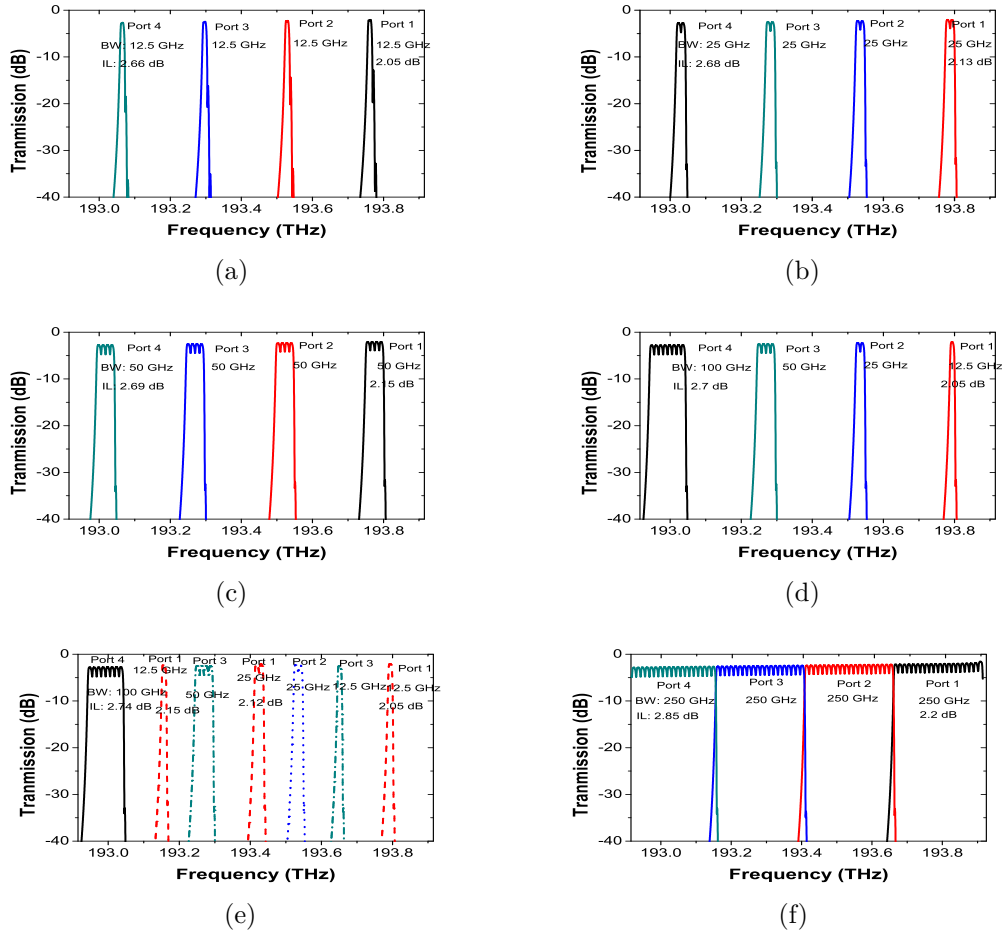
Figure 6.5. Typical transmission spectra of the switches at four drop ports. (a),(b),(c) 4 pass bands with the same widths of 12.5, 25, and 50 GHz respectively but different central frequencies at four drop ports. (d) 4 different pass bands with the widths of 12.5, 25, 50, and 100 GHz and 4 different central frequencies at four drop ports. (e) Two 12.5-GHz-wide passbands and one 25-GHz-wide passband with different central frequencies at Port 1, one 25-GHz-wide passband at Port 2, one 12.5-GHz-wide passband and one 50-GHz-wide passband with different central frequencies at Port 3, and one 100-GHz-wide passband at Port 4. (f) 4 same pass bands of 250 GHz but different central frequencies at four drop ports. The variable passbands are achieved by switching on or off a part of the third-order MRR switches.(a)-(f) The insertion losses at the drop ports vary from 2.05 to 2.85 dB. BW: -3 dB bandwidth; IL: Insertion loss.

100 GHz and 4 different central frequencies dropped from four drop ports. The insertion losses at the four ports vary from 2.05 to 2.7 dB. Figure 6.5(e) shows that several different passbands can be achieved from one drop port and that different

80

drop ports have different output passbands. In Fig. 6.5(e), there are two 12.5-GHz-wide passbands and one 25-GHz-wide passband with different central frequencies at Port 1, one 25-GHz-wide passband at Port 2, one 12.5-GHz-wide passband and one 50-GHz-wide passband with different central frequencies at Port 3, and one 100-GHz-wide passband at Port 4. The insertion losses of the three passbands at the first port vary from 2.05 to 2.15 dB. The 100-GHz-wide passband at Port 4 has the maximal insertion loss 2.74 dB. Figure 6.5(f) shows 4 same pass bands of 250 GHz at different central frequencies dropped from four drop ports. The first drop port has the minimal insertion loss 2.2 dB while the fourth drop port has the maximal insertion loss 2.85 dB. Other two drop ports have the insertion losses varying from 2.2 to 2.85 dB.
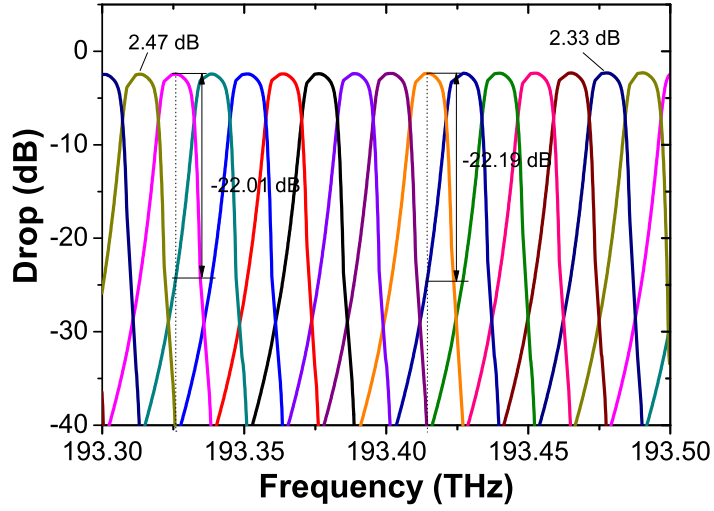
Figure 6.6. Output power spectra of 16 light channels with the bandwidth of 12.5 GHz per channel are shown from one drop port in which 20 light channels can be dropped at the same time in the bandwidth-variable microring-resonator switch architecture. The crosstalk suppression ratio greater than 20 dB between two neighborhood channels are shown. Insertion loss is less than 2.47 dB.

Figure 6.6 shows the independent output power spectra of 16 light channels. Each light channel occupies a bandwidth of 12.5 GHz. As can be seen, the crosstalk between two neighborhood channels vary from -22 to -22.18 dB. It can also seen that the insertion loss for one channel varies from 2.47 to 2.33 dB. The maximal insertion loss is approximately 2.8 dB. Thus the architecture shows low insertion loss and weak crosstalk in adjacent channels, both of them show good uniformity.

If we hope to achieve wider passbands, we can let more third-order MRR switches instead of 20 MRR switches share a linear bus waveguide for light output. Moreover,

we can use the through port of the WSS as one of the light signal output port. In this case, some light signals from the drop ports will be discarded.

6.3.2 $N \times N$ **Bandwidth-Variable Microring-Resonator-Based Wavelength Selective Switch Architecture**

$N \times N$ bandwidth-variable MRR-based wavelength selective switches can be built by using one set of $1 \times N$ bandwidth-variable MRR-based wavelength selective switches and one set of $N \times 1$ bandwidth-variable MRR-based wavelength selective switches, or by using one set of $1 \times N$ bandwidth-variable MRR-based wavelength selective switches and one set of $N \times 1$ optical couplers. Actually, the structure of $1 \times N$ bandwidth-variable MRR-based wavelength selective switches is the same as the $N \times 1$ bandwidth-variable MRR-based wavelength selective switches, except for contrary light propagation directions in the two structures. As an example, we configure two 4×4 bandwidth-variable MRR-based WSSs as shown in Fig. 6.7.
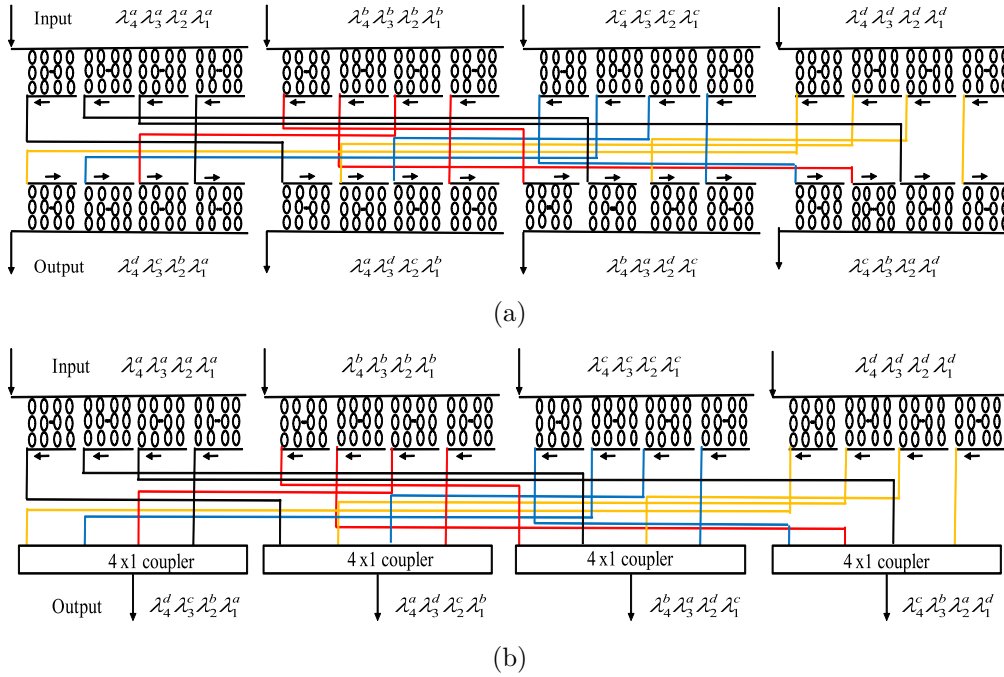
Figure 6.7. Proposed $N \times N$ MRR-based bandwidth variable wavelength selective switches and the wavelength map($N = 4$). (a) Architecture consisting of all WSS at two stages. (b)Architecture built by a combination of WSSs and optical couplers.

In Fig. 6.7(a), the 4×4 WSS consists of four 1×4 MRR WSSs and four 4×1 MRR WSSs. All the MRR WSSs have the same structures and the same parameters. The output signals of the four 1×4 MRR WSSs at the first stage (Top)

82

are separated and are sent to the input ports of the four 4×1 MRR WSSs at the second stage (Bottom) independently. The output signal at any drop port of any WSS at the first stage contains a waveband of which the bandwidth is variable. The variable bandwidth is achieved by switching on/off some of the MRR switches at the first stage through wavelength tuning of the MRRs. The signals will be further filtered and selected by the WSSs at the second stage. Moreover, some light signals can be stopped by the WSSs at the second stage when the MRR switches are turned off.

In Fig. 6.7(b), the switch consists of four 1×4 MRR WSS at the first stage and four optical couplers instead of the WSSs at the second stages. The output signals of the four 1×4 MRR WSSs at the first stage are separated and are sent to the four 4×1 optical couplers at the second stage independently. The output signal at any drop port of any WSS at the first stage contains a waveband of which the bandwidth is variable. However, the light signals from the drop ports of the WSSs at the first stage can not be filtered and selected in the couplers at the second stage. But the optical couplers have small insertion loss and they are cheaper than the WSSs.

Comparing the two architectures in Fig. 6.7, it is found that steeper-edge flat-top passband can be achieved in the WSS-WSS architecture in Fig. 6.7(a) than in the WSS-Coupler architecture in Fig. 6.7(b). As shown in Fig. 6.8, when the final output ports of the two architectures have same passband widths of 12.5, 25, and 50 GHz respectively, the passband curves (The red, dark cyan, and magenta dot lines) achieved in the WSS-WSS architecture show steeper edges than ones (The black solid, dash, and dash dot lines) achieved in the WSS-Coupler architecture. This is because the passbands of the switch architecture in Fig. 6.7(a) are filtered further at the second stage. Steeper edge passband of a WSS will have a lower inter-channel crosstalk, benefiting to signal transmission in the network. However, the passband curves achieved in the WSS-WSS architecture show respectively lower output power than ones achieved in the WSS-Coupler architecture when the architectures have the same output spectral passbands. This means that the insertion loss of the WSS-WSS architecture is higher than the loss of the WSS-Coupler architecture since the optical couplers at the second stage of WSS-Coupler architecture have much lower insertion loss than the WSSs at the second stage of WSS-WSS architecture.

Figure 6.9(a) shows the independent output power spectra of the light channels of the WSS-WSS architecture when each light channel occupies the passband width of 12.5 GHz. The average crosstalk between two adjacent channels is -25.4 dB. The average insertion loss is 4.75 dB. The maximal insertion loss is 6.35 dB that is not shown in the figure. Figure 6.9(b) shows the independent output power spectra of the light channels of the WSS-Coupler switch architecture when each light channel occupies the passband width of 12.5 GHz. The average crosstalk between two adjacent channels is -22.1 dB. The average insertion loss is 2.6 dB. The maximal insertion loss is 4.2 dB that is not shown in the figure.
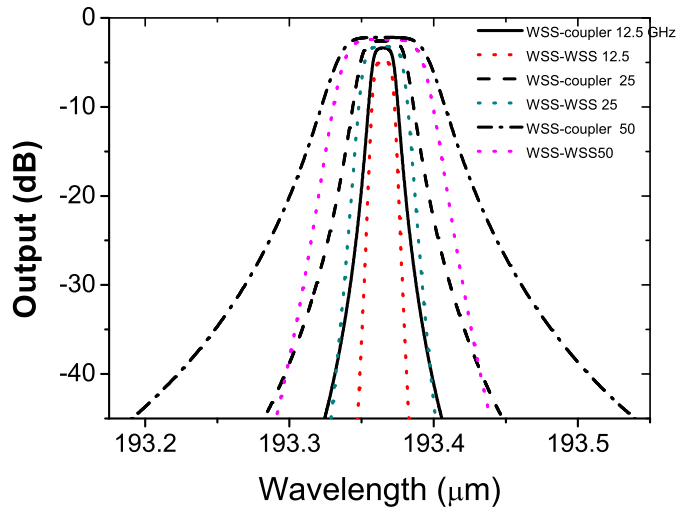
Figure 6.8. Transmission responses of the two 4×4 microring-resonator-based wavelength selective switch architectures when each third-order MRR switch has the passbands of 12.5, 25, and 50 GHz. WSS-WSS denotes the 4×4 switch architecture consisting of 1×4 WSSs totally. WSS-Coupler denotes the 4×4 switch architecture consisting of 1×4 WSSs at the first stage and the optical couplers at the second stages.

(a) WSS-WSS

(b) WSS-Coupler
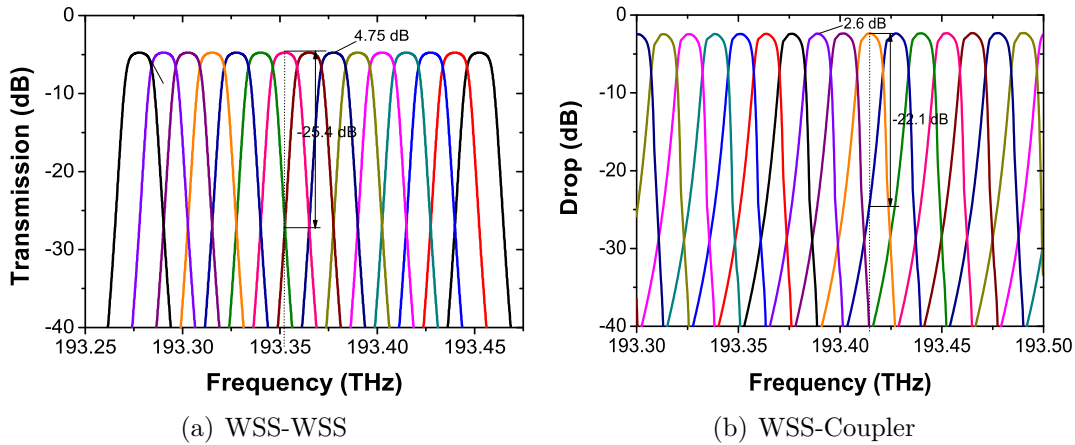
Figure 6.9. (a) Independent output power spectra of the light channels of the WSS-WSS switch architecture. The average crosstalk between two adjacent channels is -25.4 dB. The average insertion loss is 4.75 dB. (b)Independent output power spectra of the light channels of the WSS-Coupler switch architecture. The average crosstalk between two adjacent channels is -22.1 dB. The average insertion loss is 2.6 dB.

84

Table 6.1.   Comparison of 4×4 WSS-WSS and WSS-Coupler architectures

Property	WSS-WSS	WSS-Coupler
Average insertion loss (dB)	4.75	2.6
Worst insertion loss (dB)	6.35	4.2
Average adjacent channel crosstalk (dB)	-25.4	-22.1
Cost	High	Low

Thus the WSS-WSS architecture shows lower inter-channel crosstalk but higher insertion loss than the WSS-Coupler architecture. The WSS-WSS architecture has steeper edge flat-top spectral passband than the WSS-Coupler architecture. But the cost in the fabrication of the WSS-WSS architecture is evident to be higher than the WSS-Coupler architecture, and its structure arrangement is more complicated than the WSS-Coupler architecture. In a word, both architectures have their own advantages and drawbacks. They are summarized in Table 6.1.

6.4   Conclusions

We proposed bandwidth-variable MRR-based wavelength selective switches with multiple input and multiple output ports. We gave a detailed analysis on the switches consisting of the third-order microring resonators. By switching on or off a part or all of the third-order microring-resonators-based switches via tuning the refractive indices of the waveguides in the MRRs, the passbands with variable widths in a very large range are able to be achieved. For the 4×4 switch in the example the the passbands with variable widths from 12.5 to 250 GHz at one output port were demonstrated. The average insertion losses are estimated to be 4.75 and 2.6 dB, and the average adjacent channel crosstalks are -25.4 and -22.1 dB respectively for the WSS-WSS and WSS-Coupler architectures when the diameters of the MRRs in the architectures are around 12 μm and their passband widths are 12.5 GHz. If the passband widths of the MRR switches as the basic units of the WSS switches are increased, the insertion losses of the WSS switches will be reduced and the crosstalks will get lower. These losses and inter-channel signal crosstalks of the proposed bandwidth-variable microring-resonator-based wavelength selective switches are acceptable for the applications in optical networks on chip and optical communication networks.

Compared with the WSSs made of liquid crystal on silicon (LCoS)spatial light modulators (SLMs), the proposed MRR-based architectures have evident advantages. Typically, LCoS-SLMs WSSs available on market have large volume such as $200 \times 150 \times 30$ mm and they show high insertion loss of $2 \times 6 = 12$ dB when

cascading two LCoS WSSs. The proposed switches have small volumes with the widths of microns and the lengths of several millimeters, and they can be integrated in large scale. Moreover, the MRR-based WSSs could be superior to the LCoS WSSs in low power consumption, relatively simple device fabrication technology.

The proposed MRR-based architectures are also superior to the WSSs consisting of cyclic array waveguide gratings (AWG)s in several aspects such as in versatile structural design, light switching control. In particular, the passband widths of the proposed architectures can be varied in a very large range from a few GHz to a few THz while it is relatively difficult to use AWG switches to do so. Thus the proposed bandwidth-variable microring-resonator-based wavelength selective switches have the potential to replace in part or completely the LCoS and AWG WSS switches for the applications in the optical networks, in particular, for high performance computing systems and data center networks.

Chapter 7

Performance Studies of Optical Interconnections Based on Microring Resonators

In this chapter, a scalable optical interconnection architecture based on MRRs is proposed. The optical interconnect architecture consists mainly of microring resonator devices: microring lasers, microring switches, microring de-multiplexers, and integrated photodectors. The performance of the architecture is studied. The simulation on the end-to-end latencies and the packet loss rates of the architecture under large traffic loads shows that the architecture proposed has potential to be integrated on a chip scale CMOS-compatible silicon photonic platform.

7.1 Introduction

Scalable, low latency, and high-throughput interconnection is essential for future high performance interconnect networks such as high performance computing systems and data center networks. Interconnect networks based on electronic multi-stage topologies have large latencies due to the multi-hop nature of these networks, and high power consumption in the buffers and the switch fabrics.

As global internet traffic growing exponentially, the data centers, which host many internet application servers, are facing rapid increase in bandwidth demands. Furthermore, as more and more processing cores are integrated into a single chip [100], the communication speeds between racks in the data centers will become slow and the communication times between racks increase significantly. Fast and low-latency interconnection schemes are required for the cores to communicate with the storage systems and the other servers inside or outside of the racks so that data centers can achieve low latency, large throughput, high flexibility, high resource

efficiency, low power consumption, and low cost.

Recent advances in key components of integrated photonic circuits, such as large-port-count low-loss silicon arrayed waveguide gratings [101], Si ring modulators [102], high-responsivity epitaxial germanium photodetectors [103], hybrid semiconductor optical amplifiers [104], and hybrid semiconductor laser sources [105], are paving the way for device integration in large chip-scale optical switch systems. Integrated optics may meet the requirements of future high performance computing systems and data centers.

A scalable chip-scale integrated optical interconnect architecture was proposed [106]. In the architecture, the key optical component is a cyclic arrayed waveguide grating (CAWG). The modulators as wavelength multiplexers for the signal transmitters at the input side of the CAWG and the wavelength de-multiplexers for the signal receivers at the output side of the CAWG are composed of microring resonators. Since the process and technique to fabricate CAWGs are more complicated than to fabricate microrings, we propose to build a scalable interconnect network using a microring resonator switch to replace the CAWG for the architecture. In addition, the transmitters in the optical interconnect architecture reported [106] are made up of off-chip comb lasers, a 1 × N splitter, and MRR modulators. The lights from the off-chip comb lasers are coupled into a 1 × N splitter and are separated into different nodes at the input side of the CAWG. Then the lights are modulated by the microring modulators. Here we propose to use directly modulated wavelength-multiplexed integrated microring laser arrays to replace the the off-chip lasers, the splitter, and the modulators for the architecture, due to the fact that directly modulated wavelength-multiplexed integrated microring laser arrays on chips are available [107]. The application of directly modulated laser arrays as the transmitters of the architecture will simplify greatly the optical interconnection architecture and reduce the transmission power losses in the architecture.

In the chapter, the performance of the proposed MRR optical interconnection architecture is studied by simulating the end-to-end transmission latencies and packet loss rates under high traffic loads. It will demonstrate if it is feasible to build MRR WSSs for flexible grid on-chip networks and to develop advanced optical interconnects and optical networks. The optical interconnect network is simulated using OMNet++.

7.2 Optical Interconnect Architecture

The proposed optical interconnect architecture is shown in Fig. 7.1. The architecture is made up of MRR lasers as transmitters, a N × N MRR switch, MRR de-multiplexers, and integrated photodectectors. We assume a centralized control plane here for simplicity. At the input side of the N × N MRR switch, there are N
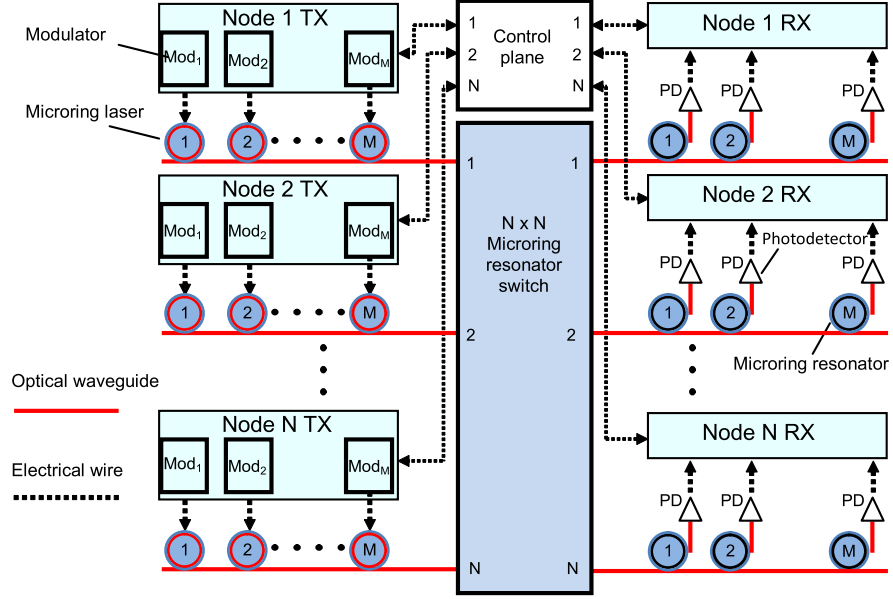
Figure 7.1.   Proposed microring-resonator-interconnect architecture.

nodes. Each node has a transmitter array that uses M microring lasers modulated directly by signal modulators to generate the data packets. At the output side, there are also N nodes. Each node has one $1 \times M$ MRR de-multiplexer and M integrated photodectectors to receive and measure the signals. There are many choices for the $N \times N$ MRR switch. Here we use the $N \times N$ MRR switch configured in Fig. 6.7(b) that is the same as Fig. 7.2(a) or use the MRR switch as shown in Fig. 7.2(b) proposed in [108]. Figure 7.2(a) is a typical MRR based $N \times N$ switch at N = 4. The signals from one input port are distributed into different output ports. The signals at different wavelengths or frequencies from different input ports combine at one output port. The signals are allocated by turning-on/off the third-order MRR switches in the $N \times N$ MRR switch. Figure 7.2(b) is a compact cross-and-bar MRR optical interconnect architecture that can be used as the switch at N = 4 [108]. It has the same function as Fig. 7.2(a).

7.3   Performance Evaluation of Microring Resonator Interconnect Architecture

We evaluate the end-to-end time latencies, packet loss rates, and throughputs of the proposed optical interconnect architecture. The simulated parameters are similar to those reported in [106]. We assume uniform random traffic with a packet size

of 1024B in all the simulations. The inter-arrival time between two packets follows Bernoulli distribution. The line rate is set at 10 Gb/s. We define the maximum offered load as N × line rate. For each node, there is a 16-kB input buffer for each transmitter. There is a 10-ns guard time between any two consecutive transmissions due to the ring reconfiguration time. The control plane runs a 2-GHz clock and takes three clock cycles to make an arbitration for each request. The control plane handles all the contentions based on round robin arbitration. The transmitter will send out the next packet right after it gets the permission while the contended packet will stay in the input buffer and wait for the next grant. The transmitter will send a new request to the control plane immediately after a failed attempt or a successful packet transmission.

(a) 4 × 4 microring resonator switch.

(b) 4 × 4 microring resonator switch.
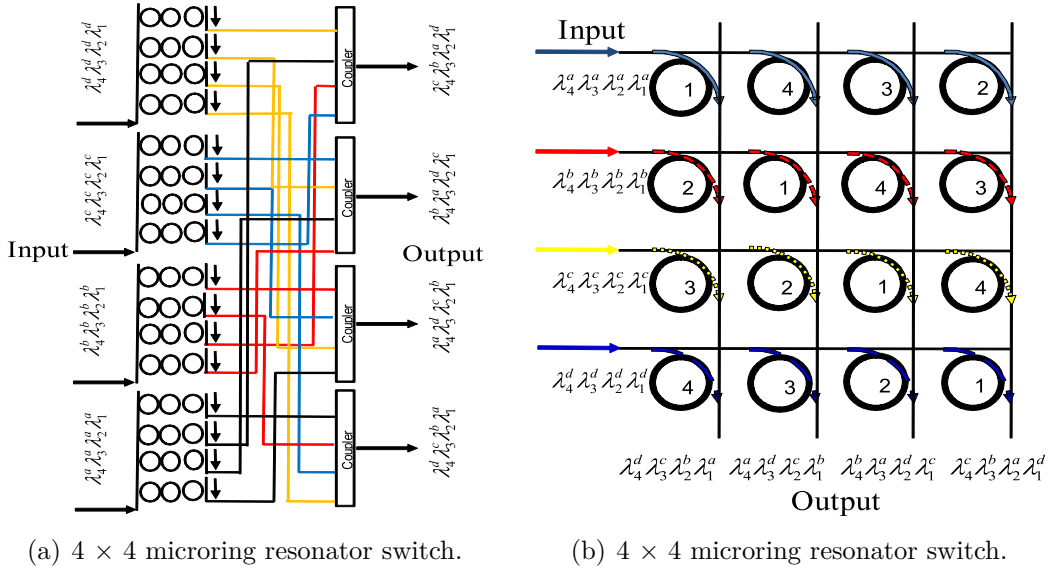
Figure 7.2.   Two typical N × N microring resonator switches

Figure 7.3 shows the average end-to-end transmission time latency as the function of normalized average load of the MRR interconnect architecture with 4, 8, 16, 32, and 64 nodes on the two sides of the N × N MRR switch. Figure 7.4 shows the average packet loss rate as a function of the normalized average traffic load for the proposed interconnect architecture. The normalized load is defined as the ratio of the simulated load divided by the maximal throughput of the architecture at a node number. The transmission capacity of the interconnection architecture changes with the node number. The simulated loads and corresponding throughputs are shown in Fig. 7.5. The throughput increases from 160 Gb/s to 40.96 Tb/s when the node numbers at the input side and output side of the MRR switch increase from 4 to 64.

It is evident that the architecture with large number of nodes and larger loads shows larger end-to-end time latencies, since the control center needs more time to
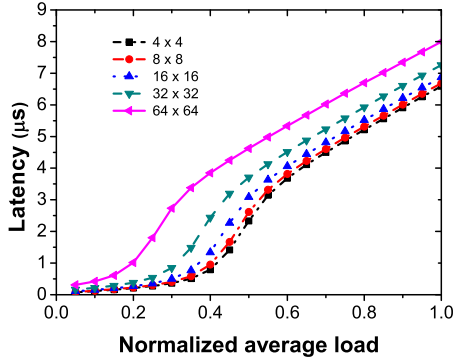
Figure 7.3. Average end-to-end latency as a function of normalized average traffic load for proposed interconnect architecture.
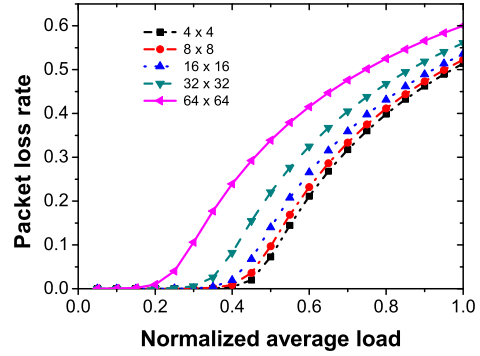
Figure 7.4. Average packet loss rate as a function of the normalized average traffic load for the proposed interconnect architecture.

arbitrate and check the request of all the nodes. The latency increases when the traffic load increases, and there are a turning point of the load at which the latency increases drastically as shown in Fig. 7.3. For instance, when the loads of the architecture with 4, 8 and 16 nodes are larger than 40% of their maximal throughputs, their latencies increase from 1 μs to longer than 4 μs, while the latencies are much shorter than 1 μs when the loads are less than their turning points. Correspondingly, the packet loss rates increase drastically after the turning points as shown in Fig. 7.4. As can be seen that their average end-to-end time latencies of the interconnect architecture are less than 8 μs. This indicates that the architecture has satisfactory end-to-end latency.

The packet loss rates of the interconnect architecture influences on the bit error ratio of the received signals. As can be seen in Fig. 7.4 that the packet loss rates of the architecture with 4, 8, 16 nodes are less than 0.5% when the loads are less than 40% of their maximal throughputs, i.e., when the throughputs are 64, 256, 1024 Gb/s. The packet loss rate of the architecture with 32 nodes is less than 0.5% when the load is less than 30% of its maximal throughput, corresponding to the throughput of 3.072 Tb/s. The packet loss rate of the architecture with 64 nodes is less than 0.5% when the load is less than 20% of its maximal throughput, corresponding to the throughput of 8.192 Tb/s.

7.4 Conclusions

In this chapter a simple but typical chip-scale scalable optical interconnect architecture based on MRRs was proposed and the performance of the architecture was
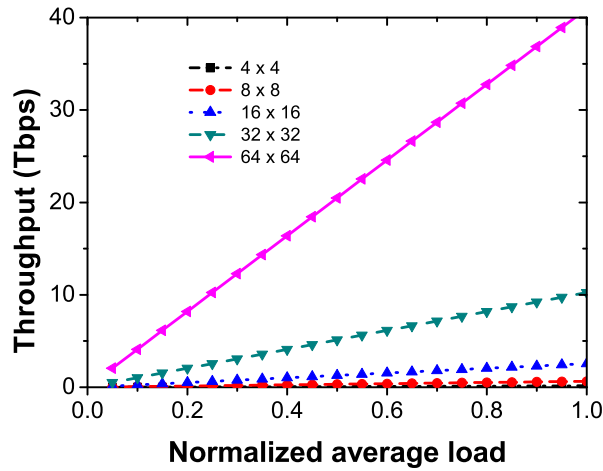
Figure 7.5.   Average throughput of the proposed interconnect architecture.

studied by simulating its end-to-end transmission time latencies and its transmission packet loss rates. The interconnect architecture makes up of mainly of microring resonator devices: microring lasers, microring switches, microring de-multiplexers, and integrated photodectors. Numerical simulation showed the low latencies of 8 μs and the low packet losses of 0.5% at high load of 3 Tb/s when the node numbers at both input and output sides of the interconnect architecture are less than 64. The results indicate that it is feasible to build high performance flexible grid on-chip optical networks and advanced optical interconnects using MRR-based devices.

Chapter 8

Conclusions

The research work of the dissertation is focused on investigating how to develop microring-resonator-based switches and switch architectures for possible applications not only in flexible-grid on-chip networks but also in optical interconnection networks for optical communication systems. Basic properties and performances of the switches and the switch architectures are investigated related to their applications in the networks. The results show that high performance, large bandwidth varying range, low insertion loss, low crosstalk optical MRR-based switches and switch architectures can be achieved to meet the requirements of flexible-grid networks.

The physical characteristics of microring resonator switch devices were thoroughly analyzed using a developed model based on the field coupling matrix theory. The spectral response and insertion loss properties of these switching devices were simulated using the developed model. Results show that they are influenced by the number of cascaded MRRs, the coupling coefficients between the bus waveguides of the switch devices and the MRRs and between the MRRs, the MRR diameters, and the propagation losses in the MRR switch devices. The main factors affecting the passband widths of the MRR switch devices are the diameters of the MRRs, the coupling coefficients between the bus waveguides and the MRRs and between the MRRs, and the ring numbers. The bandwidths increase with the increase in the coupling coefficients between the waveguides and the MRRs and between the MRRs. Using smaller MRRs can achieve larger passband widths in the switches. Cascading multiple MRRs can achieve flat-top passbands in the switches by optimal design which can improve the uniformity of the power distribution in the optical networks. When the coupling coefficients between the bus waveguides and the MRRs and between the MRRs increase, the transmission losses of the switches decrease. However, there are optimal diameters to achieve satisfactory insertion losses. When the diameters of the MRRs are smaller than a threshold value, the losses increase drastically when the diameters decrease due to drastically increased bending losses

in the MRRs. If the diameters of the MRRs are greater than a threshold value, the losses also increase with the increase in the diameters. Results show that it is possible to achieve flat-top passband widths ranging from 6.25 GHz to 3 THz by cascading three microring resonators, while having insertion losses compatible with the use in flexible-grid optical communication networks. The architectures of simple optical switches with limited functionalities and the pass bandwidths of 12.5, 25, and 50 GHz as well as the combination of these pass bands were demonstrated. Satisfactory transmission spectra and low insertion losses of these devices were achieved, showing the potential use in scalable flexible wavelength selective switches.

The MRR switch architectures consisting of 320, 160, and 80 third-order MRR switches with -3 dB passband widths of 12.5, 25, and 50 GHz, respectively and the two-stage MRR switch architectures consisting of 4 × 80 × 12.5 GHz, 4 × 40 × 25 GHz, and 4 × 20 × 50 GHz were investigated. Both architectures are able to achieve variable output bandwidths varying from 0 to 4 THz. Results show that the former is superior to the latter based on the comparison of the maximal insertion losses and the crosstalks in the worst cases. However, suitable selection of optical spectra can avoid high insertion losses and high crosstalks of the adjacent channels in the latter architecture. Anyway, acceptable insertion losses such as less than 4 dB and acceptable crosstalks such as -20 dB can be achieved in the two architectures by selecting suitable geometrical sizes and the physical parameters of the MRRs in the architectures.

The spectral shapes of the passbands of cascaded MRR switches and multistage cascaded MRR switches were investigated in detail. The results show that steep-edge flat-top spectral responses at the drop ports of the multistage MRR-based switches were achieved. Increasing stage number can obtain steeper-edge response spectra of the multistage MRR-based switches, however it also increases the transmission losses of the switches. The simulation shows that the multistage cascaded MRR-based switches provide better passband properties than the cascaded MRR-based switches without stages. Clear, regular, smooth, steep roll-off edge flat-top passpands were achieved in the multistage cascaded MRR-based switches. Irregular and fluctuating passpands were shown in the high-order MRR-based switches without stages. In order to achieve steep-edge flat-top passpands in MRR switches or filters, it is better to use the multistage cascaded MRR structures with optimal design instead of the simple cascaded structures without stages. But there is a trade-off between insertion losses and passband widths to achieve an optimal performance in the switch design.

Bandwidth-variable microring-resonator-based wavelength selective switches with multiple input and multiple output ports were proposed. A detailed analysis was given on the performances of the switches consisting of the third-order microring resonators. As a proof of concept, the structural design of 4 × 4 wavelength selective switches was investigated in detail. The results show that the average insertion losses are 2.6 and 4.75 dB, and the average adjacent channel crosstalks are -25.4 to

-22.1 dB respectively for the WSS-WSS and WSS-Coupler architectures when the diameters of the MRRs in the architectures are around 12 μm and their passband widths are 12.5 GHz. The insertion losses and signal crosstalks are acceptable for the switches to be applied in on-chip optical networks and optical communication networks. Deep research works show that the MRR-based WSSs are superior to the WSSs based on the liquid crystal on silicon spatial light modulators due to lower power consumption, and easier device fabrication technology. In particular, the proposed MRR-based architectures are superior to the WSSs based on cyclic array waveguide gratings in structural design versatility, light switching control agility, and passband width adjustment, implying that the proposed bandwidth-variable microring-resonator-based wavelength selective switches have the potential to replace in part or completely the LCoS and AWG switches for the applications in the optical networks, in particular, for high performance computing systems and data center networks.

A chip-scale optical interconnect architecture, which mainly consists of MRR devices (MRR lasers, MRR switches, and MRR demultiplexers), was proposed. The performance of the optical interconnect architecture was studied by simulating the end-to-end time latencies and the transmission packet loss rates at large throughputs using OMNet++, indicating that it is feasible to build MRR WSSs for flexible grid on-chip networks and to develop advanced optical interconnects and optical networks. The results demonstrated low latencies and low packet losses at large throughputs in the proposed chip-scale optical interconnect architecture.

Mircroring resonator-based devices are relatively difficult to be fabricated with relatively high cost using current industrial technologies. Tentative fabrications are under the way. The research works of the dissertation were done mainly based on the theoretical aspects and the numerical simulations due to the limitation of current fabrication technologies, the lack of the experimental setups, and the shortage of measuring instruments on the MRR-based devices.

Future works will be focused on three aspects: 1) MRR switch device fabrication, experiment, and fabrication error impact research. 2)MRR device polarization independence research. 3)Large scale integration theory based on MRR devices and photonic integration technology research.

In the research works of the dissertation, all the devices are assumed to have ideal properties, precise structural sizes, and perfect structure shapes. However, in a practical fabrication, there are fabrication errors in MRR diameters, waveguide widths, and heights. The MRRs have eccentricities of internal and outer circles. The surfaces of the waveguides of the MRRs are not smooth and they have roughness to some degree.

The diameter error of a MRR will change its perimeter, thus changing its resonant wavelength. The waveguide widths, heights, and section shapes of the MRRs

determine the light propagation modes in the MRR waveguides and the effective refractive indices of the waveguides. The errors in the widths, heights, and waveguide shapes of the MRRs will change the light propagation modes in the waveguides, the effective refractive indices of the waveguides, and the light coupling coefficients between the waveguides, thus changing the transmission response spectra of the MRR devices, increasing the insertion losses, and increasing signal noises.

A rough surface of a waveguide leads to light scattering in the waveguide, resulting in light propagation loss and retro-reflection. The retro-reflection will incur signal interferences in optical networks.

Silicon has a large refractive index. The high refractive index contrast between silicon and cladding media in the waveguides makes a strong light confinement but a strong polarization dependence of light propagation in the waveuides. TE and TM polarization lights have different propagation behaviors in the waveguides. Nevertheless, the optical devices in optical networks usually require that the light propagation behaviours in the devices are not sensitive to the light polarization. Actually, proper waveguide structure design may improve the polarization sensitivity of the light propagation behaviors in the waveguides.

Repaid progress in silicon photonic integration technology paves a way for large scale integration of silicon photonic devices. The large scale integration was not discussed in the dissertation.

These works mentioned here were not done in the dissertation due to the limitation in facilities, instruments, and time. They will be future works in next step.

Bibliography

[1] I. Tomkos, S. Azodolmolky, J. Sole-Pareta, D. Careglio, and E. Palkopoulou, "A tutorial on the flexible optical networking paradigm: State of the art, trends, and research challenges," *Proceedings of the IEEE*, vol. 102, no. 9, pp. 1317–1337, 2014.

[2] *Spectral grids for WDM applications: DWDM frequency grid, Recommendation ITU-T G.694.1*, 2nd ed., International Telecommunication Union – Telecommunication Standardization Sector (ITU-T), Geneva, Switzerland, Feb. 2012.

[3] S. Poole, S. Frisken, M. Roelens, and C. Cameron, "Bandwidth-flexible ROADMs as network elements," in *Optical Fiber Communication Conference and Collocated National Fiber Optic Engineers Conference*, 2011, oTuE1.

[4] J. K. Rhee, F. Garcia, A. Ellis, B. Hallock, T. Kennedy, T. Lackey, R. Lindquist, J. P. Kondis, B. A. Scott, J. M. Harris, D. Wolf, , and M. Dugan, "Variable passband optical add-drop multiplexer using wavelength selective switch," in *Proceedings of 27th European Conference on Optical Communcations*, Amsterdam, 2001, pp. 550–551, th.L.I.7.

[5] J. Ford, V. Aksyuk, D. J. Bishop, and J. Walker, "Wavelength add-drop switching using tilting micromirrors," *Journal of Lightwave and Technology*, vol. 17, no. 5, pp. 904–911, 1999.

[6] C. Stamatiadis, K. Vyrsokinos, L. Stampoulidis, I. Lazarou, A. Maziotis, J. Bolten, M. Karl, T. Wahlbrink, P. D. Heyn, Z. Sheng, D. V. Thourhout, and H. Avramopoulos, "Wavelength-selective $1 \times k$ switches using free-space optics and MEMS micromirrors: Theory, design, and implementation," *Journal of Lightwave and Technology*, vol. 23, no. 4, pp. 1620–1630, 2005.

[7] S. Suzuki, A. Himeno, and M. Ishii, "Integrated multichannel optical wavelength selective switches incorporating an arrayed-waveguide grating multiplexer and thermooptic switches," *Journal of Lightwave and Technology*, vol. 16, no. 4, pp. 650–655, 1998.

[8] G. Duan, C. Jany, A. Le Liepvre, A. Accard, M. Lamponi, D. Make, P. Kaspar, G. Levaufre, N. Girard, F. Lelarge, J. M. Fedeli, A. Descos, B. Ben Bakir, S. Messaoudene, D. Bordel, S. Menezo, G. de Valicourt, S. Keyvaninia,

G. Roelkens, D. Van Thourhout, D. J. Thomson, F. Y. Gardes, and G. T. Reed, "Hybrid III–V on silicon lasers for photonic integrated circuits on silicon," *IEEE Journal of Selected Topics in Quantum Electronics*, vol. 20, no. 4, p. 6100213, 2014.

[9] Q. Xu, B. Schmidt, S. Pradhan, and M. Lipson, "Micrometre-scale silicon electro-optic modulator," *Nature*, vol. 435, pp. 325–327, May 2005.

[10] G. Li, A. Krishnamoorthy, I. Shubin, J. Yao, Y. Luo, H. Thacker, X. Zheng, K. Raj, and J. Cunningham, "Ring resonator modulators in silicon for interchip photonic links," *IEEE Journal of Selected Topics in Quantum Electronics*, vol. 19, no. 6, p. 3401819, 2013.

[11] F. Gan, T. Barwicz, M. A. Popovic, M. S. Dahlem, C. W. Holzwarth, P. T. Rakich, H. I. Smith, E. P. Ippen, and F. X. Kartner, "Maximizing the thermo-optic tuning range of silicon photonic structures," *Photonics in Switching*, pp. 67–68, 2007.

[12] V. Van, T. Ibrahim, K. Ritter, P. Absil, F. Johnson, R. Grover, J. Goldhar, and P. T. Ho, "All-optical nonlinear switching in GaAs-AlGaAs microring resonators," *IEEE Photonics Technology Letters*, vol. 14, no. 1, pp. 74–76, Jan. 2002.

[13] A. Biberman, H. Lira, K. Padmaraju, N. Ophir, J. Chan, M. Lipson, and K. Bergman, "Broadband silicon photonic electrooptic switch for photonic interconnection networks," *IEEE Photonics Technology Letters*, vol. 23, no. 8, pp. 504–506, 2011.

[14] J. Yang, N. K. Fontaine, Z. Pan, A. O. Karalar, S. S. Djordjevic, C. Yang, W. Chen, S. Chu, B. E. Little, and S. J. B. Yoo, "Continuously tunable, wavelength-selective buffering in optical packet switching networks," *IEEE Photonics Technology Letters*, vol. 20, no. 12, pp. 1030–1032, Jun. 2008.

[15] C. Stamatiadis, K. Vyrsokinos, L. Stampoulidis, I. Lazarou, A. Maziotis, J. Bolten, M. Karl, T. Wahlbrink, P. D. Heyn, Z. Sheng, D. V. Thourhout, and H. Avramopoulos, "Silicon-on-insulator nanowire resonators for compact and ultra-high speed all-optical wavelength converters," *Journal of Lightwave and Technology*, vol. 29, no. 20, pp. 3054–3060, 2011.

[16] M. Petracca, B. Lee, K. Bergman, and L. Carloni, "Photonic NoCs: System-level design exploration," *IEEE Micro*, vol. 29, no. 4, pp. 74–85, Jul. 2009.

[17] A. Bianco, D. Cuda, M. Garrich, R. Gaudino, G. Gavilanes, and P. Giaccone, "Optical interconnection networks based on microring resonators," *IEEE Micro*, vol. 4, no. 7, pp. 546–556, 2012.

[18] P. Dong, S. Preble, and M. Lipson, "All-optical compact silicon comb switch," *Optics Express*, vol. 15, pp. 9600–9605, 2007.

[19] C. Stamatiadis, F. Gomez-Agis, L. Stampoulidis, K. Vyrsokinos, I. Lazarou, H. Dorren, L. Zimmermann, K. Voigt, D. Thourhout, P. Heyn, and H. Avramopoulos, "The BOOM project: towards 160 Gb/s packet switching

using SOI photonic integrated circuits and hybrid integrated optical flip-flops," *Journal of Lightwave and Technology*, vol. 30, no. 1, pp. 22–30, Jan. 2012.

[20] A. Bianco, D. Cuda, M. Garrich, G. Gavilanes, V. Martina, and F. Neri, "Crosstalk minimization in microring-based wavelength routing matrices," *Proceedings of IEEE Global Telecommunications Conference*, pp. 1–5, Dec. 2011.

[21] D. Siracusa, V. Linzalata, G. Maier, A. Pattavina, Y. Yabin, and C. Ming, "Hybrid architecture for optical interconnection based on micro ring resonators," *Proceedings of IEEE Global Telecommunications Conference*, pp. 1–5, Dec. 2011.

[22] M. H. Xiao, Shijun; Khan, H. Shen, and M. Qi, "Multiple-channel silicon micro-resonator based filters for WDM applications," *Optics Express*, vol. 15, no. 12, pp. 7489–7498, Jun. 2007.

[23] P. Dong, W. Qian, H. Liang, R. Shafiiha, X. Wang, D. Feng, G. Li, J. E. Cunningham, A. V. Krishnamoorthy, and M. Asghari, "1 × 4 reconfigurable demultiplexing filter based on free-standing silicon racetrack resonators," *Optics Express*, vol. 18, no. 24, pp. 24 504–24 509, Nov. 2010.

[24] M. Tlidi and L. Gelens, "High-order dispersion stabilizes dark dissipative solitons in all-fiber cavities," *Optics Letters*, vol. 35, no. 3, pp. 306–308, 2010.

[25] S. Park, K.-J. Kim, I.-G. Kim, and G. Kim, "Si micro-ring MUX/DeMUX WDM filters," *Optics Express*, vol. 19, no. 14, pp. 13 531–13 539, Jul. 2011.

[26] M. Al-Fares, A. Loukissas, and A. Vahdat, "A scalable, commodity data center network architecture," in *Proceedings of the ACM SIGCOMM conference on Data communication*, Seattle, Washington, USA, 2008, pp. 63–74.

[27] A. Greenberg, J. R. Hamilton, N. Jain, S. Kandula, C. Kim, P. Lahiri, D. A. Maltz, P. Patel, and S. Sengupta, "VL2: a scalable and flexible data center network," *Communications of the ACM*, vol. 54, no. 3, pp. 95–104, Mar. 2011.

[28] N. Sherwood-Droz, H. Wang, L. Chen, B. G. Lee, A. Biberman, K. Bergman, and M. Lipson, "Optical 4 × 4 hitless silicon router for optical networks-on-chip (NoC)," *Optics Express*, vol. 16, no. 20, pp. 15 915–15 922, 2008.

[29] R. Ji, L. Yang, L. Zhang, Y. Tian, J. Ding, H. Chen, Y. Lu, P. Zhou, and W. Zhu, "Five-port optical router for photonic networks-on-chip," *Optics Express*, vol. 19, no. 21, pp. 20 258–20 268, Oct. 2011.

[30] S. Papaioannou, K. Vyrsokinos, O. Tsilipakos, A. Pitilakis, K. Hassan, J. C. Weeber, L. Markey, A. Dereux, S. I. Bozhevolnyi, A. Miliou, E. Kriezis, and N. Pleros, "A 320 Gb/s-throughput capable 2 x 2 silicon-plasmonic router architecture for optical interconnects," *Journal of Lightwave Technology*, vol. 29, no. 21, pp. 3185–3195, Nov. 2011.

[31] Y. Goebuchi, M. Hisada, T. Kato, and Y. Kokubun, "Optical cross-connect circuit using hitless wavelength selective switch," *Optics Express*, vol. 16, no. 2, pp. 535–548, 2008.

[32] R. Soref and B. Bennett, "Electrooptical effects in silicon," *IEEE Journal of Quantum Electronics*, vol. 23, no. 1, pp. 123–129, Jan. 1987.

[33] M. W. Geis, S. J. Spector, R. C. Williamson, and T. M. Lyszczarz, "Submicrosecond submilliwatt silicon-on-insulator thermooptic switch," *IEEE Photonics Technology Letters*, vol. 16, no. 11, pp. 2514–2516, Nov. 2004.

[34] V. R. Almeida, C. A. Barrios, R. R. Panepucci, and M. Lipson, "All-optical control of light on a silicon chip," *Nature*, vol. 431, pp. 1081–1084, Oct. 2004.

[35] B. G. Lee, A. Biberman, P. Dong, M. Lipson, and K. Bergman, "All-optical comb switch for multiwavelength message routing in silicon photonic networks," *Photonics Technology Letters*, vol. 20, no. 10, pp. 767–769, May 2008.

[36] A.Yalcin, K. Popat, J. C. Aldridge, T. A. Desai, J. Hryniewicz, N. Chbouki, B. E. Little, O. King, V. Van, S. Chu, D. Gill, M. Anthes-Washburn, M. S. Unlu, and B. B. Goldberg, "Optical sensing of biomolecules using microring resonators," *IEEE Journal of Selected Topics in Quantum Electronics*, vol. 12, no. 1, pp. 148–155, Jan./Feb. 2006.

[37] C. A. Barrios, V. R. de Almeida, and M. Lipson, "Low-power-consumption short-length and high-modulation-depth silicon electrooptic modulator," *Journal of Lightwave Technology, vol.21, no.4,* pp. 1089–1098, Apr. 2003.

[38] A. Biberman, H. L. R. Lira, K. Padmaraju, N. Ophir, J. Chan, M. Lipson, and K. Bergman, "Broadband silicon photonic electrooptic switch for photonic interconnection networks," *IEEE Photonics Technology Letters*, vol. 23, no. 8, pp. 504–506, Apr. 2011.

[39] L. Xu, W. Zhang, Q. Li, J. Chan, H. Lira, M. Lipson, and K. Bergman, "40-Gb/s DPSK data transmission through a silicon microring switch," *IEEE Photonics Technology Letters*, vol. 24, no. 6, pp. 473–475, Mar. 2012.

[40] X. Luo, J. Song, S. Feng, A. W. Poon, T. Y. Liow, M. Yu, G. Q. Lo, and D. L. Kwong, "Silicon high-order coupled-microring-based electro-optical switches for on-chip optical interconnects," *IEEE Photonics Technology Letters*, vol. 24, no. 10, pp. 821–823, May 2012.

[41] M. Tinker and J. Lee, "Thermo-optic photonic crystal light modulator," *Applied physics letters*, vol. 28, no. 221111, pp. 1–3, 2005.

[42] F. Gan, T. Barwicz, M. A. Popovic, M. S. Dahlem, C. W. Holzwarth, P. T. Rakich, H. I. Smith, E. P. Ippen, and F. X. Kartner, "Maximizing the thermo-optic tuning range of silicon photonic structures," *Photonics in Switching*, pp. 67–68, 2007.

[43] P. Dong, W. Qian, H. Liang1, R. Shafiiha1, N. Feng, D. Feng, X. Zheng, A. V. Krishnamoorthy, and M. Asghar, "Low power and compact reconfigurable multiplexing devices based on silicon microring resonators," *Optics Express*, vol. 18, no. 10, pp. 9852–9858, May 2010.

[44] C. Stamatiadis, F. Gomez-Agis, L. Stampoulidis, K. Vyrsokinos, I. Lazarou, H. J. S. Dorren, L. Zimmermann, K. Voigt, D. V. Thourhout, P. D. Heyn, and

H. Avramopoulos, "The BOOM project: towards 160 Gb/s packet switching using SOI photonic integrated circuits and hybrid integrated optical flip-flops," *Journal of Lightwave Technology*, vol. 30, no. 1, pp. 22–30, Jan. 2012.

[45] M. S. Dahlem, C. W. Holzwarth, A. Khilo, F. X. Kartner, H. I. Smith, and E. P. Ippen, "Reconfigurable multi-channel second-order silicon microring-resonator filterbanks for on-chip wdm systems," *Optics Express*, vol. 19, no. 1, pp. 306–316, 2011.

[46] T. Hu, W. Wang, C. Qiu, P. Yu, H. Qiu, Y. Zhao, X. Jiang, and J. Yang, "Thermally tunable filters based on third-order microring resonators for WDM applications," *IEEE Photonics Technology Letters*, vol. 24, no. 6, pp. 524–526, Mar. 2012.

[47] C. Stamatiadis, K. Vyrsokinos, L. Stampoulidis, I. Lazarou, A. Maziotis, J. Bolten, M. Karl, T. Wahlbrink, P. D. Heyn, Z. Sheng, D. V. Thourhout, and H. Avramopoulos, "Silicon-on-insulator nanowire resonators for compact and ultra-high speed all-optical wavelength converters," *Journal of Lightwave Technology*, vol. 29, no. 20, pp. 3054–3060, Oct. 2011.

[48] K. Tanaka and Y. Kokubun, "Demonstration of OCDM coder and variable bandwidth filter using parallel topology of quadruple series coupled microring resonators," *IEEE Photonics Journal*, vol. 3, no. 1, pp. 20–25, Feb. 2011.

[49] V. R. Almeida, C. A. Barrios, R. R. Panepucci, M. Lipson, M. A. Foster, D. G. Ouzounov, and A. L. Gaeta, "All-optical switching on a silicon chip," *Optics Letters*, vol. 29, no. 24, pp. 2867–2869, Dec. 2004.

[50] B. G. Lee, A. Biberman, N. Sherwood-Droz, C. B. Poitras, M. Lipson, and K. Bergman, "High-speed 2×2 switch for multiwavelength silicon-photonic networks-on-chip," *Journal of Lightwave Technology*, vol. 27, no. 14, pp. 2900–2907, Jul. 2009.

[51] P. Dong, S. F. Preble, , and M. Lipson, "All-optical compact silicon comb switch," *Optics Express*, vol. 15, no. 15, pp. 9600–9605, 2007.

[52] Y. H. Wen, O. Kuzucu, M. Fridman, A. L. Gaeta, L. W. Luo, and M. Lipson, "All-optical control of an individual resonance in a silicon microresonator," *Physical Review Letters*, vol. 108, p. 223907, Jun. 2012.

[53] A. M. Prabhu, A. Tsay, Z. Han, and V. Van, "Extreme miniaturization of silicon add-drop microring filters for VLSI photonics applications," *IEEE Photonics Journal*, vol. 2, no. 3, pp. 436–444, Jun. 2010.

[54] ——, "Ultracompact soi microring Add/Drop filter with wide bandwidth and wide FSR," *IEEE Photonics Technology Letters*, vol. 21, no. 10, pp. 651–653, May 2009.

[55] F. Xia, M. Rooks, L. Sekaric, and Y. Vlasov, "Ultra-compact high order ring resonator filters using submicron silicon photonic wires for on-chip optical interconnects," *Optics Express*, vol. 15, no 19, pp. 11 934–11 941, 2007.

[56] S. Xiao, M. H. Khan, H. Shen, and M. Qi, "A highly compact third-order

silicon microring add-drop filter with a very large free spectral range, a flat passband and a low delay dispersion," *Optics Express*, vol. 15, no. 22, pp. 14 765–14 771, Oct. 2007.

[57] http://www.itu.int/rec/T-REC-G.694.1-201202-I/en.

[58] P. Dong, R. Shafiiha, S. Liao, H. Liang, N. N. Feng, D. Feng, G. Li, X. Zheng, A. V. Krishnamoorthy, and M. Asghari, "Wavelength-tunable silicon microring modulator," *Optics Express*, vol. 18, no. 11, pp. 10 941–10 946, May 2010.

[59] S. Manipatruni, R. K. Dokania, B. Schmidt, N. Sherwood-Droz, C. B. Poitras, and A. B. A. M. Lipson, "Wavelength-tunable silicon microring modulator," *Optics Letters*, vol. 33, no. 19, pp. 2185–2187, Oct. 2008.

[60] C. Qiu, J. Shu, Z. Li, X. Zhang, and Q. Xu, "Wavelength tracking with thermally controlled silicon resonators," *Optics Express*, vol. 19, no. 6, pp. 5143–5148, Mar. 2011.

[61] P. Alipour, E. S. Hosseini, A. A. Eftekhar, B. Momeni, and A. Adibi, "Athermal performance in high-Q polymer-clad silicon microdisk resonators," *Optics Letters*, vol. 35, no. 20, pp. 3462–3464, 2010.

[62] M. Han and A. Wang, "Temperature compensation of optical microresonators using a surface layer with negative thermo-optic coefficient," *Optics Letters*, vol. 32, no. 13, pp. 1800–1802, 2007.

[63] J. Teng, P. Dumon, W. Bogaerts, H. Zhang, X. Jian, X. Han, M. Zhao, G. Morthier, and R. Baets, "Athermal silicon-on-insulator ring resonators by overlaying a polymer cladding on narrowed waveguides," *Optics Express*, vol. 17, no. 17, pp. 14 627–14 633, Aug. 2009.

[64] V. Raghunathan, W. N. Ye, J. Hu, T. Izuhara, J. Michel, and L. Kimerling, "Athermal operation of silicon waveguides: spectral, second order and footprint dependencies," *Optics Express*, vol. 18, no. 17, pp. 17 631–17 639, Aug. 2010.

[65] B. Guha, A. Gondarenko, and M. Lipson, "Minimizing temperature sensitivity of silicon mach-zehnder interferometers," *Optics Express*, vol. 18, no. 3, pp. 1879–1887, Feb. 2010.

[66] B. Guha, K. Preston, and M. Lipson, "Athermal silicon microring electro-optic modulator," *Optics Letters*, vol. 37, no. 12, pp. 2253–2255, Jun. 2012.

[67] W. Zhang, L. Xu, Q. Li, H. L. R. Lira, M. Lipson, and K. Bergman, "Broadband silicon photonic packet-switching node for large-scale computing systems," *IEEE Photonics Technology Letters*, vol. 24, no. 8, pp. 688–690, Apr. 2012.

[68] K. Okamoto, M. Okuno, A. Himeno, and Y. Ohmori, "16-channel optical add/drop multiplexer consisting of arrayed-waveguide gratings and double-gate switches," *Electronics Letters*, vol. 32, no. 16, pp. 1471–1472, 1996.

[69] C. G. P. Herben, D. H. P. Maat, X. J. M. Leijtens, M. R. Leys, Y. S. Oei, and M. Smit, "Polarization independent dilated WDM cross-connect on InP,"

IEEE Photonics Technology Letters, vol. 11, no. 12, pp. 1599–1601, 1999.

[70] G. Baxter, S. Frisken, D. Abakoumov, H. Zhou, I. Clarke, A. Bartos, and S. Poole, "Highly programmable wavelength selective switch based on liquid crystal on silicon switching elements," in *Optical Fiber Communication Conference and Exposition and The National Fiber Optic Engineers Conference*, 2006, oTuF2.

[71] Y. Ishii, K. Hadama, J. Yamaguchi, Y. Kawajiri, E. Hashimoto, T. Matsuura, and F. Shimokawa, "MEMS-based 1×43 wavelength-selective switch with flat passband," in *35th European Conference on Optical Communication (ECOC)*, 2009.

[72] C. R. Doerr, L. L. Buhl, L. Chen, and N. Dupuis, "Monolithic flexible-grid 1×2 wavelength-selective switch in silicon photonics," *Journal of Lightwave Technology*, vol. 30, no. 4, pp. 473–478, Feb. 2012.

[73] W. Bogaerts, P. D. Heyn, T. V. Vaerenbergh, K. D. Vos, S. K. Selvaraja, T. Claes, P. Dumon, P. Bienstman, D. V. Thourhout, and R. Baets, "Silicon microring resonators," *Laser & Photonics Reviews*, vol. 6, no. 1, pp. 47–73, 2012.

[74] B. G. Lee, A. Biberman, J. Chan, and K. Bergman, "High-performance modulators and switches for silicon photonic networks-on-chip," *IEEE Journal of Selected Topics in Quantum Electronics*, vol. 16, no. 1, pp. 6–22, Jan./Feb. 2010.

[75] H. Yan, X. Feng, D. Zhang, K. Cui, F. Liu, and Y. Huang, "Compact optical add-drop multiplexers with parent-sub ring resonators on soi substrates," *IEEE Photonics Technology Letters*, vol. 25, no. 15, pp. 1462–1465, Aug. 2013.

[76] B. E. Little, S. T. Chu, H. A. Haus, J. Foresi, and J. P. Laine, "Microring resonator channel dropping filters," *Journal of Lightwave Technology*, vol. 15, no. 6, pp. 998–1005, Jun. 1997.

[77] S. Xiao, M. H. Khan, H. Shen, and M. Qi, "Silicon-on-Insulator microring Add-Drop filters with free spectral ranges over 30 nm," *Journal of Lightwave Technology*, vol. 26, no. 2, pp. 228–236, Jan. 2008.

[78] F. Xia, M. Rooks, L. Sekaric, and Y. Vlasov, "Ultra-compact high order ring resonator filters using submicron silicon photonic wires for onchip optical interconnects," *Optics Express*, vol. 15, no. 19, pp. 11 934–11 941, Sep. 2007.

[79] L. Y. Tobing, P. Dumon, R. Baets, and M.-K. Chin, "Box-like filter response of two-dimensional array of microring resonator fabricated in silicon-on-insulator technology," in *Proceedins of 5th IEEE International Conference on Group IV Photonics*, Sorrento, Italy, Sep. 2008, pp. 237–239.

[80] Y. Goebuchi, M. Hisada, T. Kato, and Y. Kokubun, "Optical cross-connect circuit using hitless wavelength selective switch," *Optics Express*, vol. 16, no. 2, pp. 535–548, Jan. 2008.

[81] J. R. Ong, R. Kumar, and S. Mookherjea, "Ultra-high-contrast and tunable-bandwidth filter using cascaded high-order silicon microring filters," *IEEE Photonics Technology Letters*, vol. 25, no. 16, pp. 1543–1546, Aug. 2013.

[82] J. K. S. Poon, J. Scheuer, S. Mookherjea, G. T. Paloczi, Y. Huang, and A. Yariv, "Matrix analysis of microring coupled-resonator optical waveguides," *Optics Express*, vol. 12, no. 1, pp. 90–103, Jan. 2004.

[83] S. Xiao, M. H. Khan, H. Shen, and M. Qi, "Compact silicon microring resonators with ultra-low propagation loss in the C band," *Optics Express*, vol. 15, no. 22, pp. 14 467–14 475, Oct. 2007.

[84] Y. Vlasov and S. McNab, "Losses in single-mode silicon-on-insulator strip waveguides and bends," *Optics Express*, vol. 12, no. 8, pp. 1622–1631, Apr. 2004.

[85] D. Marcuse, "Bend loss of slab and fiber modes computed with diffraction theory," *IEEE Journal of Quantum Electronics*, vol. 29, no. 12, pp. 2957–2961, 1993.

[86] S. H. Tao, S. C. Mao, J. F. Song, Q. Fang, M. B. Yu, G. Q. Lo, and D. L. Kwong, "Ultra-high order ring resonator system with sharp transmission peaks," *Optics Express*, vol. 18, no. 2, pp. 393–400, Jan. 2010.

[87] M. L. Cooper and S. Mookherjea, "Modeling of multiband transmission in long silicon coupled-resonator optical waveguides," *IEEE Photonics Technology Letters*, vol. 23, no. 13, pp. 872–874, Jul. 2011.

[88] X. Zhu, Q. Li, J. Chan, A. Ahsan, H. L. R. Lira, M. Lipson, and K. Bergman, "4×44 Gb/s packet-level switching in a second-order microring switch," *IEEE Photonics Technology Letters*, vol. 24, no. 17, pp. 1555–1557, Sep. 2012.

[89] S. M. H. L. R. Lira and M. Lipson, "Broadband hitless silicon electro-optic switch for on-chip optical networks," *Optics Express*, vol. 17, no. 25, pp. 22 271–22 280, Dec. 2009.

[90] S. Kamei, M. Ishii, A. Kaneko, T. Shibata, and M. Itoh, "$N \times N$ cyclic-frequency router with improved performance based on arrayed-waveguidge grating," *Journal of Lightwave and Technology*, vol. 27, no. 18, pp. 4097–4104, 2009.

[91] T. A. Strasser and J. Taylor, "ROADMS unlock the edge of the network," *IEEE Communications Magazine.*, vol. 46, no. 7, pp. 146–149, 2008.

[92] K. Christodoulopoulos, I. Tomkos, and E. A. Varvarigos, "Elastic bandwidth allocation in flexible ofdm-based optical networks," *Journal of Lightwave and Technology*, vol. 29, no. 9, pp. 1354–1366, 2011.

[93] M. Jinno, H. Takara, B. Kozicki, Y. Tsukishima, Y. Sone, and S. Matsuoka, "Spectrum-efficient and scalable elastic optical path network: architecture, benefits, and enabling technologies," *IEEE Communications Magazine.*, vol. 47, no. 11, pp. 66–73, 2009.

[94] M. Jinno, B. Kozicki, H. Takara, A. Watanabe, Y. Sone, T. Tanaka, and A. Hirano, "Distance-adaptive spectrum resource allocation in spectrum-sliced elastic optical path network," *IEEE Communications Magazine*, vol. 48, no. 8, pp. 138–145, 2010.

[95] J. Xia, A. Bianco, E. Bonetto, and R. Gaudino, "On the design of microring resonator devices for switching applications in flexible-grid networks," in *IEEE International Conference on Communications (ICC)*, Sydney, Australia, 2014, pp. 3371–3376.

[96] R. Aguinaldo, Y. Shen, and S. Mookherjea, "Large dispersion of silicon directional couplers obtained via wideband microring parametric characterization," *IEEE Photonics Technology Letters*, vol. 24, no. 10, pp. 1242–1244, Jul. 2012.

[97] http://www.optiwave.com.

[98] J. Cardenas, C. B. Poitras, J. T. Robinson, K. Preston, L. Chen, and M. Lipson, "Low loss etchless silicon photonic waveguides," *Optics Express*, vol. 17, no. 6, pp. 4752–4757, Mar. 2009.

[99] G. Cocorullo and I. Rendina, "Thermo-optical modulation at 1.5 μm in silicon etalon," *Electronics Letters*, vol. 28, no. 1, pp. 83–85, 1992.

[100] P. Salihundam, S. Jain, T. Jacob, S. Kumar, V. Erraguntla, Y. Hoskote, S. Vangal, G. Ruhl, and N. Borkar, "A 2 Tb/s 6 $\times$ 4 mesh network for a single-chip cloud computer with DVFS in 45 nm CMOS," *IEEE Journal of Solid-State Circuits*, vol. 46, no. 4, pp. 757–766, 2011.

[101] S. Cheung, T. Su, K. Okamoto, and S. J. B. Yoo, "Ultra-compact silicon photonic 512×512 25 GHz arrayed waveguide grating router," *IEEE Journal of Selected Topics in Quantum Electronics*, vol. 20, no. 4, p. 8202207, 2014.

[102] P. Dong, S. Liao, D. Feng, H. Liang, D. Zheng, R. Shafiiha, C. C. Kung, W. Qian, G. Li, X. Zheng, A. V. Krishnamoorthy, and M. Asghari, "Low Vpp, ultralow-energy, compact, high-speed silicon electro-optic modulator," *Optics Express*, vol. 17, no. 25, pp. 22 484–22 490, Dec. 2009.

[103] D. Ahn, C. yin Hong, J. Liu, W. Giziewicz, M. Beals, L. C. Kimerling, J. Michel, J. Chen, and F. X. Kartner, "High performance, waveguide integrated Ge photodetectors," *Optics Express*, vol. 15, no. 7, pp. 3916–3921, Apr. 2007.

[104] H. Park, A. W. Fang, O. Cohen, R. Jones, M. J. Paniccia, , and J. E. Bowers, "A hybrid AlGaInAs-silicon evanescent amplifier," *IEEE Photonics Technology Letters*, vol. 19, no. 4, pp. 230–232, Feb. 2007.

[105] A. W. Fang, H. Park, O. Cohen, R. Jones, M. J. Paniccia, and J. E. Bowers, "Electrically pumped hybrid AlGaInAs-silicon evanescent laser," *Optics Express*, vol. 14, no. 20, pp. 9203–9210, Oct. 2006.

[106] R. Yu, S. C. and1 Yuliang Li, K. Okamoto, R. Proietti, Y. Yin, and S. J. B. Yoo, "A scalable silicon photonic chip-scale optical switch for high performance computing systems," *Optics Express*, vol. 21, no. 23, pp. 32 655–32 667, Nov.

2013.

[107] A. Bennecer, K. Williams, R. Penty, I. White, M. Hamacher, and H. Heidrich, "Directly modulated wavelength-multiplexed integrated microring laser array," *IEEE Photonics Technology Letters*, vol. 20, no. 16, pp. 1411–1413, Aug. 2008.

[108] A. Bianco, D. Cuda, R. Gaudino, G. Gavilanes, F. Neri, and M. Petracca, "Scalability of optical interconnects based on microring resonators," *IEEE Photonics Technology Letters*, vol. 22, no. 15, pp. 1081–1083, Aug. 2010.